



BRNO UNIVERSITY OF TECHNOLOGY

VYSOKÉ UČENÍ TECHNICKÉ V BRNĚ

CENTRAL EUROPEAN INSTITUTE OF TECHNOLOGY BUT

STŘEDOEVROPSKÝ TECHNOLOGICKÝ INSTITUT VUT

EXTENDED DEFECTS IN GA AND AL NITRIDES

ROZSÁHLÉ DEFEKTY V NITRIDECH GA A AL

DOCTORAL THESIS

DIZERTAČNÍ PRÁCE

AUTHOR

AUTOR PRÁCE

Ing. Petr Vacek

SUPERVISOR

ŠKOLITEL

doc. Ing. Roman Gröger, Ph.D. et Ph.D.

BRNO 2021

Abstract

III-nitrides crystallize in the hexagonal (wurtzite) structure, whereas the cubic (zincblende, sphalerite) structure is metastable with only slightly higher energy. Their physical properties are strongly affected by the presence of extended defects that are of different kinds in the two structures. In wurtzite III-nitrides, these are primarily threading dislocations, some of which are known to generate deep defect states in the bandgap, through which they affect the electrical and optoelectronic properties of devices. On the other hand, zincblende III-nitrides contain a large density of stacking faults that facilitate local transformations into the more stable wurtzite structure. The aim of this work is to characterize the extended defects in both crystal structures using a combination of electron microscopy, atomic force microscopy, and X-ray diffraction.

We demonstrate that (0001)-oriented samples of GaN/AlN and AlN grown on Si (111) substrate by metal-organic chemical vapor deposition contain a large density of threading dislocations. Their Burgers vectors are mostly parallel to the a -direction of the wurtzite lattice, followed by the Burgers vectors parallel to the $a+c$ -direction, whereas the dislocations with Burgers vectors parallel to the c -direction are relatively rare. The probable origin of threading dislocations is discussed according to the type of the film growth. Prismatic stacking faults were found in thin AlN nucleation layers but were not present in the thicker layers. Amorphous layer composed of SiN_x and partially of AlN was found at the AlN/Si interface. We propose that this amorphous layer could have a major role in the relief of misfit strain. Analysis of electrical activity of extended defects in AlN was done using electron beam induced current technique. We have found that threading dislocations cause a weak drop of induced current. However, due to their high density and uniform distribution, they have larger impact on electrical properties than V-defects and their clusters.

The topographical and crystallographic defects were studied in as-grown and annealed nucleation layers of zincblende GaN grown on 3C-SiC (001) / Si (001) substrate. The sizes of surface features on as-grown samples increase with the thickness of the nucleation layer and are enhanced by annealing. The surface coverage of GaN with the thinnest nucleation layers is reduced after annealing due to diffusion and desorption (or etching by reactor atmosphere). The stacking faults found in GaN near its interface with SiC were mostly of the intrinsic type bounded by Shockley partial dislocations. The origin of these stacking faults was discussed as well as the impact of partial dislocations on the strain relief. Due to the abundance of stacking faults, their interactions were studied in detail. Based on our findings, we have developed a theoretical model of stacking fault annihilation in zincblende GaN films. This model is shown to be able to predict the decrease of the stacking fault density with increasing film thickness.

Keywords

III-nitrides, gallium nitride, aluminum nitride, TEM, AFM, threading dislocations, stacking faults

Abstrakt

III-nitridy běžně krystalizují v hexagonální (wurtzitové) struktuře, zatímco kubická (sfaleritová) struktura je metastabilní a má pouze mírně vyšší energii. Jejich fyzikální vlastnosti jsou silně ovlivněny přítomností rozsáhlých defektů, které jsou v těchto dvou strukturách od sebe odlišné. U wurtzitových nitridů se jedná primárně o vláknové dislokace. Některé vláknové dislokace tvoří hluboké energetické stavy v zakázaném pásu, kterými ovlivňují elektrické a optoelektronické vlastnosti těchto materiálů. Oproti tomu, kubické nitridy obsahují množství vrstevných chyb, které představují lokální transformace do stabilnější wurtzitové struktury. Cílem této práce je charakterizovat rozsáhlé defekty v obou krystalových strukturách pomocí elektronové mikroskopie, mikroskopie atomárních sil a rentgenové difrakce.

Prokázali jsme, že vzorky GaN/AlN a AlN s orientací (0001) rostlé na substrátu Si (111) pomocí epitaxe z organokovových sloučenin obsahují velkou hustotu vláknových dislokací. Nejčastější jsou dislokace s Burgersovým vektorem s komponentou ve směru a wurtzitové struktury, následované dislokacemi s Burgersovým vektorem s komponentou ve směru $a+c$, zatímco dislokace s Burgersovým vektorem s c komponentou jsou relativně vzácné. Pravděpodobný původ vláknových dislokací je diskutován v souvislosti s různými mechanismy růstu těchto vrstev. Prizmatické vrstevné chyby byly nalezeny v tenkých nukleačních vrstvách AlN, ale v tlustších vrstvách již nebyly přítomny. Na rozhraní AlN / Si byla nalezena amorfnní vrstva složená ze SiN_x a částečně taky z AlN. Navrhujeme, že by tato amorfnní vrstva mohla hrát významnou roli při relaxaci misfitového napětí. Analýza elektrické aktivity rozsáhlých defektů v AlN byla provedena pomocí měření proudu indukovaného elektronovým svazkem. Zjistili jsme, že vláknové dislokace způsobují slabý pokles indukovaného proudu. Díky jejich vysoké hustotě a rovnoměrnému rozložení však mají větší vliv na elektrické vlastnosti, než mají V-defekty a jejich shluky.

Topografické a krystalografické defekty byly studovány na nežíhaných a žíhaných nukleačních vrstvách kubického GaN deponovaných na 3C-SiC (001) / Si (001) substrátu. Velikost ostrůvků na nežíhaných vzorcích se zvyšuje s tloušťkou nukleační vrstvy a po žíhání se dále zvětšuje. Po žíhání se snižuje pokrytí substrátu u nejtenčích nukleačních vrstev v důsledku difúze a desorpce (nebo leptání atmosférou reaktoru). Vrstevné chyby nalezené ve vrstvách GaN, poblíž rozhraní se SiC, byly většinou identifikovány jako intrinsické a byly ohraničené Shockleyho parciálními dislokacemi. Jejich původ byl diskutován, jako i vliv parciálních dislokací na relaxaci misfitového napětí. Díky velkému množství vrstevných chyb byly podrobněji studovány jejich interakce. Na základě našich zjištění jsme vyvinuli teoretický model popisující anihilaci vrstevných chyb v kubických vrstvách GaN. Tento model dokáže předpovědět pokles hustoty vrstevných chyb se zvyšující se tloušťkou vrstvy.

Klíčová slova

Nitridy III-A skupiny, nitrid gallia, nitrid hliníku, TEM, AFM, vláknové dislokace, vrstevné chyby

VACEK, Petr. *Rozsáhlé defekty v nitridech Ga a Al*. Brno, 2021. Dostupné také z: <https://www.vutbr.cz/studenti/zav-prace/detail/135175>. Dizertační práce. Vysoké učení technické v Brně, Středoevropský technologický institut VUT, Středoevropský technologický institut VUT. Vedoucí práce Roman Gröger.

Prohlašuji, že jsem dizertační práci Rozsáhlé defekty v nitridech Ga a Al vypracoval samostatně pod odborným vedením doc. Ing. Romana Grögera, Ph.D. s použitím materiálů uvedených v seznamu literatury.

V Brně dne: 13. 4. 2021

.....

Ing. Petr Vacek

Acknowledgement

I would like to thank my supervisor Roman Gröger for his support, scientific discussions and all the time and effort he put into supervising my PhD studies. I would also like to thank my co-supervisor Tomáš Kruml for useful scientific discussions. I would like to thank Rachel Oliver and Martin Frentrup for supervision during my research stay at the University of Cambridge. I would also like to thank all my wonderful colleagues both from the Institute of Physics of Materials, CAS and the University of Cambridge whom I had the pleasure to work with.

A part of this project was made in collaboration with Tescan (Jiří Dluhoš) and NenoVision (Zdeněk Nováček).

I would like to thank ON Semiconductor (Petr Kostelník) for the growth of wurtzite III-nitride samples and for discussing the results.

I would like to thank the Ministry of Education, Youth and Sports of the Czech Republic (MEYS CR) for supporting my 6-month research stay at the Cambridge Centre for Gallium Nitride through the project no. CZ.02.2.69/0.0/0.0/16_027/0008056.

A part of this research was financially supported by CEITEC BUT, Brno University of Technology, under the grant STI-J-17-4388. The CzechNanoLab project LM2018110 funded by the MEYS CR is gratefully acknowledged for the financial support of the measurements at CEITEC Nano Research Infrastructure. This research has been carried out under the project CEITEC 2020 (LQ1601) with financial support from the Ministry of Education, Youth and Sports of the Czech Republic under the National Sustainability Programme II.

Table of contents

1 Introduction	13
2 Fundamental physics of III-nitrides	15
2.1 Bandgap, emission spectrum and bonding	15
2.2 Crystal structures	16
2.3 Defects and their physical properties	18
2.3.1 Point defects	19
2.3.2 Dislocations	20
2.3.3 Stacking faults	23
2.4 Substrates	24
2.5 Electron beam induced current	25
3 Aims of thesis	28
4 Materials and methods	29
4.1 Atomic force microscopy	29
4.2 Scanning electron microscopy	29
4.3 Transmission electron microscopy	29
4.4 X-ray diffraction	30
4.5 Correlative probe and electron microscopy	30
5 Results and discussion	31
5.1 Defects in wurtzite AlN and GaN	31
5.1.1 Topography of AlN nucleation layers	31
5.1.2 Defects in wurtzite GaN and AlN	32
5.1.3 Electrical activity of extended defects in AlN layers	46
5.1.4 Correlative probe and electron microscopy	52
5.2 Defects in zincblende GaN	56
5.2.1 Defects in zincblende GaN nucleation layers	56
5.2.2 Stacking faults and dislocations in zincblende GaN	65
5.2.3 Interaction of stacking faults in zincblende GaN	72
6 Conclusions	79
7 References	81

1 Introduction

The group III-nitrides (AlN, GaN, InN) are direct wide-bandgap semiconductors that have a wide range of applications in optoelectronics and microelectronics [1]. Combining these materials and utilizing substitutional doping allows to tune their emission spectra from near infrared (pure InN), via the visible part of the spectrum, to deep ultraviolet (pure AlN). The green and red light-emitting diodes (LEDs) have been known for a long time, but the lack of blue/violet source of light has been an obstacle to the making white LEDs. The invention of blue LEDs based on doped GaN, and thus the possibility of making white LEDs, was so significant that their inventors, Isamu Akasaki, Hiroshi Amano and Shuji Nakamura, received the 2014 Nobel prize for physics.

The III-nitrides crystallize in the polar wurtzite (hexagonal) structure, but non-polar zincblende (cubic) structure can be stabilized using epitaxial growth on cubic substrates such as Si {001} or {00 $\bar{1}$ } planes of the 3C polytype of SiC. The III-nitrides are frequently grown on sapphire or Si, despite the large mismatch of their lattice parameters and differences in their thermal expansions [2]. The epitaxial strain is relieved in thicker films by nucleating extended defects, whose characters are different in wurtzite and zincblende GaN [3].

The wurtzite III-nitrides contain a large density of threading dislocations (TDs), which extend from the film-substrate interface towards the surface. Naresh-Kumar et al. [4] have estimated that a majority of TDs in GaN films grown on sapphire are of the edge character (60%), about 38% are of the mixed, and less than 2% of the screw character. Similar results were obtained by Datta et al. [5]. Hino et al. [6] observed that screw and mixed TDs act as non-radiative recombination centers, whereas a majority of edge dislocations do not lead to non-radiative recombination. This seems to provide a plausible explanation why TDs in GaN are not as detrimental to optical properties as in GaAs, where similar densities of TDs completely quench the luminescence. Interestingly, somewhat different conclusions about the recombination activity of the three types of TDs were drawn by Yamamoto et al. [7], Albrecht et al. [8], and in a more recent work of Naresh-Kumar et al. [4], where edge and mixed TDs are identified as primary non-radiative recombination sources of charge carriers.

Much effort has been devoted to investigating the structures of TDs in III-nitrides (mostly GaN) using both experimental and computational methods. On the experimental side, most studies used transmission electron microscopy (TEM) to determine the types of TDs [9], to analyze the structures of dislocation cores by Z-contrast imaging [10,11], and to determine the sizes of surface depressions at the locations, where TDs emanate on the surface of the film [6]. Atomic force microscopy was used mainly to map the surface morphology around larger defects such as nanopipes at the cores of screw TDs and spiral hillocks [12]. The computational studies of TDs in GaN were made using empirical Stillinger-Weber [13] and Tersoff-Brenner potentials [14], tight-binding calculations [15], and by the density functional theory [16,17].

The advantage of using zincblende over the wurtzite III-nitrides is that the former does not exhibit spontaneous polarization and has a lower bandgap. The zincblende GaN is a promising material for development of LEDs that have high efficiency when emitting in the green part of the spectrum and thus provide a means of solving the “green gap” problem [18]. This challenge can be targeted using a large concentration of In inside quantum wells in wurtzite

GaN (optically active parts of the device), but its presence inevitably leads to larger lattice mismatch. This problem is not solved easily in wurtzite III-nitrides, where In causes large internal electric fields that separate charge carriers and thus reduces their recombination efficiency. On the other hand, zincblende III-nitrides do not exhibit spontaneous polarization and their smaller bandgaps make the green emission possible with lower In content. Since the zincblende phase of GaN is only metastable, it is prone to formation of stacking faults, which facilitate local transformations into the more stable wurtzite structure. The formation mechanism of these stacking faults is not yet understood, which is a severe obstacle to improving the luminous efficiency of GaN in the green part of the spectrum.

2 Fundamental physics of III-nitrides

2.1 Bandgap, emission spectrum and bonding

The III-nitrides are direct wide-bandgap semiconductor materials commonly used in electronic and optoelectronic applications [19,20]. It includes AlN, GaN and InN, but most of the applications are based on GaN and its alloys. Blue and white LEDs based on GaN are now an industry standard and are used in LED displays and many lighting applications. GaN-based laser diodes made Blue-ray technology possible. III-nitrides and their alloys have a wide range of possible bandgap energies ranging from 0.8 eV for InN, via 3.4 eV for GaN, to 6.1 eV for AlN [19]. Combining these materials to form (Al,In,Ga)N alloys opens the possibility to tune the bandgap and thus to achieve the emission of light with wavelengths anywhere from infrared to deep ultraviolet, as depicted in Figure 2.1.

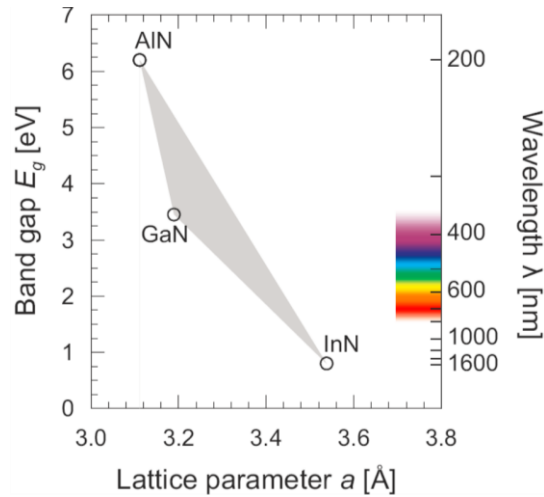


Figure 2.1: Bandgaps and wavelengths of pure wurtzite III-nitrides (circles) and their variations with the lattice parameter of the (Al,In,Ga)-N alloy (gray area). The color spectrum of the visible light (approx. 400-700 nm) is added for clarity [21].

All III-nitrides have a predominantly covalent character of bonds with varying ionic contribution that depends on the difference $|\chi_{III} - \chi_N|$ of the Pauling electronegativities χ_{III} of the group III-A (13th group of the periodic table) element and χ_N of nitrogen [22]. The values between 0 and 0.5 indicate a predominantly covalent bond, between 0.5 and 1.6 a combination of covalent and ionic bond, and above 1.6 a predominantly ionic bond. In the case of III-nitrides, the differences of Pauling electronegativities of the two ions are approximately 1.43 for GaN, 1.23 for AlN, and 1.26 for InN. The strongest ionicity is thus anticipated for GaN, and somewhat weaker for both AlN and InN.

2.2 Crystal structures

Under ambient pressure III-nitrides adopt either cubic structure (B3 zincblende/sphalerite, $F\bar{4}3m$, No. 216) or hexagonal structure (B4 wurtzite, $P6_3mc$, No. 186). They differ mainly by their stacking sequence, AaBbCc for zincblende and AaBb for wurtzite. These structures and their stacking sequence are shown schematically in Figure 2.2(a) and (b), respectively.

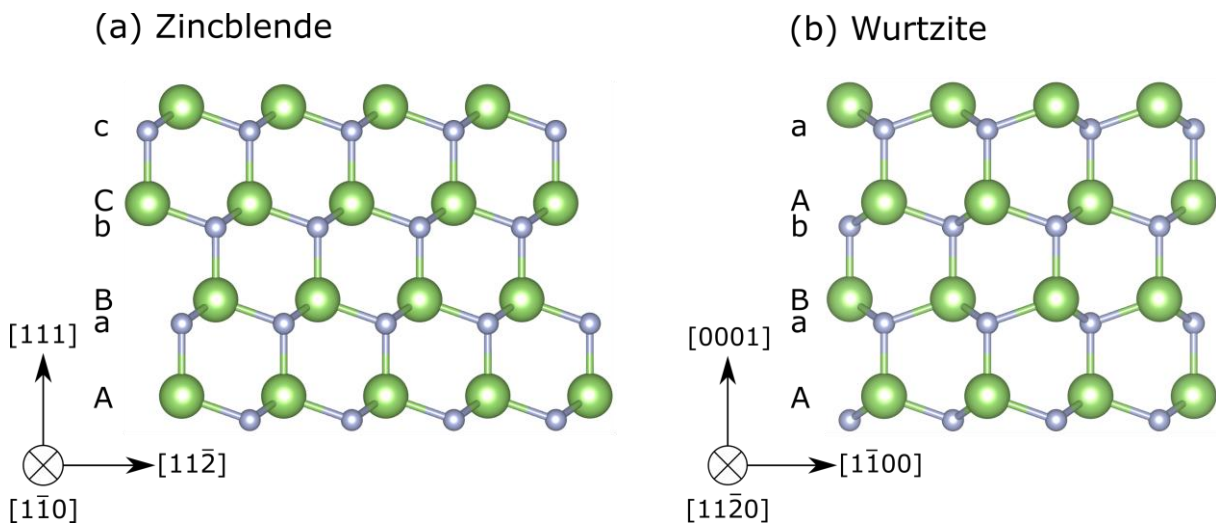


Figure 2.2: Different stacking sequences of (a) zincblende, and (b) wurtzite structures of III-nitrides. The large green spheres correspond to III-A group elements (Al, Ga, In) and the small gray spheres to N atoms.

The zincblende structure can be described as two interpenetrated face-centered cubic (FCC) sublattices, each of which containing a different atomic type. These sublattices are mutually shifted by $a/4[111]$, which results in a conventional unit cell with 8 atoms (4 of each type). The stacking sequence of the zincblende structure in the $\langle 111 \rangle$ direction is AaBbCc, where A, B, C represent the first sublattice and a, b, c the second sublattice. Each atom in this structure is coordinated tetrahedrally with 4 atoms of the other type. The zincblende structure and its significant projections are drawn in Figure 2.3.

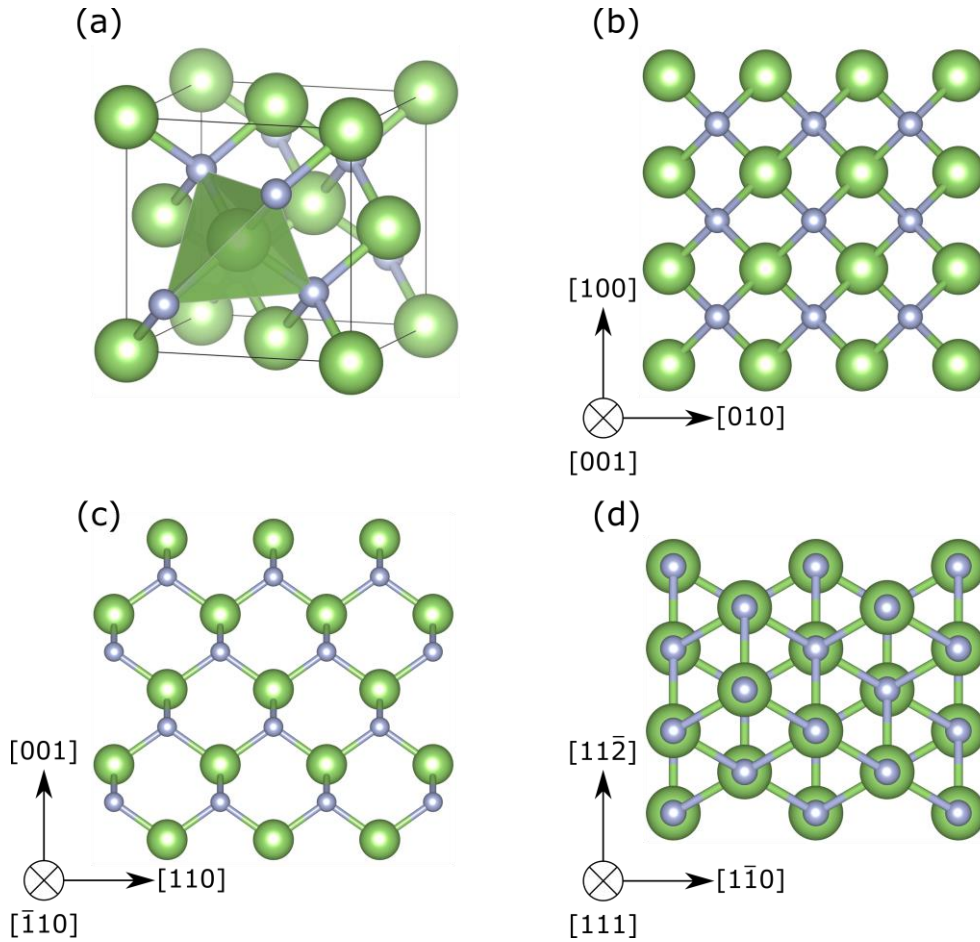


Figure 2.3: Zincblende crystal structure of III-nitrides in four characteristic projections. The assignment of individual atomic types is the same as in Figure 2.2.

The wurtzite structure is represented by two interpenetrated hexagonal close-packed (HCP) sublattices mutually displaced in the c -direction by $u = 0.375c$, where c is the lattice constant in [0001] direction of the parent HCP structure. The conventional unit cell is formed by 4 atoms (2 of each type). It is described by an alternated stacking of close-packed planes with AaBb stacking, where A, B represent the first sublattice and a, b the second sublattice. Each atom is again coordinated tetrahedrally with 4 atoms of the other type. The wurtzite structure and its significant projections are shown in Figure 2.4.

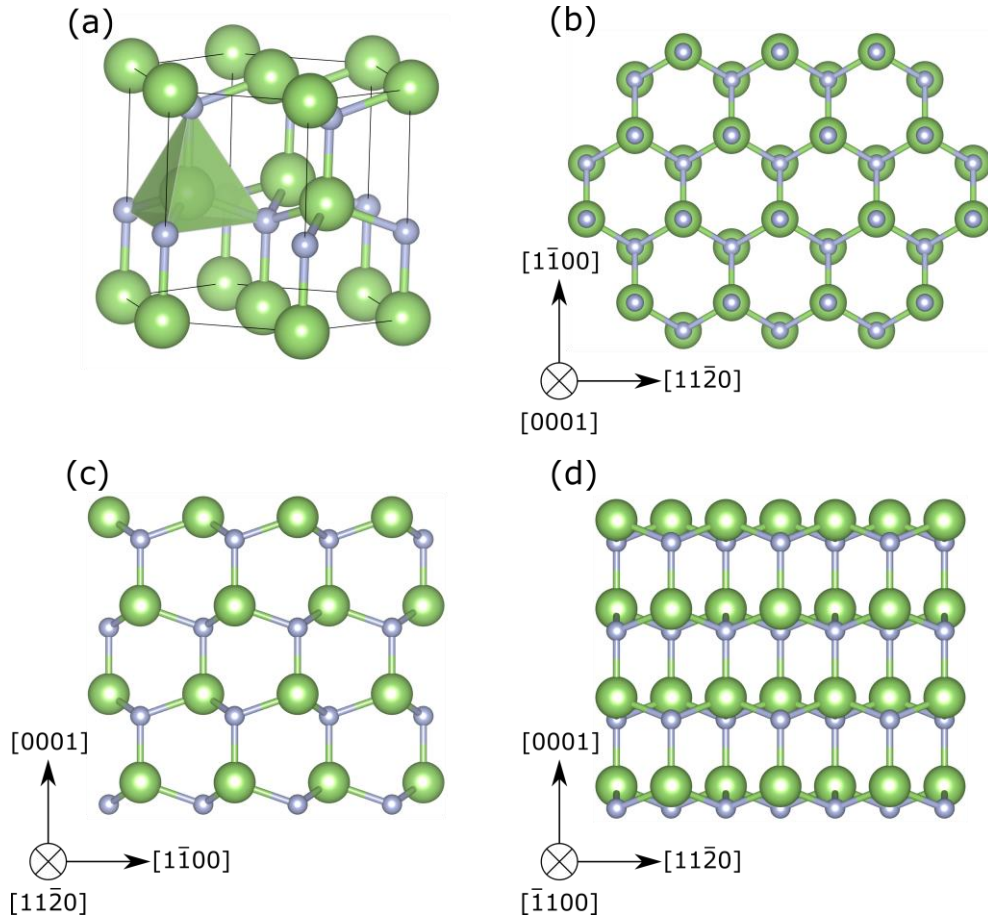


Figure 2.4: Wurtzite crystal structure of III-nitrides in four characteristic projections. The assignment of individual atomic types is the same as in Figure 2.2.

The energy differences of the wurtzite structure relative to zincblende, calculated by the density functional theory (DFT) [23], are -18.41 meV/atom for AlN, -9.88 meV/atom for GaN, and -11.44 meV/atom for InN. Clearly, wurtzite structure is more energetically favorable compared to zincblende, and thus the former represents the ground state structure. The largest energy difference corresponds to AlN, which is the least likely to transform into the zincblende phase. The smallest difference is obtained for GaN, which may thus exhibit a coexistence of zincblende and wurtzite structures in regions subjected to finite internal strains. The zincblende phase can be stabilized by heteroepitaxial growth of III-nitrides on cubic substrates such as 3C-SiC [24], GaAs [25], or patterned Si [26].

2.3 Defects and their physical properties

The physical properties of crystalline materials are to a large extent governed by lattice defects. The materials crystallizing in high-symmetry structures possess many available slip systems and their plastic deformation takes place preferentially by stress-controlled and

temperature-assisted dislocation glide on these systems [27]. On the other hand, low-symmetry crystal structures have much fewer slip systems and deform predominantly by twinning [28].

2.3.1 Point defects

Point defects play an important role in semiconductors. Impurities introduced into the crystal lattice can create shallow energy levels in the bandgap near the conduction and valence band edges and thus induce n-type or p-type conductivity [29], respectively. Moreover, they can also introduce deep level states in the bandgap, which act as trap states or recombination centers for charge carriers and thus reduce the device efficiency.

The main types of point defects are vacancies and impurity atoms (see Figure 2.5). There is a non-zero concentration of vacancies in every material, which is a consequence of the increase of entropy and the associated decrease of the Helmholtz free energy after introducing vacancies into the material [30]. Vacancies can be also introduced into the material during growth. Unlike vacancies, impurity atoms can occupy both lattice sites (substitutional impurities) and interstitial sites in the crystal (interstitial impurities). The substitutional defect forms preferentially when the “size” of the impurity atom is similar or larger than the size of the host atom, whereas the interstitial defect forms if the impurity atom is much smaller and can fit into the interstitial sites of the crystal lattice.

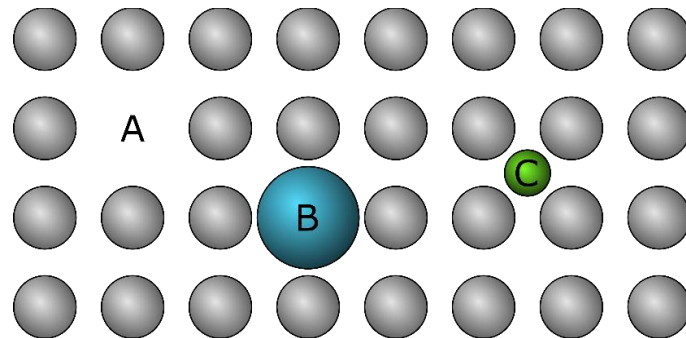


Figure 2.5: Schematic illustration of point defects in a square lattice: A – vacancy, B – substitutional impurity atom, C – interstitial impurity atom.

All point defects induce long-range strain fields that have different characters in purely covalent crystals (such as Si) and in ionic-covalent solids (such as III-nitrides). In the former case, vacancies create “wrong bonds” between like atoms and thus local failures in the coordination of atoms. In partially ionic bonded III-nitrides, the effect of vacancies is further strengthened by the creation of repulsive (+)(+) and (-)(-) bonds between the first atomic neighbors with the resulting electrostatic repulsion propagating to large distances.

2.3.2 Dislocations

Dislocations are line defects in crystals that are described by the Burgers vector and the orientation of the dislocation line. The glide plane on which the dislocation moves is defined as the plane that contains both these vectors. Depending on the orientation of the dislocation line and the Burgers vector, we recognize the edge, screw and mixed dislocations. The Burgers vector of an edge dislocation is perpendicular to the dislocation line and thus its glide plane is well-defined. As shown in Figure 2.6(a), a perfect edge dislocation exists in the part of the crystal that contains locally an extra half-plane of atoms in an otherwise perfect crystal lattice. The Burgers vector of a screw dislocation is parallel to the dislocation line, as shown in Figure 2.6(b). Therefore, the glide plane of screw dislocations is not defined uniquely as for the edge dislocations and can be generally any plane in the zone of the Burgers vector. In practice, the glide planes of screw dislocations are frequently low-index planes compatible with the given crystal structure [27,30]. The remaining (mixed) dislocations are characterized by the Burgers vectors with both edge and screw components and its glide plane is also fixed.

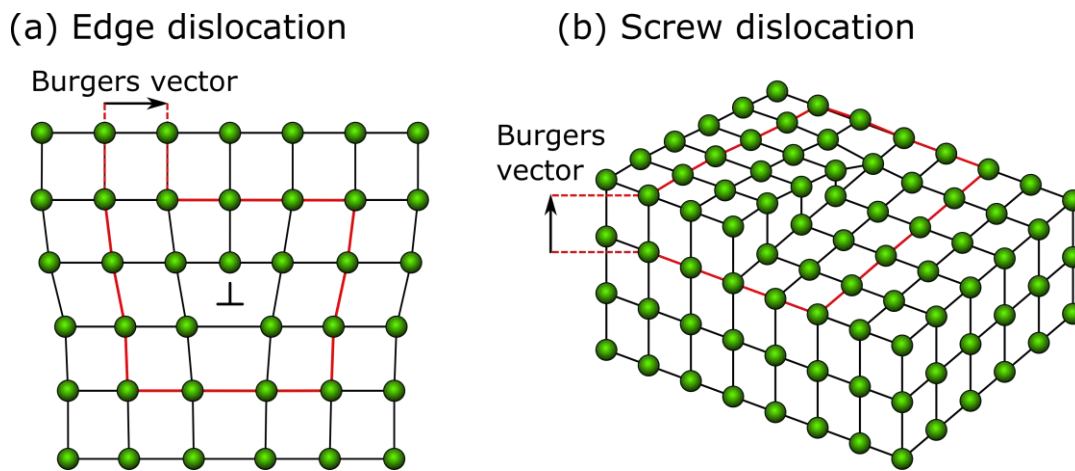


Figure 2.6: Schematic illustration of (a) edge dislocation, (b) screw dislocation in the simple cubic structure. The Burgers vector represents the closure failure of the Burgers circuit shown in red.

It is important to emphasize that the Burgers vector of every dislocation is conserved along its length. However, this is not the case for the tangential vector of the dislocation line that depends on the local orientation of the dislocation. Dislocations cannot begin or end inside the crystal [27]. Therefore, they must form closed loops or begin/end at interfaces, surfaces or other dislocations. Besides perfect dislocations, whose Burgers vector is the shortest lattice vector in the lattice, the close-packed crystals with low stacking fault energy could contain partial dislocations separated by stacking fault ribbons. The Burgers vectors of these partial dislocations are fractions of the interatomic distance.

Dislocations associated with interfaces in layered and epitaxial structures are distinguished as misfit and threading dislocations (TDs). The role of misfit dislocations is to

relieve the interfacial strain arising from the mismatch of lattice parameters of the materials on the opposite parts of the interface [31]. The dislocation lines of these dislocations are located at the interface and the Burgers vector contains finite edge component in the plane of the interface. The associated strain fields lead to relaxation of the epitaxial strain. On the other hand, TDs start at the interface and penetrate the epitaxial film. They can have any character (edge, mixed, screw). Screw TDs create surface steps, which significantly lower the energy barrier for nucleation of subsequent layer of atoms [30].

Dislocations are commonly described by the angle between the Burgers vector and the vector of the dislocation line. Using this convention, pure edge dislocation can be described as a 90° dislocation, and pure screw dislocation as a 0° dislocation (even though it is rarely used for screw dislocations).

Most of the perfect dislocations in the diamond cubic and zincblende structures are 60° mixed or pure screw dislocations with $1/2\langle 110 \rangle$ Burgers vectors and dislocation line vectors oriented preferably in $\langle 110 \rangle$ directions. Both 60° and screw dislocations have their Burgers vectors and dislocation line vectors in one of the $\{111\}$ planes and thus are mobile. The 90° dislocation could result from a dislocation reaction involving 60° dislocations, e.g. $1/2[01\bar{1}] + 1/2[\bar{1}01] \rightarrow 1/2[\bar{1}10]$, where $[110]$ is the dislocation line vector in both cases. The resulting dislocation is a 90° perfect dislocation and is called Lomer dislocation. It is sessile because the dislocation line and the Burgers vector do not lie in any of the $\{111\}$ planes [30]. Because of the presence of the two sublattices in zincblende structure, a perfect dislocation can be created in the glide set or in the shuffle set. This is illustrated in Figure 2.7. The glide set dislocation is created if the atoms inside the rectangle defined by the points 1-3-4-6 are removed, and thus the glide plane of the dislocation is defined by the line 3-4. On the other hand, the shuffle set dislocation is created if the atoms inside the rectangle 1-2-5-6 are removed, and the glide plane is then defined by the line 2-5 [27].

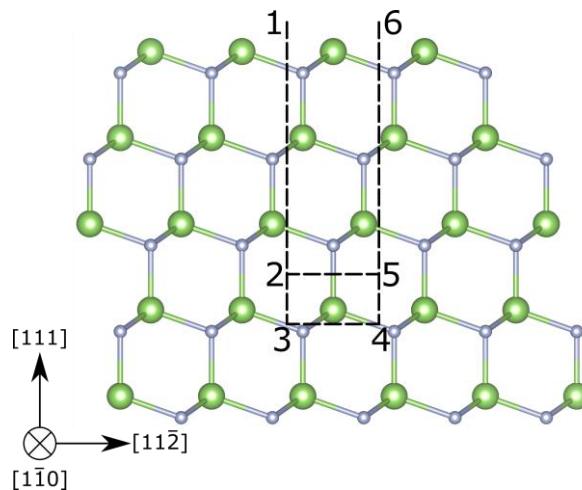


Figure 2.7: Illustration of the zincblende structure in the $[1\bar{1}0]$ projection and the section of atoms needed to create a glide (1-3-4-6) and shuffle (1-2-5-6) 60° dislocation.

Dislocations in wurtzite III-nitrides can have their Burgers vector either in the a -direction, in the c -direction or in both directions and thus can be denoted as a -type, c -type and $a+c$ -type, respectively. Possible Burgers vectors are $1/3[11\bar{2}0]$ for the a -type, $[0001]$ for the c -type and $1/3[11\bar{2}3]$ for the $a+c$ -type. If we assume that a particular TD has a dislocation line vector $[0001]$, the a -type dislocation is a pure edge, the c -type a pure screw, and $a+c$ -type a mixed dislocation. Two possible core structures of pure edge and screw dislocations in GaN obtained using the Tersoff-Brenner potential [32] are shown in Figure 2.8(a) and (b), respectively. The color coding here corresponds to energies of individual atoms (blue = lowest energy, red = highest energy). Only the bonds between the neighboring Ga and N atoms are shown for clarity, which shows the presence of “wrong” Ga-Ga and N-N bonds in the dislocation core. The same core structures were observed experimentally using aberration corrected scanning electron microscopy [33–35].

All types of TDs mentioned earlier are readily present in the III-nitride heteroepitaxial layers. The misfit dislocations in III-nitride heterostructures are 60° a -type mixed dislocations and they accommodate the mismatch strain and the island misorientation to substrate, which was analyzed by Mante et al. [36].

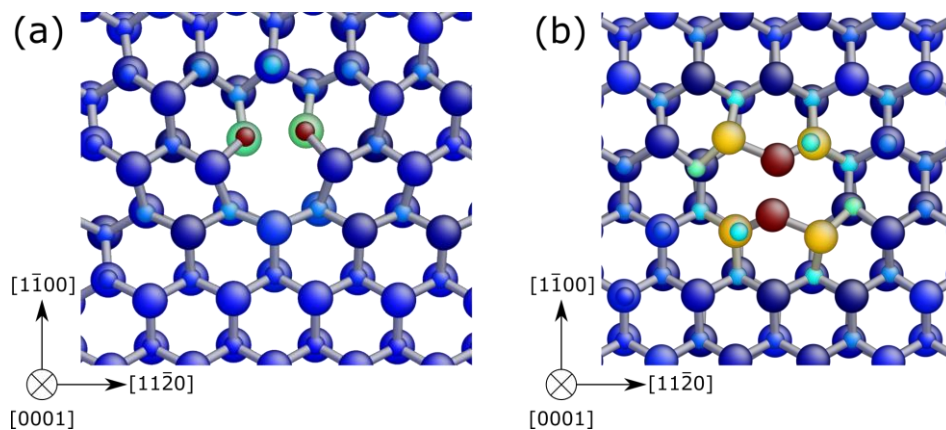


Figure 2.8: Two equilibrium core structures of the pure edge dislocation (a) and pure screw dislocation (b) obtained from atomistic calculations by Gröger et al. [14]. The color coding here corresponds to energies of individual atoms (blue = lowest energy, red = highest energy).

Threading dislocations in III-nitrides are believed to act as sources of non-radiative recombination of charge carriers [37]. However, DFT calculations and the measurements of cathodoluminescence do not agree unanimously on the recombination strengths of individual types of TDs. In particular, the DFT simulations of Elsner et al. [16] show that open-core screw dislocations and threading edge dislocations with full cores do not generate deep levels within the bandgap and thus they do not represent sources of non-radiative recombination. Whereas the cathodoluminescence measurements of Yamamoto et al. [7] and Albrecht et al. [8] confirm that screw dislocations are not recombination-active, both edge and mixed dislocations are predicted to be non-radiative recombination centers whose strengths are influenced by impurity gettering.

2.3.3 Stacking faults

The stacking fault (SF) is a planar defect that leads to a failure in the perfect stacking of crystallographic planes. We recognize intrinsic and extrinsic SFs. The intrinsic SF is described as a missing plane of atoms. If we consider a perfect stacking sequence as ABCABC, the stacking sequence of intrinsic SF is ABCBCABC, where the A plane is missing. The extrinsic SF is described as an extra plane of atoms, which results in the stacking sequence ABCBABC, if an extra B plane is added. Both types of SFs are illustrated in Figure 2.9.

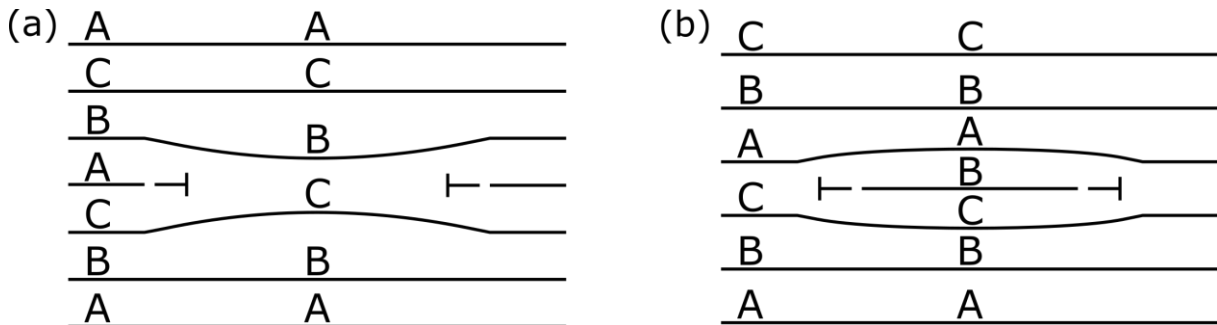


Figure 2.9: Illustration of (a) intrinsic SF (A plane missing), and (b) extrinsic SF (an extra B plane) in material with ABCABC stacking sequence with the corresponding partial dislocations.

The stacking faults in the zincblende structure can be formed on $\{111\}$ planes with ABCABC stacking. These faults can end on the surface or be bounded by a partial dislocation loop. We recognize Shockley and Frank partial dislocations. The Shockley partial dislocations in the zincblende structure have Burgers vectors $1/6\langle 112 \rangle$. They are products of the dissociation of a perfect $1/2\langle 110 \rangle$ dislocations and are glissile. According to Frank's rule, dissociation of a perfect dislocation into two partials is energetically favorable. The resulting Shockley partials bound an intrinsic SF and their separation depends on the energy and stability of this SF. Frank partial dislocations have Burgers vectors $1/3\langle 111 \rangle$, are sessile, and can be either positive or negative. A negative Frank partial dislocation terminates a missing $\{111\}$ plane of atoms. Therefore, it bounds an intrinsic SF, as illustrated in Figure 2.9(a). On the other hand, the positive Frank partial dislocation terminates an extra $\{111\}$ plane of atoms that can be created by a precipitation of interstitial atoms [30]. Positive Frank partials bound an extrinsic SF, as shown in Figure 2.9(b).

A stacking fault in the zincblende structure can be created in the glide or shuffle set, as is shown in Figure 2.10. For SFs in the shuffle set, the crystal would be cut between the Bb layers with upper or lower part of the crystal displaced in the direction of the fault vector that lies in the plane of the SF. On the other hand, the SF in the glide set is created by making a cut between the Cb layers and displacing the upper or lower part of the crystal similarly as for the shuffle set. Most of the SFs created in this way are unstable because the energy of the crystal can be

lowered by removing the fault. In zincblende GaN, metastable SFs can be created only in the glide set, as was calculated by Antoř et al. [38].

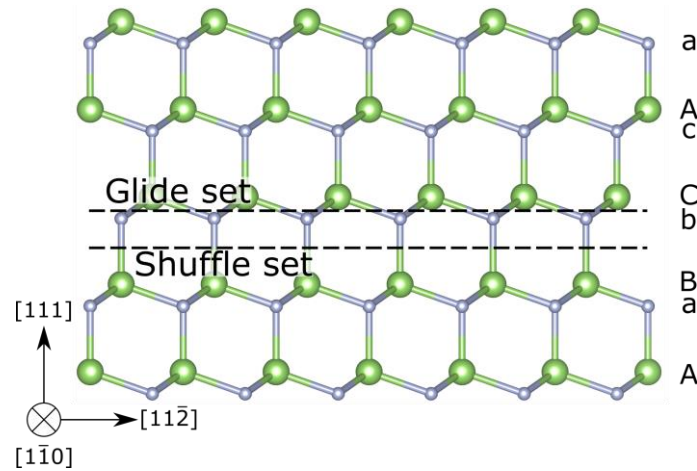


Figure 2.10: Illustration of the zincblende structure in the $[1\bar{1}0]$ projection. The positions of planar cuts that result in SFs in the glide and shuffle sets are drawn by dashed lines.

Stacking faults in the wurtzite structure can occur on the $\{0001\}$ planes and on $\{11\bar{2}0\}$ planes, which are then called basal and prismatic SFs, respectively. On the basal plane, there are two possible intrinsic and one extrinsic SF. The I_1 intrinsic SF has ABACACA stacking and the I_2 intrinsic SF has ABABCACA stacking. The stacking of the extrinsic SF is ABABCABAB, where the C plane is inserted into the otherwise perfect stacking. The Shockley partial dislocations have $1/3\langle 1\bar{1}00 \rangle$ Burgers vector and are glissile. The Frank partial dislocations have $1/2\langle 0001 \rangle$ and $1/6\langle \bar{2}203 \rangle$ Burgers vectors and both are sessile [27]. The prismatic SFs are bounded by partial dislocations with $1/2\langle 10\bar{1}1 \rangle$ Burgers vector. Also, prismatic SFs are able to fold from the prismatic plane into the basal plane [39]. Stair rod dislocation is located at the transition between basal and prismatic SF and its Burgers vector can be determined according to the dislocation reaction: $1/6[20\bar{2}3] + 1/6[10\bar{1}0] \rightarrow 1/2[10\bar{1}1]$.

2.4 Substrates

Unlike other semiconductor materials, group-III nitrides do not have a commercially available native lattice-matched substrate [1]. Most commercial applications thus rely on the use of foreign substrates with lattice parameters different from those of the III-nitride film, which leads to the nucleation of interfacial misfit dislocations and, in some cases, to cracking. The main parameters to consider when designing heteroepitaxial structures are the lattice mismatch between the epilayer and the substrate, and the differences of thermal conductivities of both materials. Other parameters to consider are the crystal structure, possible surface quality, reactivity, electrical properties, and availability. The previously mentioned properties

of substrates control the crystal orientation, polytype, polarity of wurtzite polytypes, surface morphology, strain and the density of defects in III-nitride epilayers [40].

Sapphire (single-crystal Al_2O_3) is by far the most widely used substrate for the epitaxial growth of wurtzite nitrides. It has low thermal conductivity, high electrical resistivity (it is an insulator), and is highly transparent in the infrared to ultraviolet region. The lattice mismatch of sapphire to GaN is approx. 15%, which is partially accommodated by nucleating interfacial misfit dislocations. Besides these dislocations, GaN films grown on sapphire also contain a large density of TDs [41], whose existence cannot be predicted from simple arguments based on linear elasticity. The thermal expansion coefficient of sapphire is larger than that of GaN, thus compressive strain in GaN is induced upon cooling. Sapphire surface is often nitridated to form AlN buffer layer for further growth of GaN, which improves wetting characteristics and reduces the defect density [42].

Silicon carbide (SiC) generally has a lower lattice mismatch to GaN than sapphire, higher thermal conductivity and can be conductive if doped, but it is also more expensive. SiC has many polytypes, but only a few are used for group-III nitride epitaxy. Commercially available are its 6H and 4H hexagonal polytypes, which belong to the same $P6_3mc$ point group as wurtzite nitrides. AlN buffer layer is again used for improving wetting characteristics and nucleation [42]. 3C-SiC cubic polytype can be used to stabilize the growth of zincblende GaN [24], but it is only available as an epilayer on Si substrate.

Silicon (Si) is an attractive substrate for nitride epitaxy because it is cheap and readily available, its crystal quality and surface finish are superior to any other semiconductor material, and the Si technology is well-developed. Using Si as the substrate for nitride growth has significant drawbacks as well. Crystal quality of these layers is worse than on any other substrate previously mentioned. The mismatch of lattice parameters and thermal conductivities between Si and GaN or AlN is very large and Si has the tendency to form amorphous SiN_x layer when exposed to reactive nitrogen species [42]. Much effort has been invested in improving the growth of III-nitrides on Si, which has led to significant improvements in the efficiency of LEDs, laser diodes, and high electron mobility transistors.

2.5 Electron beam induced current

Electron beam induced current (EBIC) is a technique used in scanning electron microscopy to study electrical properties of semiconducting materials. It can be used to characterize the electrical activity of defects present in materials and also material properties like carrier lifetime, diffusion length and surface recombination velocity. For in-depth look on the EBIC method see ref. [43,44].

The basic principle of EBIC is that the sample is irradiated by high energy electrons, which are able to excite electrons in the sample from the valence into the conduction band, thereby creating electron-hole pairs. Current associated with these charge carriers can be collected and measured by an external ammeter. Electron-hole pairs generated by the electron beam diffuse away into the surrounding area and recombine in the process. In the presence of the internal electric field, the movement of electron-hole pairs is no longer random, but is directed by the electric field, which allows their collection and detection in the external circuit.

In the EBIC measurements, the internal electric field is mostly induced by the p-n junction already present in the sample or by a Schottky junction intentionally created for the EBIC measurement. The contrast comes from the difference of collected charge across the sample, which might be caused by the number of generated and recombined charge carriers, presence of p-n or Schottky junctions, impurities, or space charge regions. Defects like dislocations and point defects are usually associated with increased recombination rate, thus drops in the induced current indicates the position of these defects. The current always flows in the direction opposite to current under forward bias since minority carriers are responsible for the induced current.

A commonly used configuration for the EBIC measurement is when the sample contains p-n junction or Schottky junction connected to the ammeter by two contacts. Two orientations of sample are possible. The top view is used for identification of the positions of defects in the sample and the electron beam is scanned perpendicular to the sample surface. Alternatively, the sample can be cleaved, and its cross-section analyzed. This configuration may be used, for example, for the minority carrier diffusion length measurement or for identifying the positions of p-n junctions in layered structures. All possible configurations are depicted in Figure 2.11. If the sample does not contain any p-n or Schottky junction, it is necessary to create one to be able to detect any EBIC current. Fortunately, the Schottky junction can be easily created by depositing a thin layer of metal on the sample surface. The layer should be thin enough to be electron transparent (usually less than 20 nm) for it not to conceal the surface topography and also not to induce lateral scattering of the electrons in the metal layer. Low resistance contacts leading to the ammeter are also necessary for successful EBIC measurements.

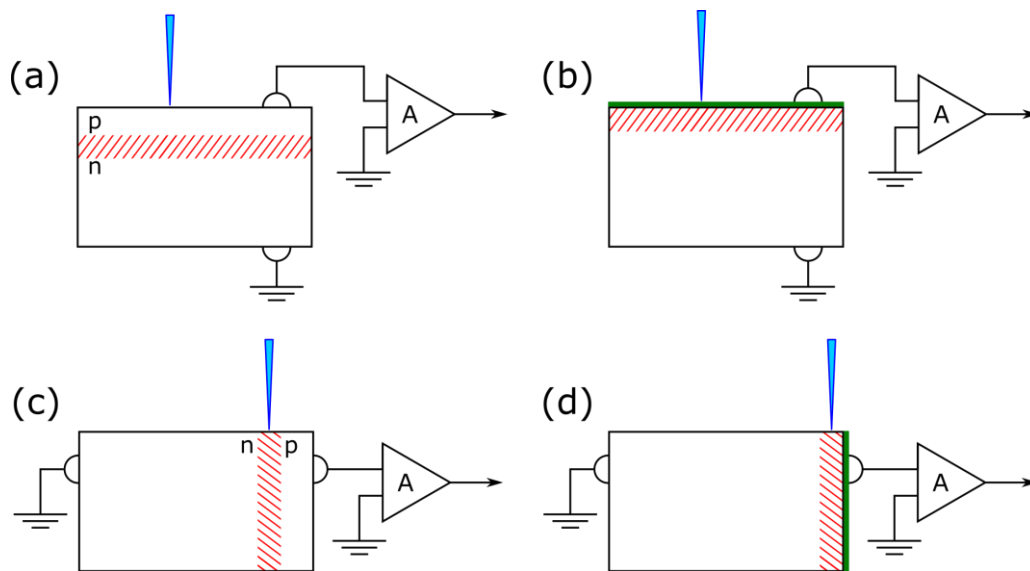


Figure 2.11: The possible configurations for the EBIC measurement: (a) top view with p-n junction, (b) top view with Schottky junction, (c) cross-sectional view with p-n junction, and (d) cross-section view with Schottky junction, where the direction of the electron beam is illustrated as blue line, the space charge region is highlighted by red cross-hatching and Schottky junction is highlighted as the green line.

For non-semiconducting materials, this method is only able to accurately measure the current absorbed by the sample and only one contact is necessary for this measurement. However, there exists another method using one contact, which is called the electron beam absorbed current (EBAC). This can be used in semiconductors to investigate the continuity of electrical circuits in semiconducting devices, for example, microprocessors. In EBAC, one contact is connected to the circuit and the electron beam is scanned across the investigated area. Differences in the collected current reveal whether a part of the circuit is connected to the contact or there is a discontinuity in the circuit. By changing the energy of primary beam, electrons can penetrate into different depths of the sample and thus probe circuitry in different layers of the microchip.

The most notable artifact experienced in this work is “tailing” after an abrupt change of contrast (Figure 2.12). This is caused by insufficient speed of the amplifier, which outputs the data more slowly than the electron beam moving to the next pixel. It is especially noticeable with rapid scan rates, where the tailing gets elongated. Fortunately, decreasing the scan speed is sufficient to eliminate this artifact.

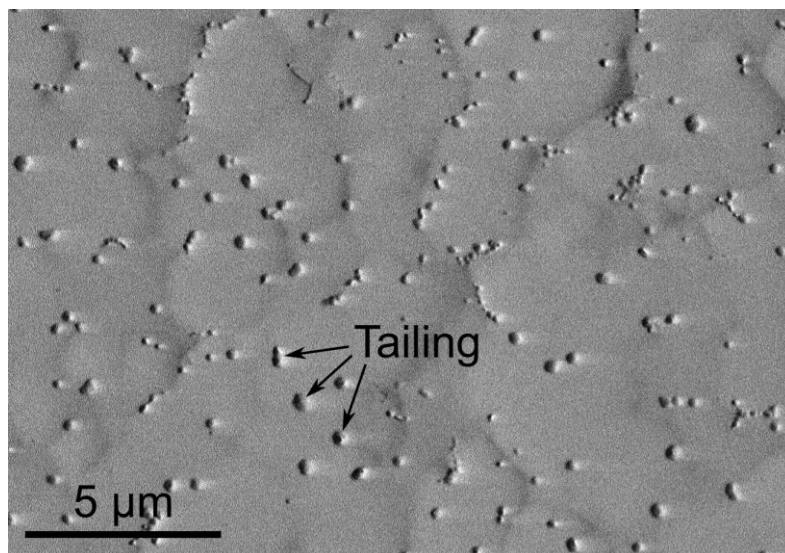


Figure 2.12: The EBIC image of GaN/AlN/Si (111) where the tailing artifacts due to high scan rate are easily apparent.

3 Aims of thesis

III-nitrides can adopt wurtzite (stable) and zincblende (metastable) structures. III-nitrides crystalizing in these structures exhibit different physical properties and completely different structures of extended defects. Wurtzite III-nitrides are populated by threading dislocations that are anchored at the interface and emanate on the surface of the film. However, zincblende III-nitrides are mainly plagued by stacking faults and associated partial dislocations, which facilitate partial transformations into the more stable wurtzite structure.

The aim of this Thesis is to investigate the structural and physical properties of extended defects in III-nitrides, especially focusing on their origin, nucleation and physical properties. We have concentrated on characterizing the major types of extended defects that form in both structures in response to epitaxial strain arising from the mismatch of their lattice parameters. Multiple advanced microscopy techniques, predominantly transmission electron microscopy, were used in this study. AlN/Si (111) and GaN/AlN/Si (111) heterostructures were used to study defects in wurtzite III-nitrides and GaN/SiC/Si (001) was used for zincblende nitrides.

The goal of this dissertation project is to investigate the following problems and provide plausible arguments that can be used for further advancements of epitaxial growth of these heterostructures:

- Wurtzite III-nitrides
 - Describe the structures of threading dislocations.
 - Identify the origin of threading dislocations.
 - Do all threading dislocations act as non-radiative recombination centers?

- Zincblende III-nitrides
 - Describe the structures of stacking faults.
 - Identify the partial dislocations that bound stable stacking faults.
 - How do stacking faults interact with each other?

Answering these questions will lead to better understanding of nucleation of defects in these materials, which can also lead to new methods of defect reduction.

4 Materials and methods

4.1 Atomic force microscopy

The topography of samples was analyzed by atomic force microscopy (AFM). Conventional tapping mode or Bruker's proprietary PeakForce Tapping was used for the imaging. Tapping mode was used for the images with imaging area larger than $5 \times 5 \mu\text{m}$ using the probes RTESPA-300 with nominal tip radius of 8 nm. The PeakForce Tapping uses the ScanAsyst-Air probe with a smaller nominal tip radius of 2 nm and, therefore, it is sufficient for the higher resolution imaging. Both imaging modes were performed on the Bruker Dimension Icon located in the CEITEC Nano core facilities and Bruker Dimension Icon located at the Department of Material Science & Metallurgy, University of Cambridge.

4.2 Scanning electron microscopy

Scanning electron microscopy (SEM) was used for the sample surface topography analysis and for analysis of defect recombination properties using the electron beam induced current (EBIC). Samples for the EBIC measurement were first coated by 5 nm of Au or 3 nm Ni and 3 nm Au to create the Schottky junction necessary for rectification of the induced current flowing through the sample. SEM imaging was performed on the Tescan Lyra 3 XMH microscope, whereas the EBIC measurements were made by the Mighty EBIC 2.0 detector (Ephemeron Labs), both at the Institute of Physics of Materials, Czech Academy of Sciences. Focused ion beam (FIB) in SEM was used to prepare samples for further analysis using transmission electron microscopy.

4.3 Transmission electron microscopy

Transmission electron microscopy (TEM) and scanning transmission electron microscopy (STEM) were used to study crystallographic defects present in the layers. Both diffraction contrast and high-resolution imaging were used for imaging these defects. Plan view samples were prepared by mechanical grinding and polishing with final Ar^+ -ion polishing to electron transparency. Cross-sectional samples were prepared either by mechanical grinding, polishing, and Ar^+ -ion milling or by the FIB milling and polishing in the scanning electron microscope. Microscopes used in this thesis were FEI Titan located in the CEITEC Nano core facilities and at the Department of Material Science & Metallurgy, University of Cambridge, FEI Tecnai F20 located also at the University of Cambridge, and Jeol JEM-2100F located at the Institute of the Physics of Materials, Czech Academy of Sciences.

4.4 X-ray diffraction

X-ray diffraction experiments were performed using Cu K α source ($\lambda = 0.154056$ nm) in Philips X'pert diffractometer located at the Department of Material Science & Metallurgy, University of Cambridge. Standard ω - 2θ scans were performed in order to analyze crystal structure, relative amount of material deposited, and strain in the layers.

4.5 Correlative probe and electron microscopy

Correlative probe and electron microscopy (CPEM) is based on measuring the signals from scanning probe and from electron microscope at the same time. This is achieved by inserting LiteScope scanning probe microscopy (SPM) module (NenoVision) into the Tescan Lyra 3 XMH electron microscope, both located at the Institute of Physics of Materials. The scanning is carried out by controlled movement of the LiteScope stage and the signals from both probes are acquired for each pixel. The AFM and SEM probes are stationary and are separated by a few hundreds of nm. Their mutual separation remains fixed during the image acquisition, which results in an offset between the two images which corresponds to their separation. The obtained images are overlaid, and the edges cropped. This results in a three-dimensional image, where the topography typically corresponds to surface morphology and the surface is colored according to a signal from the electron microscope.

5 Results and discussion

5.1 Defects in wurtzite AlN and GaN

We have used samples of GaN/AlN or AlN grown on Si (111) substrate by metal-organic chemical vapor deposition (MOCVD) in ON Semiconductor. Due to the growth on Si (111) substrate, all samples possess wurtzite crystal structure and are highly crystalline. The characterization of TDs in these samples was made by: (i) transmission electron microscopy (TEM), and (ii) atomic force microscopy (AFM) and (iii) scanning electron microscopy (SEM) with electron beam induced current (EBIC).

5.1.1 Topography of AlN nucleation layers

Majority of defects in AlN are nucleated in the early stages of growth. Therefore, we have investigated the AlN nucleation layers (NLs) grown on Si (111) substrates by MOCVD to observe nucleation and coalescence of AlN islands and defects present in these NLs. The thicknesses of NLs ranged from 1 to 100 nm. The AFM topography images of NLs are shown in Figure 5.1. For the thickness of 1 nm and 5 nm, the NL exhibited separated islands. However, at 5 nm thickness some of them coalesced with other neighboring islands. Additionally, the islands in 1 nm thick NL are preferentially nucleated at step edges, which are visible in Figure 5.1 as brighter straight lines. The islands of 10 nm thick NL were interconnected and formed a network of islands separated by trenches. At the thickness of 30 nm the NL does not exhibit any islands, but rather a coalesced layer with holes. For thicker NLs, the character of the layers did not change, only some of the holes disappeared or left only a small dimple on the surface. Some holes developed into pronounced V-defects that grew in size with increasing thickness. The 100 nm NL was flat with small dimples on the surface and hexagonal-shaped V-defects.

The AlN layer exhibits the Volmer-Weber growth mode [45], because it nucleates first as individual islands which then coalesce and create a continuous layer. This growth mode is typical for the growth of III-nitrides, because they are usually grown on highly mismatched foreign substrates like Si or sapphire [46]. The coalescence occurs somewhere between 10 and 30 nm as is apparent from AFM images shown in Figure 5.1, where 10 nm sample has interconnected, but not fully coalesced islands, and 30 nm sample already has continuous AlN layer, albeit with many defects. We assume that the origin of some crystallographic or macroscopic defects like V-defects is in this coalescence stage. Samples with uncoalesced NLs did not exhibit any features on the island surface, but after coalescence, the layer contained a large number of holes or dimples, which in some cases developed into V-defects. Apart from the V-defects, the 30, 60, and 100 nm NLs exhibited small surface dimples, which might be surface terminations of TDs [47,48]. The main difference between V-defects and surface terminations of dislocations is that the size of a V-defect increases with increasing thickness [49], while the size of the surface termination of a dislocation remains the same. This will be discussed in more detail in the next section.

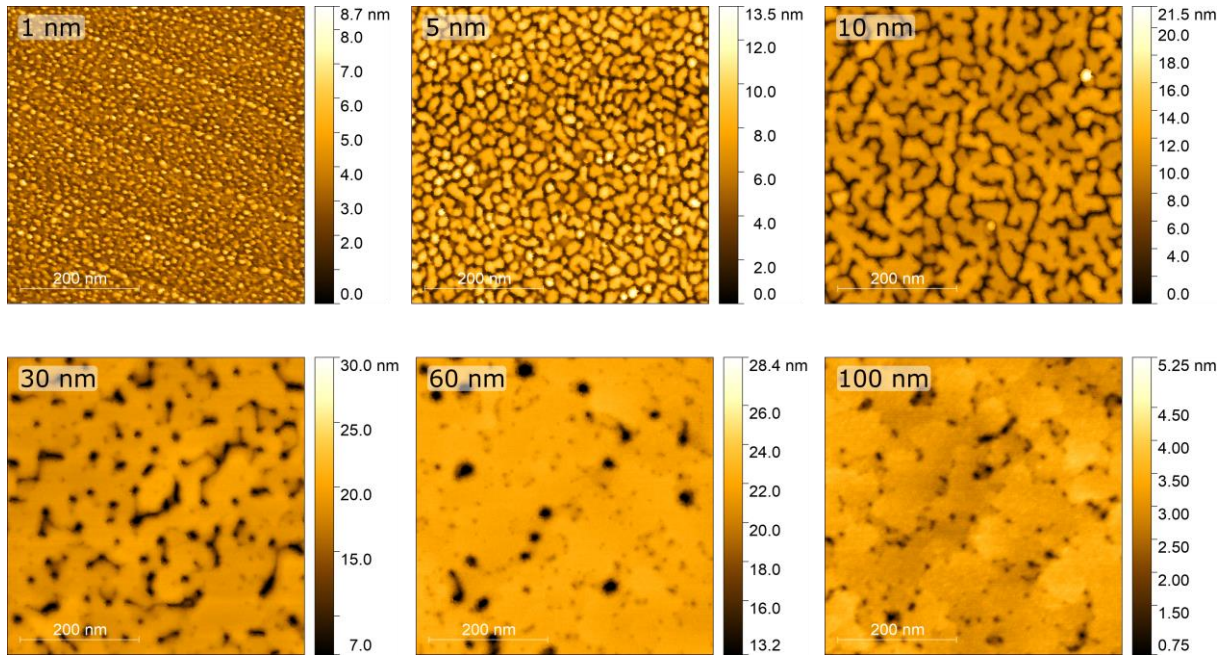


Figure 5.1: AFM images of the area of 500×500 nm for various thicknesses of AlN/Si (111) NLs.

5.1.2 Defects in wurtzite GaN and AlN

Epitaxial layers of wurtzite III-nitrides contain a variety of defects, most importantly dislocations. Both misfit and TDs are present in III-nitrides and will be considered in the following text. Misfit dislocations are present at or near the heteroepitaxial interfaces and relieve the lattice misfit strain. TDs have their dislocation line perpendicular to the interfaces and penetrate through the entire layer and terminate on the surface. Their origin is not well understood and will be discussed in this section. Additionally, possible interactions of dislocations and the amorphous interfacial layer will be considered.

Interfacial layer between AlN and Si

The interface between AlN and Si is not abrupt, as would be expected for an epitaxially grown layer, but the two are separated by an interfacial layer. This layer is visible in the high-resolution TEM image presented in Figure 5.2. It is apparent that the layer is composed of amorphous or highly defective material and has uneven thickness that ranges from 0.3 to 1.7 nm. The thickness variations of the amorphous layer are mainly present in the part facing AlN, but the thickness varies also in the part facing the Si substrate, however only by a few monolayers. Some areas at the AlN/Si interface do not have amorphous layer present, but these areas are usually small in size and a majority of the interface has the amorphous layer present. Despite the presence of the amorphous layer the AlN layer maintains the epitaxial relationship across the entire layer with the exception of small local rotational misalignments along the c axis.

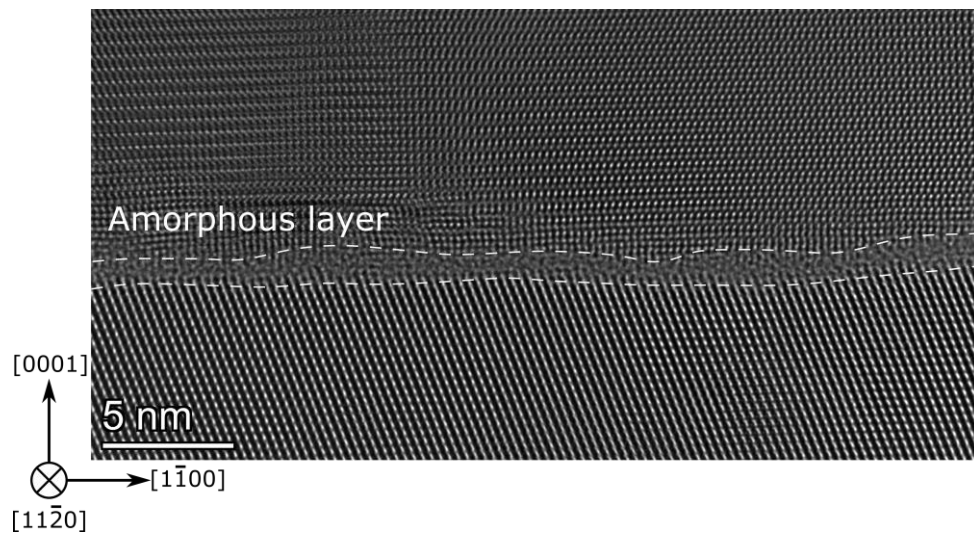


Figure 5.2: High-resolution TEM image of the AlN layer grown on Si (111) showing the amorphous interfacial layer between AlN and Si.

To further understand the origin of the amorphous layer, energy-dispersive X-ray spectroscopy (EDX) analysis in TEM was performed to obtain its chemical composition. An EDX line scan across the AlN/Si interface is shown in Figure 5.3, which reveals that the amorphous layer is composed of Si, Al, and N. The chemical composition does not change abruptly at the interface but varies continuously in approx. 5 nm range from pure Si to pure AlN. It is important to note that a higher beam current was used for EDX imaging and this resulted in lower resolution of the measurement and, consequently, in some overestimation of the thickness of the amorphous layer. One interesting thing visible from the line scan is that the concentration of N changes faster than the concentration of Al. This implies that some of the N reacts with Si to create SiN_x . Therefore, the whole amorphous layer is composed of varying concentrations of Si, SiN_x , and AlN. Similar conclusion was drawn by Radtke et al. [50].

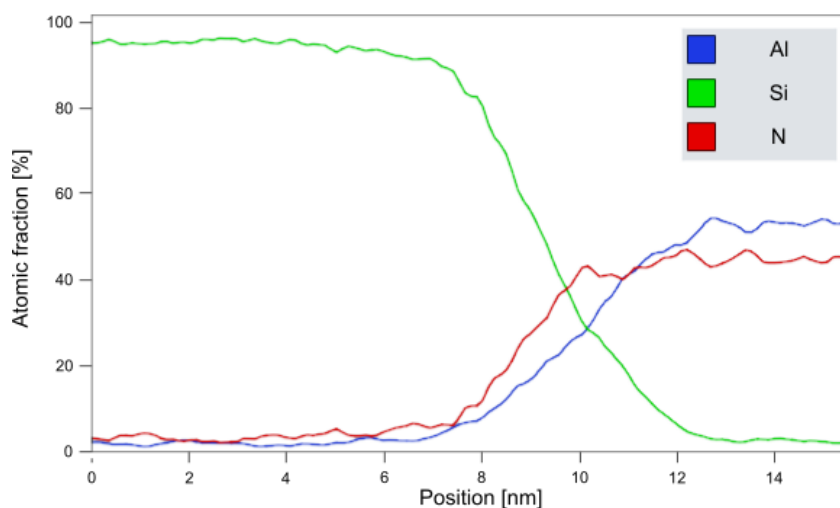


Figure 5.3: EDX line scan across the AlN/Si interface showing the change of the chemical composition of the amorphous layer.

There are several possible mechanisms for the formation of the amorphous layer. It can be either created during the initial stage of deposition or in the later stages due to the diffusion. During the initial stage, the active nitrogen species could react with the Si substrate forming SiN_x layer on the Si surface. The active nitrogen species are present during the growth of AlN layers, but its effect could be reduced by predose of Al precursor during the initial stage of growth as was discussed several times in the literature [51–53]. The SiN_x layer is then overgrown by AlN which could also adopt amorphous structure. If the SiN_x layer is not continuous, as we observe in our samples, the AlN layer could obtain epitaxial relationship from the area, where the SiN_x layer is not present, and during the lateral growth of the layer the epitaxial relationship would be extended to the areas covered with the SiN_x layer. This mechanism would reasonably explain the behavior we observe in the AlN layers.

Another possibility is that amorphous layer is formed after the initial deposition phase. The AlN layer is deposited on the Si surface and afterwards the SiN_x layer is formed due to the diffusion of N into Si or the diffusion of Si into AlN. High temperature during the growth is able to activate the diffusion and, consequently, the rearrangement of atoms is possible. This mechanism is supported by the fact that the interface between the amorphous layer and Si is not flat, which is apparent in Figure 5.2. This means that some of the Si atoms diffused into the amorphous layer. This mechanism is also suggested several times in the literature [54,55]. Some authors even suggest that the amorphous layer originates from the combination of diffusion and high misfit strain, which makes the interfacial area amorphous [56,57].

In conclusion, the amorphous layer present at the AlN/Si interface is composed of SiN_x and partially of amorphous AlN and could be formed by two mechanisms described above. We assume that a major part of the amorphous layer is formed during the initial deposition phase due to the reaction of nitrogen present in reactor atmosphere with Si surface. The resulting layer is unevenly distributed on the sample surface with some uncovered areas. Then some of the deposited AlN atoms adopt amorphous structure, but gradually, due to the lateral growth of

AlN from uncovered areas the AlN layer becomes single crystalline. The amorphous layer increases its thickness due to the diffusion of Si and N during the later stages of growth. However, we suggest that the diffusion is not the major formation mechanism, but rather a complementary one to the reaction of active N species with Si surface.

Stacking faults in AlN/Si (111)

One of the common extended defects in semiconductor materials are stacking faults (SFs). In the wurtzite III-nitrides, they can be present on the basal or prismatic planes. On the basal plane SFs can be bound by Shockley and Frank partial dislocations. Shockley dislocations have $1/3\langle 1\bar{1}00 \rangle$ Burgers vectors, while Frank partials have two possible types of Burgers vectors. Simple Frank partials have $1/2\langle 0001 \rangle$ Burgers vectors and the complex Frank partials have $1/6\langle 2\bar{0}23 \rangle$ Burgers vectors. The latter are composed of a simple Frank partial and a Shockley partial and could be described by the dislocation reaction $1/3[10\bar{1}0] + 1/2[0001] \rightarrow 1/6[2\bar{0}23]$. Even though the complex Frank partial is a vector connecting two atoms, it is not considered a perfect dislocation, because the two atomic sites do not have the same surroundings and its Burgers vector is not a lattice translation vector [30]. The prismatic SFs are bound by partial dislocations with the $1/2\langle 10\bar{1}1 \rangle$ Burgers vectors [39].

NLs with the thicknesses of 10, 30 and 100 nm were chosen for the TEM study. A representative plan view image of each sample is shown in Figure 5.4. The majority of defects present in those layers are TDs and prismatic SFs (TDs will be discussed in more detail in the next section). In the 100 nm sample there are mostly TDs and only occasional prismatic SFs. In the 30 nm sample there is lower number of TDs and more prismatic SFs than in the 100 nm sample. In contrast, the 10 nm sample contains only very few prismatic SFs, which are much shorter in length compared to the SFs in thicker layers.

Figure 5.5 shows a partial dislocation with the $1/2[0001]$ Burgers vector. Alternatively, it could have the Burgers vector of $1/6[\bar{2}023]$. These share the same $1/2[0001]$ edge component, but the $1/6[\bar{2}023]$ dislocation has an additional $1/3[10\bar{1}0]$ screw component, which is not visible in this high-resolution image. Therefore, these cannot be distinguished from the data available to us. However, both possible options are variations of Frank partial dislocations bounding a basal SF, which unravels the position of basal SF even though the discontinuity of stacking sequence is not visible in this projection.

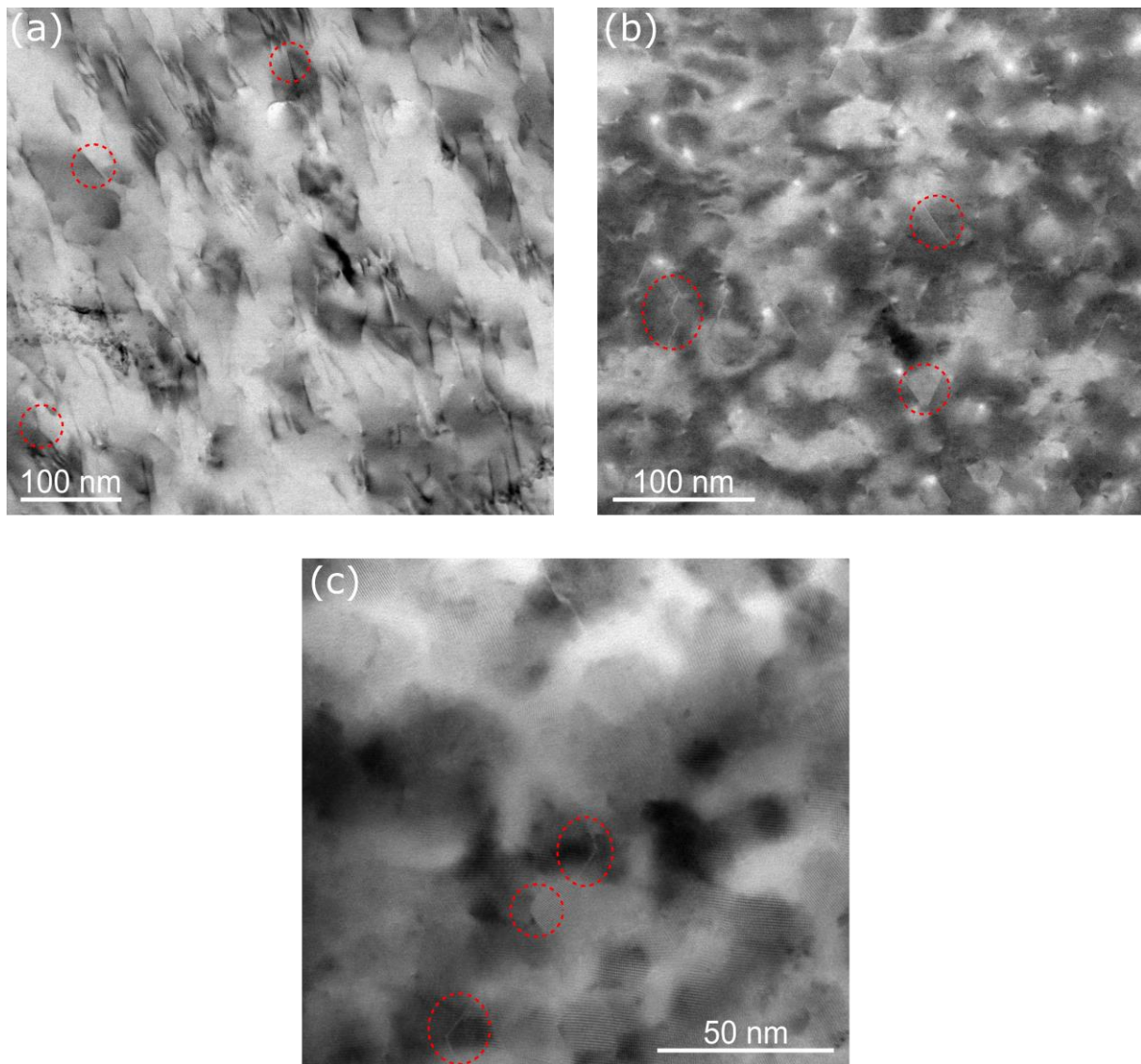


Figure 5.4: Plan view TEM images of AlN NLs on Si of various thicknesses, where some of the prismatic SFs are highlighted by red circles: (a) 100 nm thick layer STEM bright field image taken using diffraction condition $\mathbf{g} = \bar{1}101$ near $[2\bar{1}\bar{1}3]$ zone axis; tilting of approx. 32° from the foil normal is required to reach this imaging condition so that all TDs are represented as straight lines pointing in the same direction; (b) STEM bright field image of 30 nm thick layer taken using $\mathbf{g} = 2\bar{1}\bar{1}0$ near $[0001]$ zone axis; (c) TEM bright field image of 10 nm thick layer taken using $\mathbf{g} = 2\bar{1}\bar{1}0$ near $[0001]$ zone axis.

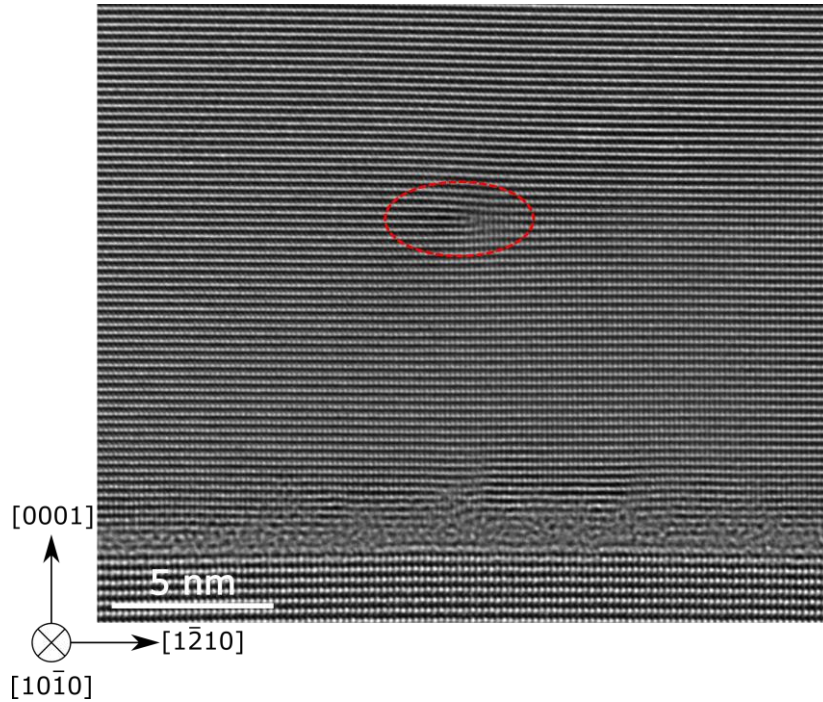


Figure 5.5: High-resolution TEM image of a dislocation in AlN/Si (111). This is identified as having the $[10\bar{1}0]$ dislocation line vector and $1/2[0001]$ visible Burgers vector.

Prismatic SFs were preferentially observed near the holes in the partially coalesced layer. This is shown in Figure 5.6. The holes in the layers are the areas between interconnected islands, which were described previously in more detail in the analysis of the topography in chapter 5.1.1. This suggests that they are created during coalescence of the layer. It would also explain why there are only a few prismatic SFs in the 10 nm thick layer. The 10 nm layer exhibits only a few interconnected islands as the coalescence is just starting. On the other hand, it would not explain why there are almost no prismatic SFs in 100 nm thick layer. There would need to be some mechanism for annihilation of these prismatic SFs nucleated during the coalescence.

Ruterana et al. [39] observed folding of a basal SF back and forth between the basal and prismatic plane. The fault on the basal plane was bounded by a complex Frank partial with $1/6\langle 20\bar{2}3 \rangle$ Burgers vectors. The prismatic SF is bounded by $1/2\langle 10\bar{1}1 \rangle$ Burgers vectors, which means that there should be a stair rod dislocation at the intersection of the basal and prismatic planes. This could be described by the dislocation reaction $1/2[10\bar{1}1] \rightarrow 1/6[20\bar{2}3] + 1/6[10\bar{1}0]$. It is reasonable to assume that prismatic SFs could be nucleated from basal SFs bounded by a complex Frank partial.

However, nucleation of prismatic SFs during the coalescence seems to be a more probable mechanism of their formation due to their localization to the holes in the partially coalesced layer.

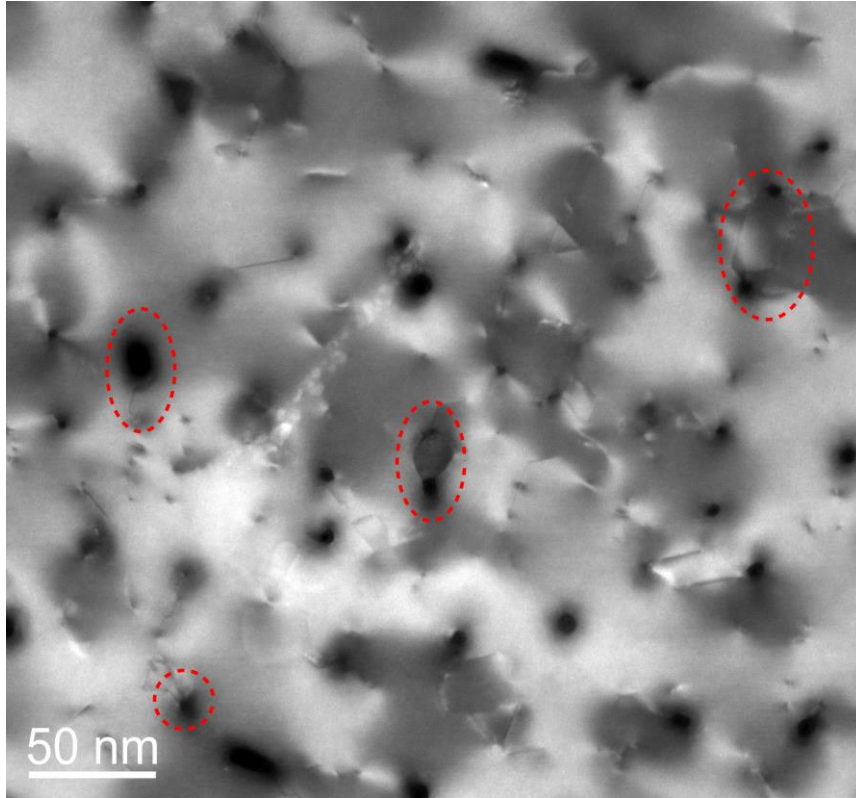


Figure 5.6: Plan view STEM image of 30 nm AlN layer with prismatic SFs visible near the holes in the partially coalesced layer. Image was taken near the $[0001]$ zone axis using $\mathbf{g} = 2\bar{1}\bar{1}0$. Some of the SFs located near the holes in the partially coalesced layer are highlighted by red ovals.

Strain relief in AlN/Si (111)

Misfit dislocations are dislocations present at or near the interface between two materials with different lattice parameters, where they are able to accommodate the lattice misfit strain. They have dislocation line vector parallel to the interface and need to have an edge component of their Burgers vector parallel to the interface. In AlN, perfect misfit dislocations can have $1/3\langle 11\bar{2}0 \rangle$ or $1/3\langle 11\bar{2}3 \rangle$ Burgers vector, because only those have nonzero component parallel to the interface.

Misfit dislocations are generated in the layer, when the layer exceeds the critical thickness (or critical size of islands), where it becomes beneficial to nucleate misfit dislocations instead of having the layer elastically strained [58–60]. Therefore, as the size of the islands increases, the stored elastic strain energy increases toward the critical point at which misfit dislocations are nucleated. Additional misfit dislocations could then be nucleated during the coalescence phase. Islands could no longer reduce their strain by elastically expanding to their surroundings, but instead they coalesce with neighboring islands possibly leaving the misfit dislocation at the coalescence boundary [61,62].

The lattice mismatch of AlN/Si (111) is 19%, which means that there is approx. 5/4 ratio between lattice planes in AlN and Si [36]. Therefore, there should be a misfit dislocation every

5 lattice spacings in AlN. Using this simple prediction, misfit dislocations should be present in high densities and be observable in plan view and cross-sectional samples.

Figure 5.7 shows the AlN/Si (111) interface with highlighted misfit dislocation present at the interface. However, misfit dislocations are not observed every 5 lattice spacings as predicted from the lattice mismatch, which suggests that only some part of misfit strain is relieved by these dislocations. Misfit dislocations also appear only in areas without the amorphous layer, which constitute only a fraction of the interface. If the amorphous layer is present at the interface, misfit dislocations are not observed. Misfit dislocations could therefore provide only a partial relief of the misfit strain and other possibilities should be considered.

Misfit dislocations were only observed in the cross-sectional images but not in the plan view images shown in Figure 5.4 using diffraction contrast. This could be explained by the differences of crystal structures of AlN and Si. Misfit dislocations are normally observed using diffraction contrast in heterostructures composed of layers that have the same crystal structure. As the crystal structure is continuous across the interface, the strain field caused by the misfit dislocation can be imaged by diffraction contrast. However, the crystal structures of AlN (hexagonal wurtzite) and Si (cubic diamond) are different and if the misfit dislocation is located at the interface, it cannot be detected using diffraction contrast. In the classical example of dislocations in gold foil, the dislocations are visible using diffraction contrast if located at least one atomic plane away from the foil surface [63]. Using this argument, we can assume that the misfit dislocation would be invisible if located exactly at the heterointerface. It needs to be at least one atomic plane away from the interface to be observable by diffraction contrast in the plan view images.

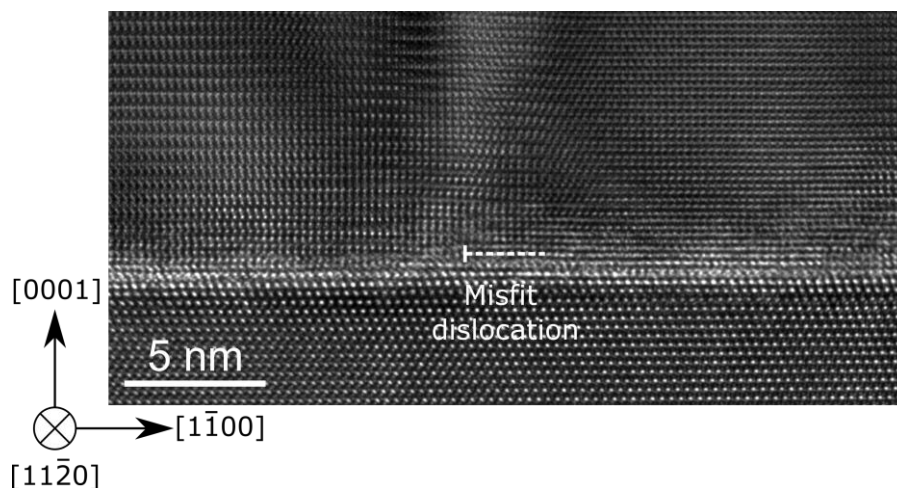


Figure 5.7: High-resolution TEM image of an interface between AlN and Si exhibiting a misfit dislocation at the interface.

We propose that the next factor influencing the strain relief is the amorphous interfacial layer, which was discussed in detail in the previous section. As there is no sharp transition from Si to AlN, but the transition is more gradual due to the amorphous layer, the misfit strain is not

fully contained in the AlN layer, but some of its part is accommodated by the amorphous layer. Therefore, the AlN film is not as strained as it would be when connected directly to the Si substrate. The accommodation of misfit strain by the amorphous layer leads to reduction of the density of misfit dislocations. The amorphous layer may play an important role in accommodation of lattice mismatch in AlN/Si heterostructures, where this layer is often observed.

Threading dislocations

Threading dislocations in this section were studied in NLs of AlN/Si (111) and in GaN layers grown on the AlN NL on Si (111) by MOCVD. TEM was employed in order to study the distributions and types of TDs and to discuss their origin.

Three types of TDs are expected to form in the wurtzite structure: (i) the *a*-type dislocations with Burgers vectors $1/3\langle 11\bar{2}0 \rangle$, (ii) the *c*-type dislocations with Burgers vectors $\langle 0001 \rangle$, and (iii) the *a+c*-type dislocations with Burgers vectors $1/3\langle 11\bar{2}3 \rangle$. Depending on the relative orientation of the dislocation line and the Burgers vector, these dislocations can have pure edge, pure screw or mixed character. The Burgers vector is deduced using the standard $\mathbf{g}\cdot\mathbf{b}$ visibility criterion in TEM, where \mathbf{g} is the diffraction vector, and \mathbf{b} the Burgers vector of the dislocation. In cross-sectional samples with $\langle 10\bar{1}0 \rangle$ orientation, the dislocations with the *a*-component, i.e. the *a*-type and *a+c*-type dislocations, are visible when using, for example, $\mathbf{g} = 1\bar{2}10$, whereas the pure *c*-type dislocations are invisible under this diffraction condition. On the other hand, both *c*-type and *a+c*-type dislocations are visible when using $\mathbf{g} = 0002$, which makes the *a*-type dislocations invisible. The only dislocations that are visible under both diffraction conditions are of the *a+c*-type. For the plan view samples with $\langle 0001 \rangle$ orientations, it is much harder to identify the types of dislocations present, because there is no available diffraction condition near the $\langle 0001 \rangle$ zone axis, where the *c*-type dislocations would be visible. In order to view the *c*-type dislocations, the sample needs to be tilted, for example, to the $\langle 2\bar{1}\bar{1}3 \rangle$ zone axis, where all types of dislocations could be visible. This was previously described by Datta et al. [64].

Many defects nucleate at the heterointerface between AlN and Si (111). Therefore, 30 nm and 100 nm thick AlN NL samples analyzed by AFM in section 5.1.1 were used to investigate TDs. Both cross-sectional and plan view samples were investigated to thoroughly study the structure of TDs in AlN. Plan view and cross-sectional STEM images of AlN NLs are shown in Figure 5.8 and Figure 5.9, respectively. In both types of images, TDs could be readily observed. From the cross-sectional images it is apparent that all types of TDs are present, including *a*-type, *c*-type, and *a+c*-type. In the plan view images, especially in the 30 nm sample, TDs terminated by V-defects are visible. Although, V-defects are also visible in the cross-sectional images, there are no TDs visible in the 10 nm sample (apparent from Figure 5.4(c) from the previous section). Prismatic SFs are visible in the plan view images, but they were discussed in more detail in the previous section.

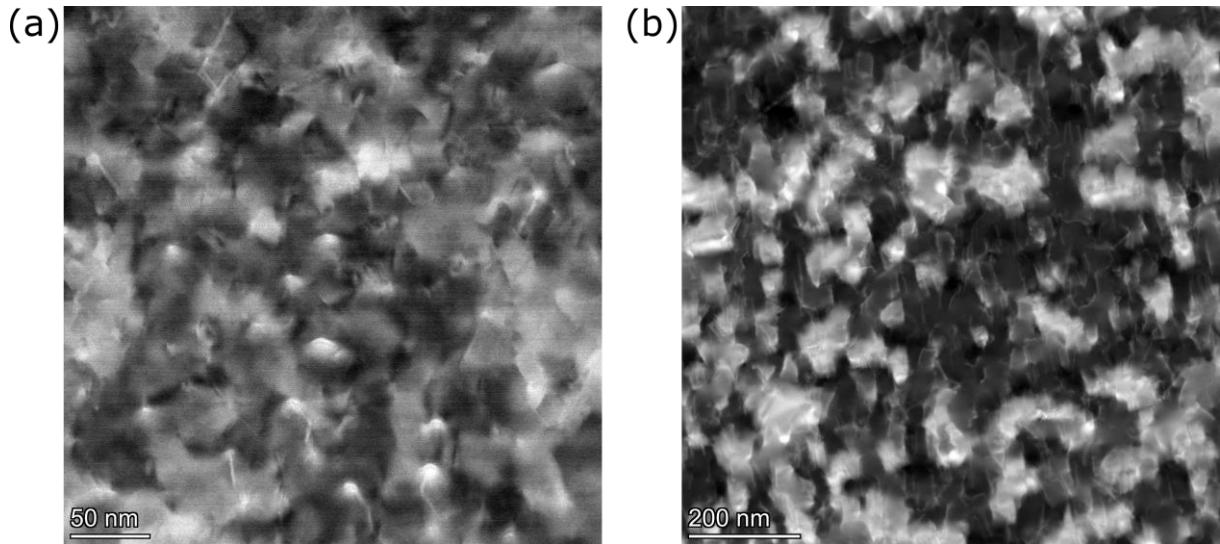


Figure 5.8: Plan view dark field images of AlN NLs with the thicknesses of 30 nm (a) and 100 nm (b). Both images were taken in the $[2\bar{1}\bar{1}]_3$ zone axis.

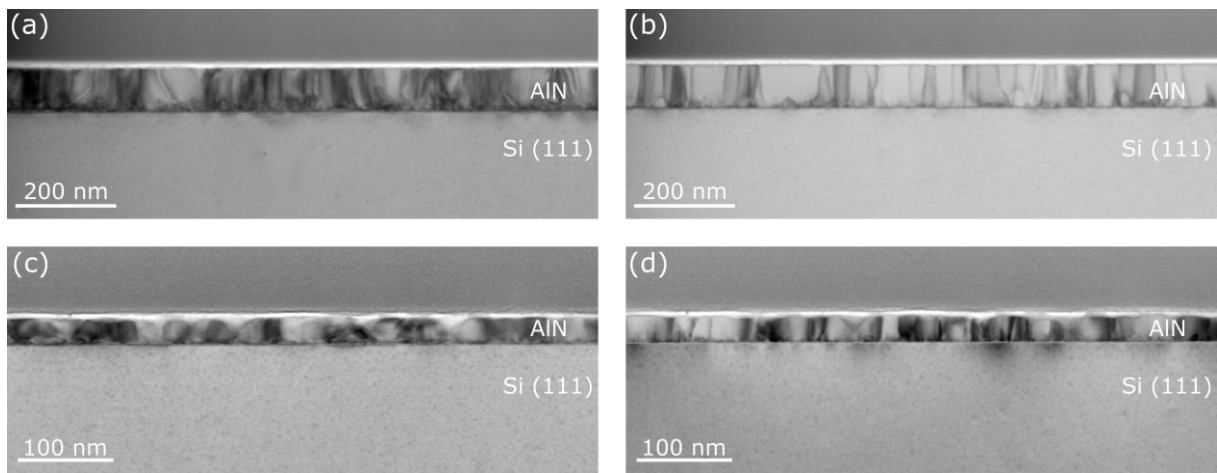


Figure 5.9: Bright field cross-sectional STEM images of 100 nm (a, b) and 30 nm (c, d) thick AlN NLs oriented near the $[10\bar{1}0]$ zone axis using the diffraction condition: (a, c) $g = 1\bar{2}10$, (b, d) $g = 0002$.

The diffraction contrast analysis was done to distinguish between various dislocations present in the layers and their distribution. All three types of TDs are present in the GaN/AlN/Si (111) sample shown in Figure 5.10. Most of these are of the *a*-type (54.3%), fewer are of the *a+c*-type (38.6%), and the *c*-type dislocations are quite rare (7.1%). Most of these TDs are not aligned perfectly with the $\langle 0001 \rangle$ growth direction, which makes it difficult to determine their exact characters (edge, mixed or screw). Nevertheless, our observations agree qualitatively with the work of Naresh-Kumar, et al. [4], who determined that 60% of the TDs are edge, more than 38% mixed, and less than 2% screw. The AlN layer consists of columnar crystals that are visible

in Figure 5.10(a) as alternating darker and brighter areas. However, they are not visible under $g = 0002$ in Figure 5.10(b), which means that these crystals are slightly rotated around the c axis (vertical in both images).

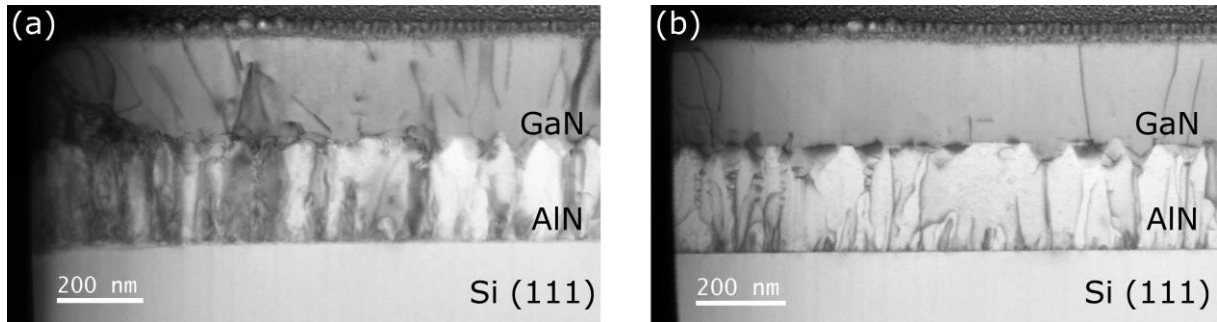


Figure 5.10: Bright field STEM images of the same area of the GaN/AlN/Si (111) sample oriented near the $[10\bar{1}0]$ zone axis using the diffraction condition: (a) $g = 1\bar{2}10$, (b) $g = 0002$.

Judging from the line energies taken from the linear elasticity [27], it could be deduced that most of the TDs would be of edge type, followed by the screw and mixed dislocations. Using these simple predictions to compare with the dislocation densities in this work, the edge dislocations appear with the highest density, but the density of screw and mixed dislocations does not correspond to theoretical predictions. Holec [21] showed that the mixed TD is the most stable if oriented in the $[0001]$ direction, but there are also other orientations with deep local minima.

One possible explanation for this discrepancy is that the threading screw dislocations have stronger tendency to form elongated half-loops than mixed dislocations. Screw dislocations could be spread on the three $\{\bar{1}100\}$ prismatic planes due to the underlying three-fold symmetry of the $[0001]$ axis. Opposite screw dislocations could then undergo a cross-slip between these planes during the growth and annihilate while creating half-loops. Since cross-slip of mixed dislocations is not possible, they would have to be on the same plane to annihilate, which is much less probable.

The next possible explanation of higher density of mixed dislocations is that they are multiplied by dissociation. A mixed dislocation in the $[0001]$ direction could be dissociated into two dislocations bounded by a SF. Two possible options were confirmed experimentally. Arslan et al. [10] observed dissociation of a mixed dislocation into edge and screw dislocations with SF on the $(1\bar{1}00)$ plane by aberration corrected STEM. This dissociation does not provide any energy savings, thus it was assumed it was defect driven. According to this reaction the density of both edge and screw dislocations would increase at the expense of mixed dislocations. From our STEM analysis, this does not seem to be the case, because we observed low density of screw dislocations, in disagreement with the prediction above.

Another possible mechanism was proposed by Hirsch et al. [65]. They showed that edge dislocations in GaN could dissociate by climb according to the reaction $a \rightarrow (a/2) + (a/2)$ while

creating a SF on the (0001) plane. Similarly, dissociations of mixed dislocations follow the equation $(a+c) \rightarrow (a+c)/2 + (a+c)/2$ while creating a SF that results from an intersection of SFs on the (0001) and (11 $\bar{2}$ 0) planes. The resulting $1/6[11\bar{2}3]$ fault was further studied in AlN [66] and, more recently, in GaN [65]. In both materials, the SF had a zincblende structure, which is metastable, and its energy is slightly higher than wurtzite. Using the dissociation model of Hirsch et al. [65] the occurrence of individual types of TDs might change. The most probable would be edge dislocations followed by $(a+c)/2$ partial mixed dislocations and the least probable would be screw dislocations. This is in agreement with the experimental TEM data. This model would also imply that there are SFs present in between the partial dislocations which were, however, not observed.

The origin of TDs in III-nitrides grown on Si (111) has long evaded understanding of scientists. Majority of research was focused on the origin of TDs in III-nitrides grown on sapphire substrates, because sapphire was used as the main substrate for III-nitride based LEDs. There are several possible explanations for the origin of TDs in III-nitrides grown on sapphire.

Firstly, TDs could be nucleated during the island coalescence phase of the layer growth. TDs could accommodate the crystal lattice tilt at the sub-grain boundary of the mosaic structure that is created by island coalescence [67]. If the crystal lattice is tilted with respect to the other island along the [0001] axis, then the boundary will consist of pure edge TDs with $1/3(11\bar{2}0)$ Burgers vector. If the two islands are rotated along the $\langle 1\bar{1}00 \rangle$ axis, then the misorientation could accommodate the network of pure screw TDs with $\langle 0001 \rangle$ Burgers vector. If the relative lattice tilt is different from the two aforementioned tilts, then the boundary consists of a network of mixed dislocations [67]. This approach would explain all types of dislocations in III-nitride epilayers. Similar conclusion was drawn by Qian et al. [68] and Wu et al. [69]. However, later works of Oliver et al. [5,70], Narayanan et al. [71], and Moram et al. [72] question these conclusions. Their studies on partially coalesced layers show that only in some cases, there are arrays of TDs at the coalescence boundaries, but definitely not in every case. Also, TDs are already present inside the islands prior to the island coalescence. The dislocation arrays observed in the coalesced layers in the previous studies could be explained by the fact that the *a*-type TDs aligned in $\langle 11\bar{2}0 \rangle$ directions represent low energy configurations [73]. Therefore, if the TDs are mobile, they might have the tendency to align in one direction, which could appear as the position of a coalescence boundary. Considering the previously mentioned arguments, nucleating TDs from the coalescence of misaligned islands is one possible mechanism. However, other mechanisms should be considered as well because the former cannot reliably explain the origin of all TDs and it was questioned by several authors.

A similar mechanism purporting to explain the origin of TDs was proposed by Kwon et al. [74]. They assert that TDs could be created from misfit dislocations when individual islands coalesce, when the network of misfit dislocations is not identical in every island. When the two islands coalesce, the misfit dislocations from the two islands might not join each other. Since dislocations cannot terminate inside the material, the misaligned dislocations originating in the two islands have to bend toward the nearest surface. This changes their orientations and transforms them from misfit to TDs. If the islands are rotated along the *c* axis, the *a*-type TDs are necessary to accommodate this misorientation. Therefore, misfit dislocations, which are

also *a*-type, that transform into TDs upon the island coalescence are beneficial to accommodation of island misorientation. However, this mechanism can only explain the origin of the *a*-type TDs and a different mechanism should be considered for the *c*-type and the *a+c*-type dislocations.

The next mechanism to consider is the nucleation of TDs from the partial dislocations bounding SFs. III-nitrides often contain large concentrations of point defects that can diffuse and cluster together to create SFs bounded by Frank partial dislocation loops. Narayanan et al. [71,75] and Meng et al. [76] proposed that TDs could result from a dislocation reaction between partial dislocations bounding the SFs. Shockley and Frank partial dislocations could occur in III-nitride layers. From the reaction of two Shockley partial dislocations, it is possible to get an *a*-type dislocation using the reaction $1/3[10\bar{1}0] + 1/3[1\bar{1}00] \rightarrow 1/3[2\bar{1}\bar{1}0]$. It is also possible to get *c*-type dislocation from the reaction of two simple Frank partials $1/2[0001] + 1/2[0001] \rightarrow [0001]$ [71]. Additionally, *a+c*-type dislocation could result from dislocation reaction of two complex Frank partials, e.g. $1/6[20\bar{2}3] + 1/6[2\bar{2}03] \rightarrow 1/3[2\bar{1}\bar{1}3]$. Nucleation of *a+c*-type TD from two Frank partials was observed experimentally by Narayanan et al. [71]. By considering the reactions of partial dislocations bounding the SFs it is possible to explain all types of dislocations present in the III-nitrides layers. The question is if the SFs are present in III-nitrides in quantities sufficient for them to be able to react and create the high density of TDs observed in III-nitrides layers.

We have also observed TDs arising in the immediate vicinity of a misfit dislocation, as shown in Figure 5.11. This supports the contention that misfit dislocations can bend and transform into TDs. To further investigate nucleation of TDs, molecular statics simulations of GaN islands were performed using the Tersoff-Brenner potential developed by Nord et al. [32]. A single semi-spherical GaN island with the diameter of 10 nm was placed on GaN substrate. The atoms in both parts of the simulation cell were initially placed on the wurtzite lattice with equilibrium lattice parameter after which the whole system was expanded 20% in the two directions perpendicular to the interface. During the subsequent relaxation, the atoms in the substrate were held fixed but the atoms in the island were allowed to relax at zero absolute temperature and pressure. The resulting dislocation substructure was visualized using the Dislocation Extraction Algorithm implemented in Ovito [77] and shown in Figure 5.12. One clearly sees that the misfit strain is relieved by nucleating $1/3\langle 11\bar{2}0 \rangle$ misfit dislocations at the interface between the strained island and the substrate. Most of these dislocations arrange into a hexagonal network. However, the dislocations closer to the surface of the island bend away from the interface and have a tendency to align themselves in the direction perpendicular to the surface of the island. We anticipate that further growth can promote the reorientation of dislocation lines into the direction perpendicular to the surface and thus to transformations into TDs when dislocation networks in two islands do not perfectly align with each other.

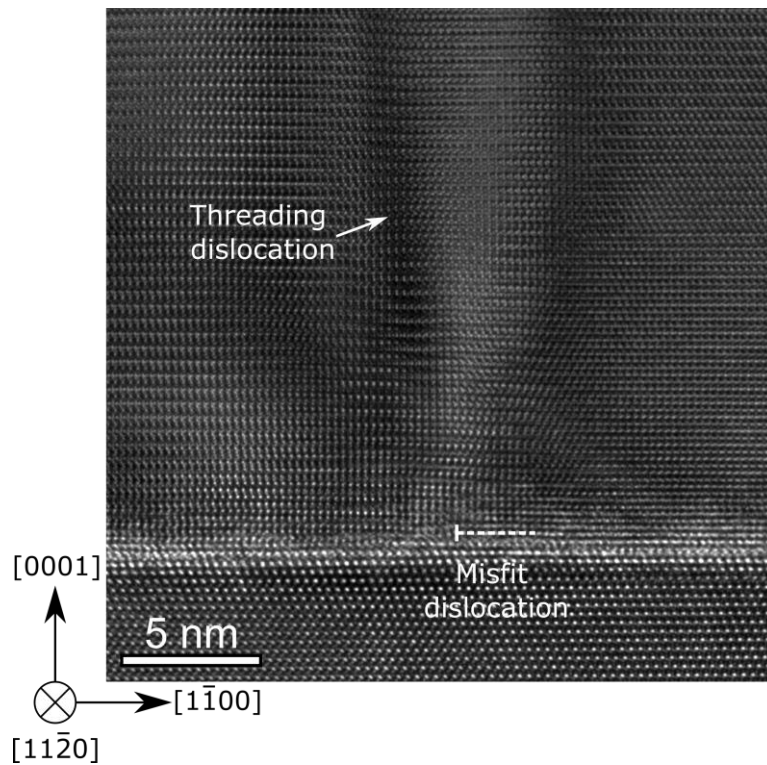


Figure 5.11: High-resolution TEM image of the interface between AlN and Si that exhibits TD arising in the vicinity of a misfit dislocation at the interface. The TD is visible due to the residual diffraction contrast in the high-resolution image.

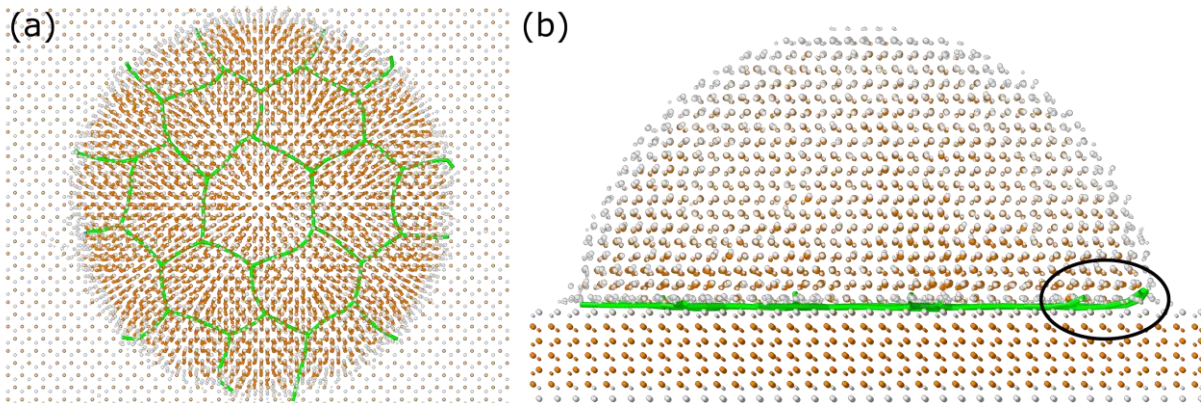


Figure 5.12: Simulated GaN island viewed in the [0001] direction (a) and in the [11̄20] direction (b). The colors of atoms represent the local neighborhood of every atom (orange=wurtzite, gray=unspecified/surface). All misfit dislocations (green lines) have $1/3\langle 11\bar{2}0 \rangle$ Burgers vectors. The misfit dislocations that bend away from the interface are highlighted by the black oval.

Out of the possible mechanisms described above, we believe the following two are the most probable. The first one is the bending of misfit dislocations toward the island surface, which results in creating TDs after the island coalescence. The second mechanism is the nucleation of TDs from partials bounding the SFs. These mechanisms can reasonably explain all types of TDs present in III-nitrides. It is also important to mention that there are important differences between III-nitride layers grown on sapphire and Si. One of the most important is the amorphous layer often present at the AlN/Si (111) interface. The amorphous layer could significantly affect the nucleation mechanism of TDs because the growing layer does not have direct contact with the substrate. However, its impact is not fully understood. We suggest that theoretical models aiming to explain the origin of TDs in AlN/Si (111) layers should take into account the impact of amorphous interfacial layer.

5.1.3 Electrical activity of extended defects in AlN layers

The presence of extended defects in AlN layers determines the electrical activity of the device. These defects may also induce non-radiative recombination, which is undesirable, because it reduces the efficiency of the device.

The electrical activity of defects can be measured by electron beam induced current (EBIC). The basic principle of EBIC is that the sample is irradiated by high energy electrons, which are able to excite electrons in the sample from the valence into the conduction band, thereby creating the electron-hole pairs. These pairs are then separated by the internal electric field (caused by p-n or Schottky junction) and measured by the external ammeter. The contrast comes from the difference between the number of generated electron-hole pairs and the number of recombined electron-hole pairs. The presence of these defects usually leads to an increased recombination rate and thus drops in the induced current. The positions, where the current drops are associated with the positions of extended defects.

The AlN layers in chapter 5.1.3 were grown on Si (111) by MOCVD at 1000 °C. More information about the growth can be found in ref. [78].

Identification of defects in AlN layers

The surface of AlN layers was analyzed by AFM to investigate the surface termination of extended defects present in the layers. The topography images are shown in Figure 5.13. Figure 5.13(a) is a 5.5×5.5 μm image of AlN surface taken by conventional tapping mode and shows several types of surface depressions. The first type were an individual surface depressions (marked as A), which are mostly uniformly distributed across the surface. Figure 5.13(b) shows these depressions in more detail revealing the hexagonal shape, which is typical for the V-defects in III-nitrides. They might originate at dislocations [79], nanopipes [80], stacking mismatch boundaries [81], and inversion domains [82]. Their density was analyzed to be able to directly compare it with the defect density obtained from other techniques. The density of V-defects was $\rho_A = (1.3 \pm 0.1) \times 10^9 \text{ cm}^{-2}$; it was analyzed from multiple areas randomly chosen on the surface and standard error was used for the error bars. The second type of defects present on the AlN surface were clusters of surface depressions (denoted as B) imaged in detail

in Figure 5.13(c). Upon further examination the cluster consisted of individual V-defects. The density of these clusters was $\rho_B = (2.4 \pm 0.4) \times 10^7 \text{ cm}^{-2}$, which was two orders of magnitude lower than the density of V-defects. A more detailed topography scan shown in Figure 5.13(b) revealed another type of defects (marked as C), which were described as very small surface depressions equally distributed on the AlN surface in between larger V-defects. The density of C-type defects was calculated to be $\rho_C = (4.6 \pm 0.1) \times 10^{10} \text{ cm}^{-2}$. Their density was by far the highest of all surface defects found on the AlN surface.

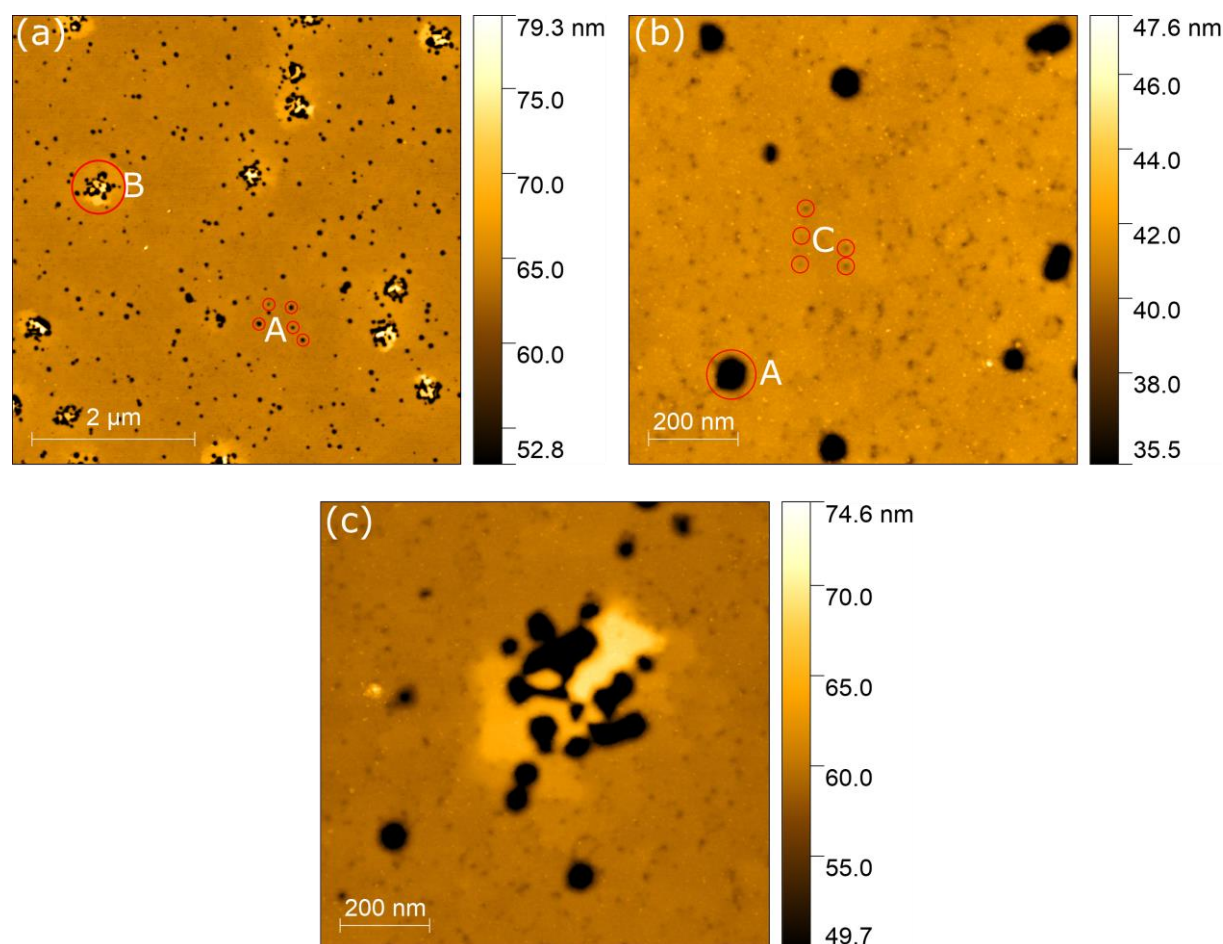


Figure 5.13: (a) AFM topography of the $5.5 \times 5.5 \mu\text{m}$ AlN surface area revealing the V-defects (denoted as A) and clusters of V-defects (denoted as B), (b) $1 \times 1 \mu\text{m}$ image of area between V-defects showing another type of defects identified as surface terminations of TDs (denoted as C) and (c) $1 \times 1 \mu\text{m}$ image of the cluster of V-defects.

To further analyze the defects identified by AFM, STEM dark field imaging was used. STEM is able to visualize the crystallographic defects present in the layers and to identify the source of the various types of surface depressions. The STEM cross-sectional images of AlN/Si (111) FIB lamella are shown in Figure 5.14. Two diffraction conditions were used to determine the Burgers vector of dislocations present in the sample. The $g = 0002$ diffraction

condition reveals the presence of dislocations that have finite components of their Burgers vectors in the c -direction. If the dislocation is visible only in this diffraction condition, it is identified as being of c -type with the $\langle 0001 \rangle$ Burgers vector. When using the $\mathbf{g} = 1\bar{2}10$ diffraction condition, only the dislocations with Burgers vector having the a -component are visible. If the dislocation is visible only in this diffraction condition, then it is a -type with the $1/3\langle 11\bar{2}0 \rangle$ Burgers vector. If the dislocation is visible using both $\mathbf{g} = 0002$ and $\mathbf{g} = 11\bar{2}0$ diffraction conditions, then it is $a+c$ -type with the $1/3\langle 11\bar{2}3 \rangle$ Burgers vector. We have observed that most TDs had their dislocation line direction close to $[0001]$. Therefore, a -type, c -type and $a+c$ -type TDs will be referred to in the following as edge, screw, and mixed, respectively.

The dislocation density was measured by counting the total length of TDs (i.e. only the ones emanating on the surface) and dividing it by the volume of the lamella, which was measured in SEM. This was done for each dislocation type across the entire lamella (approx. 7740×220 nm area with the lamella thickness of 100 nm). The total dislocation density was 2.5×10^{10} cm⁻². The density of edge dislocations was 1.5×10^{10} cm⁻² (61% of the total density), the density of screw dislocations was 2.1×10^9 cm⁻² (8% of the total density), and the density of mixed dislocations was 7.8×10^9 cm⁻² (31% of the total density). For two reasons, these densities should be taken as lower bounds. Firstly, there is always some amorphous layer on the surface of the lamella that is caused by the FIB milling. Secondly, when the dislocation is too close to the surface, image forces acting on the dislocation may be high enough to attract it to the surface. These phenomena effectively reduce the volume available for the dislocations and, consequently, increase the dislocation density. Due to the similarity of the density of C-type surface depressions (4.6×10^{10} cm⁻²) and the total density of TDs (2.5×10^{10} cm⁻²), the C-type surface depressions were associated with surface terminations of TDs. However, not all TDs have to terminate by creating surface depressions. Dislocation etch pits studies made by Hino et al. [6] showed that edge dislocations have very shallow etch pits. This suggests that their surface depressions are very shallow and may not be recognized by AFM.

In Figure 5.14(c) and (d) the V-defects with the typical “V” shaped surface depressions are clearly visible. The observation of V-defects in STEM provided further support that the A-type surface depressions identified in the AFM images are indeed V-defects. The V-defect is always associated with dislocations having the screw component, as visible from Figure 5.14(c), and only sometimes with dislocations with having the edge component (Figure 5.14(d)). Therefore, V-defects were associated with screw and mixed dislocations, which agrees with previous observations of GaN/Si layers [79,83,84].

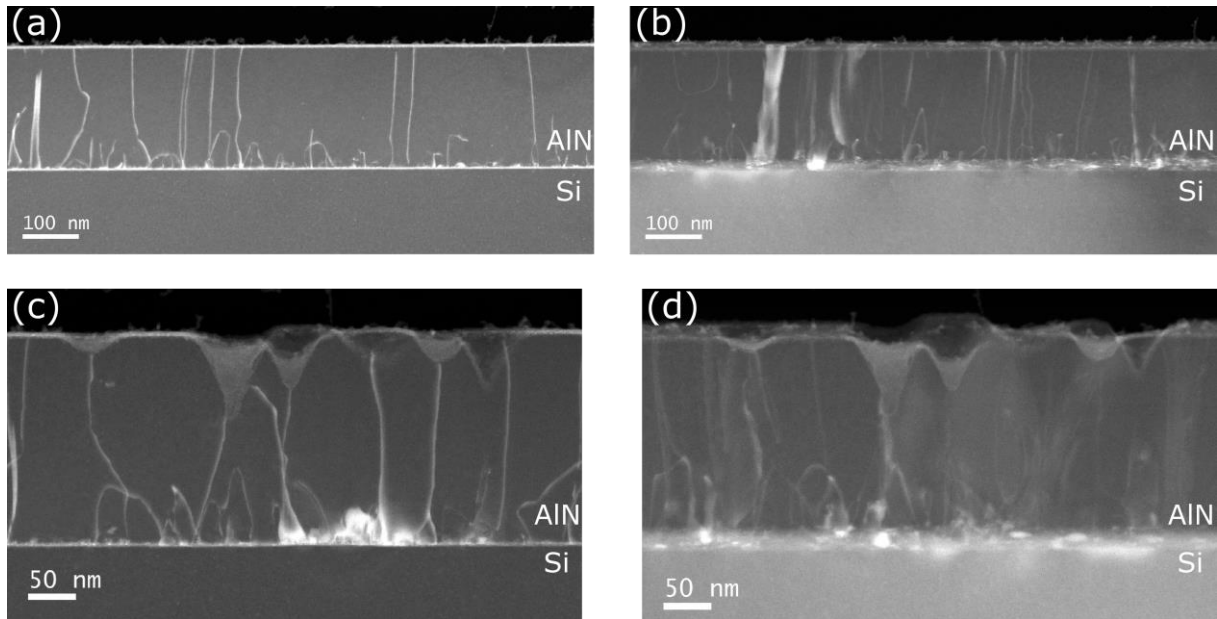


Figure 5.14: STEM dark field images of AlN/Si layers showing TDs and V-defects, taken using the diffraction condition $g = 0002$ (a), (c), and using $g = 1\bar{2}10$ (b), (d) near the $[10\bar{1}0]$ zone axis.

Electrical activity of extended defects in AlN layers

The electrical activity of extended defects was assessed using EBIC. Prior to the measurement, 3 nm Ni and 3 nm Au layers had to be deposited to create the Schottky junction on the sample surface. This junction creates the internal electric field inside the sample, which separates the bound electron-hole pairs generated by the electron beam. Beam energy of 5 kV and 440 pA beam current was used for the measurement. The images using signals from secondary electrons and EBIC are shown in Figure 5.15 (a) and (b), respectively. In the secondary electron image, many evenly distributed, and some clustered surface depressions are visible. These are analogous to the surface depressions observed by AFM and are marked the same way as in Figure 5.13. The EBIC image shows spatial variations of the current induced by the electron beam. It exhibits distinct drops in the induced current at the positions of the B-type surface depressions. The smaller A-type defects cause much smaller drops of induced current than the clusters of V-defects (B-type). The individual dislocations are barely noticeable in the secondary electron image and are associated with the small drops of induced current.

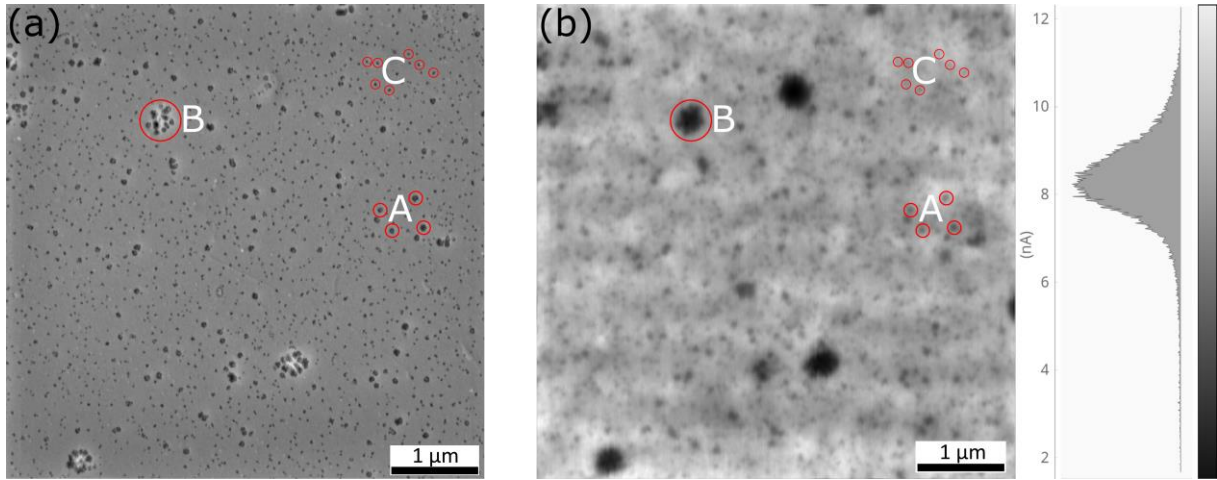


Figure 5.15: The secondary electron image of AlN surface (a), and EBIC image of the same area with periodic noise removed by Fourier transform in combination with a low-pass filter. The positions of defects are highlighted in red.

In order to further analyze the impact of defect types on the electrical properties of the AlN layers, we have analyzed the defect contrast, size and distribution of defects. The positions of defects were found by searching for the pixels in the EBIC image that had lower values (i.e. darker) than the defect-free areas (i.e. bright areas). The center of the defect was found by taking the lowest pixel value in the image and then the circular region was attached and expanded until the EBIC signal profile inside the circle ceased to be convex. This area was excluded from the image and this procedure was repeated until the pixel value reached the value of the defect-free surface. Using this method, we found 1134 defects in the $5.52 \times 5.48 \mu\text{m}$ area, which corresponds to the density of extended defects of $3.7 \times 10^9 \text{ cm}^{-2}$. Each defect was described by its diameter (i.e. the diameter of the circle representing the convex EBIC region centered at the defect) and the EBIC contrast, which was used as a measure of the defect recombination efficiency. The EBIC contrast was defined as $C_{max} = 1 - I/I_0$, where I_0 is the maximum current from the defect area, and I is the minimum current in the defect area corresponding to the center of the defect.

The results of the previously described analysis are shown in Figure 5.16. The histogram of the defect diameters in Figure 5.16(a) shows that most defects had diameters in the range of 70-80 nm. Only a few defects had radii below 70 nm, but there were many defects with radii larger than 80 nm. The defects with smaller diameters could be attributed to TDs, whereas the defects with large diameters to V-defects and their clusters. The histogram of EBIC contrast is shown in Figure 5.16(b). For a majority of defects, this contrast was around $C_{max} = 0.15$, but there are also many defects with higher defect contrast.

From the bivariate histogram in Figure 5.16(c) it is apparent that there is a linear dependence of the EBIC contrast on the defect diameter. This implies that defects with high recombination efficiency can attract charge carriers from larger area around them and thus have a larger imprint in the EBIC signal. The clusters of V-defects are the most efficient defect types present in our AlN layers and have the largest defect diameter, which results from the collective

effect of individual defects. The isolated V-defects were also very strong recombination centers. Combined with their higher density than clusters, the isolated V-defects significantly impair the electrical properties of the layers. Individual TDs had lower recombination efficiencies, but much higher densities than the V-defects and their clusters combined.

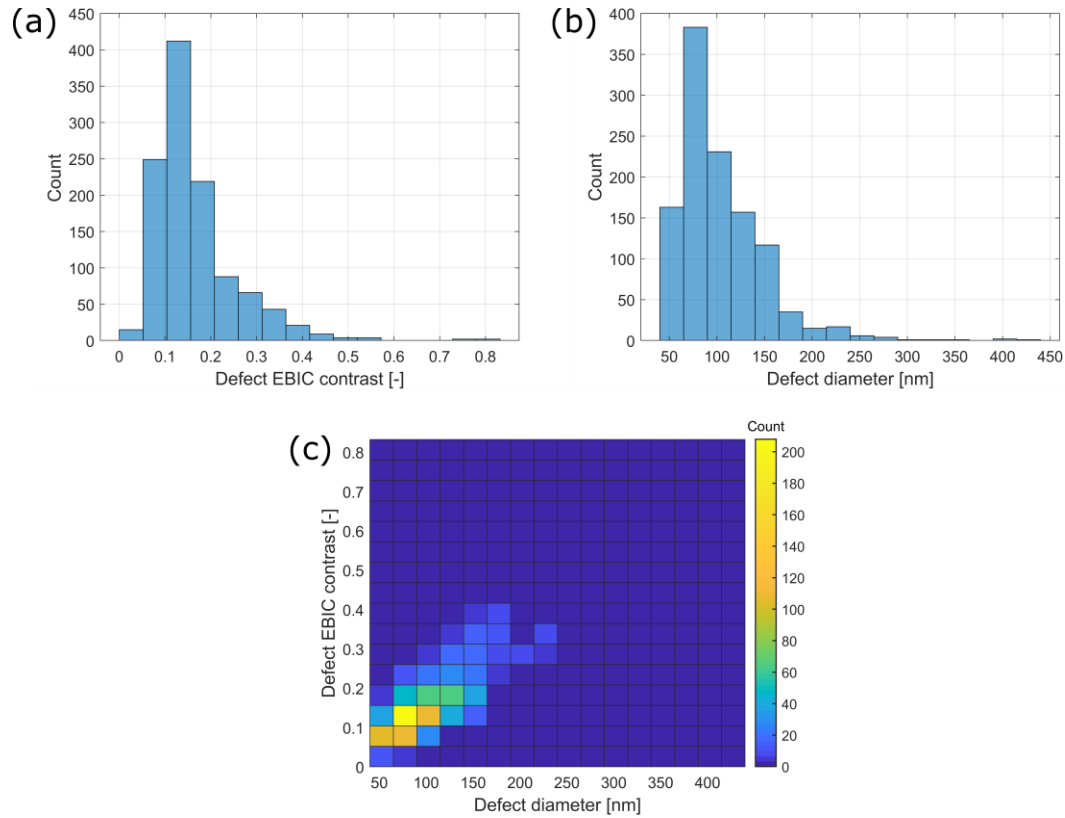


Figure 5.16: The histogram of the defect diameters (a), the defect contrast (b), and bivariate histogram of the defect contrast and the defect diameter (c), which shows their linear correlation.

Table 1 shows a comparison of the defect densities estimated by AFM, TEM and the defect contrast measured by EBIC. Among the individual defect types, the defect contrast varies by an order of magnitude, but the defect densities differ by more than three orders of magnitude. Although TDs have weak recombination strengths, they are distributed uniformly across the layer with very high density. V-defects and their clusters have high recombination strengths, but they have low densities and are distributed only locally. Because TDs are present almost everywhere in the layer, they are the major factor in determining the properties of the AlN layers. All of the studied defects deteriorate the electrical properties of the layers and should be eliminated, or their density reduced to ensure efficient operation of devices utilizing these AlN layers.

Table 1: The comparison of defect densities and defect contrasts obtained by AFM, TEM, and EBIC.

	Defect type	Density AFM [cm ⁻²]	Density TEM [cm ⁻²]	C_{max}
A	V-defect	$(1.3\pm 0.1)\times 10^9$	-	0.3-0.4
B	Cluster	$(2.4\pm 0.4)\times 10^7$	-	0.4-0.8
C	Threading dislocations	$(4.6\pm 0.1)\times 10^{10}$	2.5×10^{10}	0.05-0.3
	<i>a</i> -type (edge)		1.5×10^{10} (61%)	
	<i>a+c</i> -type (mixed)		7.8×10^9 (31%)	
	<i>c</i> -type (screw)		2.1×10^9 (8%)	

Using a combination of AFM, TEM, and SEM, we have shown that AlN/Si layers contain a large density of extended defects that impair the electrical properties of the layers. As the extended defects emerge on the surface, they create three types of surface depressions. Individual TDs have the smallest surface depressions and appear with the highest density. V-defects caused larger surface depressions, but their density was lower than that of TDs. The clusters of V-defects had the largest EBIC signal, but they appeared with the lowest density. All V-defects were associated with TDs having a finite screw component of their Burgers vectors. The STEM analysis showed that most of the TDs were edge (61%), followed by mixed (31%), and screw (8%) dislocations.

The EBIC measurements revealed large variations of induced current across the AlN surface. Individual TDs exhibited weak drops of induced current and were found to be uniformly distributed with high density. The V-defects acted as strong recombination sites, and this recombination efficiency was further enhanced for the clusters of V-defects. However, V-defects had low density and only local impact on the electrical properties. We assumed that individual TDs had the most significant impact on the properties of the AlN layer due to their much higher density and uniform distribution.

5.1.4 Correlative probe and electron microscopy

The correlative probe and electron microscopy (CPEM) is a novel technique that can take advantage of simultaneously acquiring signals from atomic force microscopy and scanning electron microscopy. It is advantageous over the other correlation techniques because the signals are measured at the same time using the same stage, which neglects the possible influence of different measuring conditions on the results. Here we describe the results of CPEM technique used in combination with EBIC on AlN and GaN layers, which we developed in collaboration with the NenoVision company.

The CPEM technique was utilized within the LiteScope SPM module (NenoVision), which was installed in the scanning electron microscope (Tescan Lyra 3 XMH/FEG in our case). The sample was mounted on the LiteScope piezostage, which performs scanning. The AFM and electron probes are both stationary and were separated by few hundreds of nanometers to ensure that both probes do not interact with each other and their separation was constant during the measurement. The separation of probes causes the offset of the images

which is resolved by overlaying the images, bringing them into coincidence and cropping the edges. This allows for systematic correlation of the physical properties of surfaces with their topography.

The combination of AFM and EBIC is advantageous for measuring the surface topography and the presence of electrically active defects in the vicinity of surfaces of GaN and AlN layers. The electrical activity of GaN surfaces was investigated by measuring the EBIC signal using the Tescan EBIC detector. This requires a Schottky barrier (metal-semiconductor interface), which was created on the surface of the GaN film by depositing 5 nm thick Au layer. The ohmic contact was prepared on the opposite side of the sample (Si surface). The 7 keV electron beam incident on the sample creates a large density of electron-hole pairs that are separated by the internal electric field arising from the Schottky barrier. These are rapidly recombined at TDs, which leads to local drops of current measured in the external circuit. The large mean-free path of charge carriers allowed these measurements to be made next to the Au layer, which simultaneously avoids contamination of the AFM tip by Au. The obtained results are shown in Figure 5.17.

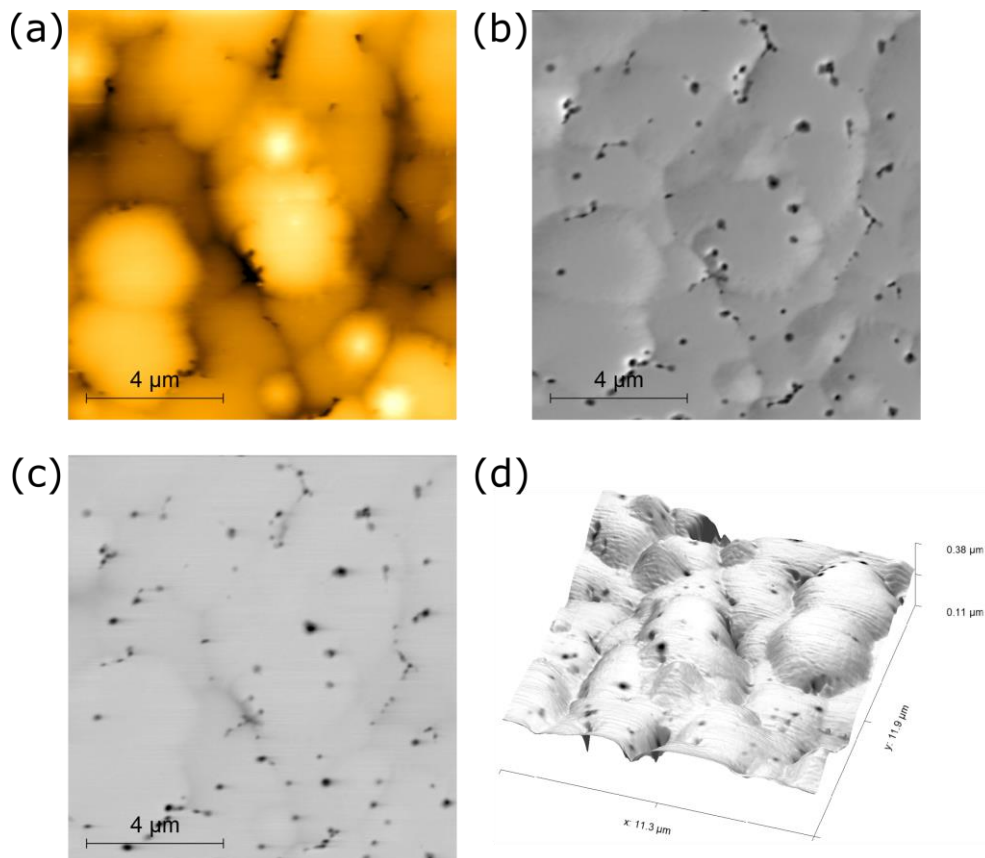


Figure 5.17: The surface of GaN/AlN/Si (111) represented using: (a) AFM as the topography map, (b) SEM using secondary electrons, (c) EBIC signal obtained by SEM, and (d) a 3D map with height taken from the topography in (a) and the coloring obtained from the EBIC signal in (c).

In Figure 5.17(a) and (b), one can see coalesced islands of GaN/AlN/Si (111) grown by MOCVD separated by depressions and holes, which could be associated with TDs emerging on the surface. The AFM signal is sensitive to topography and the secondary electron signal in SEM to near-surface features. Both images can be overlaid and cropped accurately to obtain complementary information that is not present in the individual signals. The EBIC signal shows local electrical activity in the layer determined by the electron interaction volume. The strongest contrast is associated with dark spots, where the EBIC signal drops significantly due to faster recombination of charge carriers. These spots are associated with TDs, dislocation clusters and/or nanopipes.

The electrical activity of defects in the AlN layer was investigated by CPEM. This time Mighty EBIC 2.0 from Ephemeron labs was used as an EBIC detector. Its higher sensitivity allowed us to measure very thin (200 nm) layers of AlN on Si (111). Beam energy of 5 kV was used for imaging, because according to our Monte Carlo simulation, majority of electrons interact within the AlN layer. As a Schottky contact, 3 nm Ni and 3 nm Au layer was deposited by magnetron sputtering and ohmic contact was fabricated from the back side of Si substrate. The surface topography from AFM in Figure 5.18(a) exhibits a flat surface with many surface depressions, some of which are clustered together. The signal from secondary electrons in Figure 5.18(b) is also able to resolve the same surface depressions as AFM but is lacking the depth information. The EBIC image in Figure 5.18(c) shows large areas of reduced current distributed unevenly across the surface. Small dots with lower current drops have much higher density and they are distributed evenly on the sample surface. Using CPEM, we were able to overlay the topography image with the EBIC signal (Figure 5.18(d)), which clearly shows that areas with large drops of current correspond to clusters of surface depressions. The individual surface depressions are also associated with the drops of induced current.

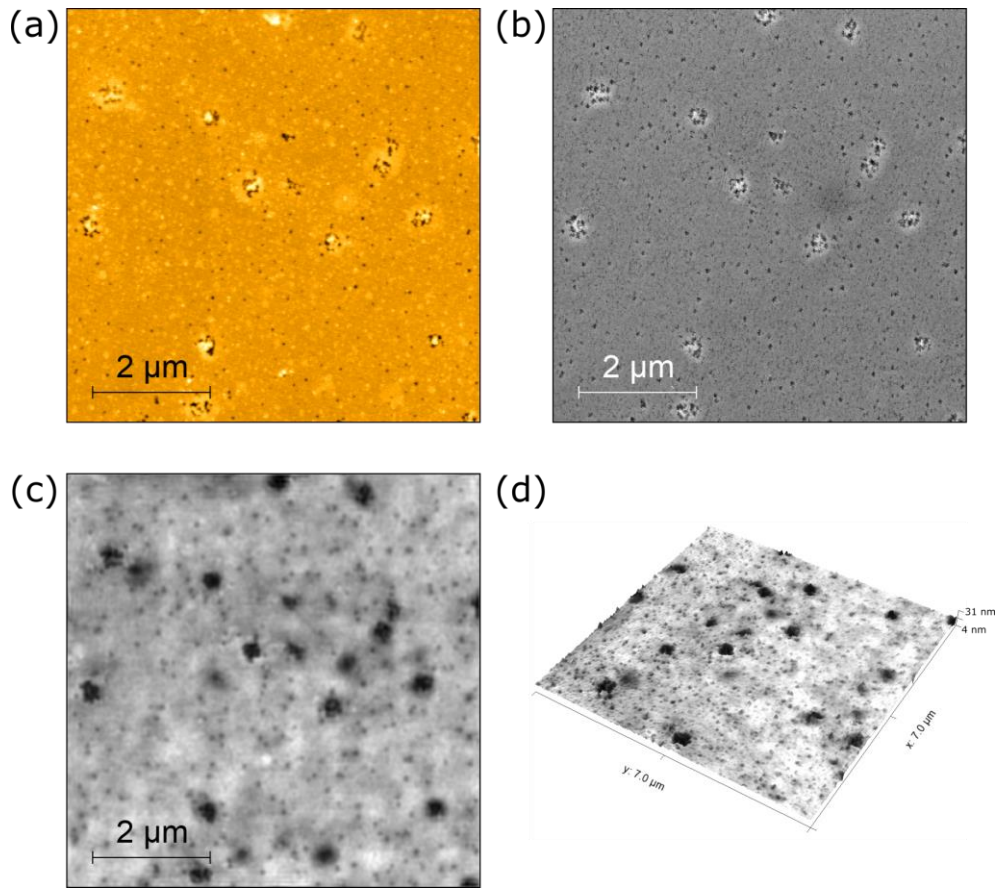


Figure 5.18: AFM topography image of AlN surface (a), the same area imaged with SEM using secondary electrons (b) and EBIC (c). AFM topography overlaid with EBIC image, acquired using CPEM (d).

5.2 Defects in zincblende GaN

Zincblende GaN (zb-GaN) layers exhibit various defects ranging from the growth defects to defects of the atomic structure. Growth defects were analyzed on the series of nucleation layer (NL) samples and defects of atomic structure were analyzed on the various samples including NLs and epilayers.

Samples were grown at approx. 600 °C by MOCVD on 3C-SiC templates grown on Si (001) with 2° or 4° miscut towards the [110] direction. These samples will be referred to as “as-grown”. In order to evaluate changes in the NL prior to the epilayer deposition, some samples were annealed, which consisted of a ramp from the growth temperature of the NL to the epilayer growth temperature (885 °C) and cooling. More details on growth conditions and annealing are available in ref. [85].

5.2.1 Defects in zincblende GaN nucleation layers

NLs were used to investigate the very beginning of the growth of zb-GaN. The thickness of the NL ranged from 3 to 44 nm. As the first step, AFM was used to study the morphology of the substrate for the growth of NL and the evolution of NL topography with increasing layer thickness before and after annealing. The second step involved the X-ray diffraction (XRD) studies of the strain and desorption of material during the annealing.

Substrate used for NL growth

The substrates used for the growth of NL were about 3 μm thick 3C-SiC templates grown on Si (001) substrates with 2° and 4° miscut towards the [110] in-plane direction. The high miscut is used to suppress the formation of antiphase domains in GaN layers as reported by Lee et al. [86]. The template was chemically-mechanically polished after the SiC growth. The AFM image of the substrate with 2° miscut in Figure 5.19 shows scratches from polishing, but the root-mean-square surface roughness is very low ($S_q = 0.4$ nm). There is one elongated surface defect (marked by the ellipse) that is perpendicular to the miscut direction and is much deeper than polishing scratches. Its orientation suggests that it is related to the crystallography of the substrate, but its origin is unknown.

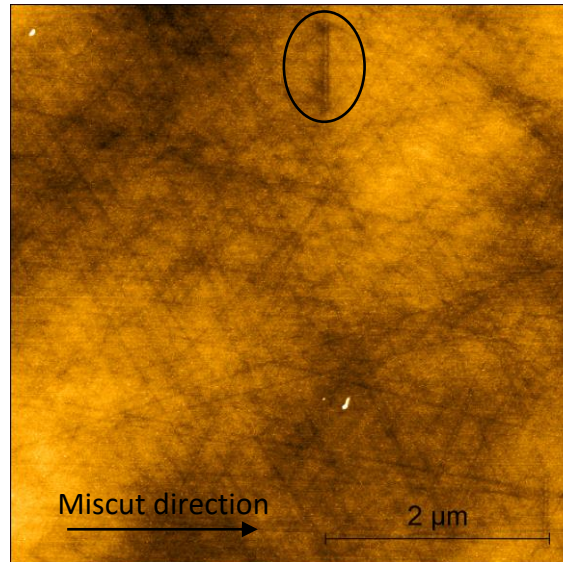


Figure 5.19: The AFM topography of 3C-SiC substrate with 2° miscut. The root-mean-square surface roughness $S_q = 0.4$ nm, and the range of heights (z -range) is 3.83 nm.

Topography of nucleation layers

AFM was used to compare the topography of as-grown and annealed samples with different thicknesses of NLs. The topography maps of as-grown samples are shown in Figure 5.20. The individual panels correspond to different thicknesses of the NL as marked at the bottom. The large-area topography maps in Figure 5.20(a) show elongated defects perpendicular to the direction of the miscut, which are present in all as-grown NL samples irrespective of their thicknesses. The sample with 3 nm NL exhibits randomly oriented elongated defects. The random orientations of these defects and the fact that they are not present in thicker NLs suggests that they are related to polishing scratches on the surface of the substrate. The finer polishing scratches are easily overgrown in thicker NLs. However, coarser substrate defects perpendicular to the miscut are more difficult to overgrow and remain visible in AFM images of the thickest NLs shown in the right panel of Figure 5.20(a).

One can see from the $1\ \mu\text{m}$ scans in Figure 5.20(b) that the NLs consist of small “island-like” features elongated in the direction perpendicular to the miscut. These features are present invariably in all samples and it suggests the three-dimensional Volmer-Weber growth mode [45]. This morphology was previously found in the zb-GaN epilayers and it was explained by the anisotropic diffusion along the $[110]$ and $[\bar{1}10]$ directions due to the potential valleys present on GaN surface [86]. This is probably also applicable to the NLs. The feature size perpendicular to the miscut was measured using the full width at half maximum of the power spectrum obtained from four $500\ \text{nm}$ AFM scans. The results of these measurements are shown in Figure 5.21. For the as-grown samples, the feature size increases with increasing thickness of the NL. The only exception at the thinnest NL is probably due to better separation of individual islands in the sample with 3 nm NL. The other samples have islands more coalesced, which leads to

smaller apparent feature sizes as compared to better separated islands. Feature size of zb-GaN NLs is also not dependent on the miscut of the substrate [85].

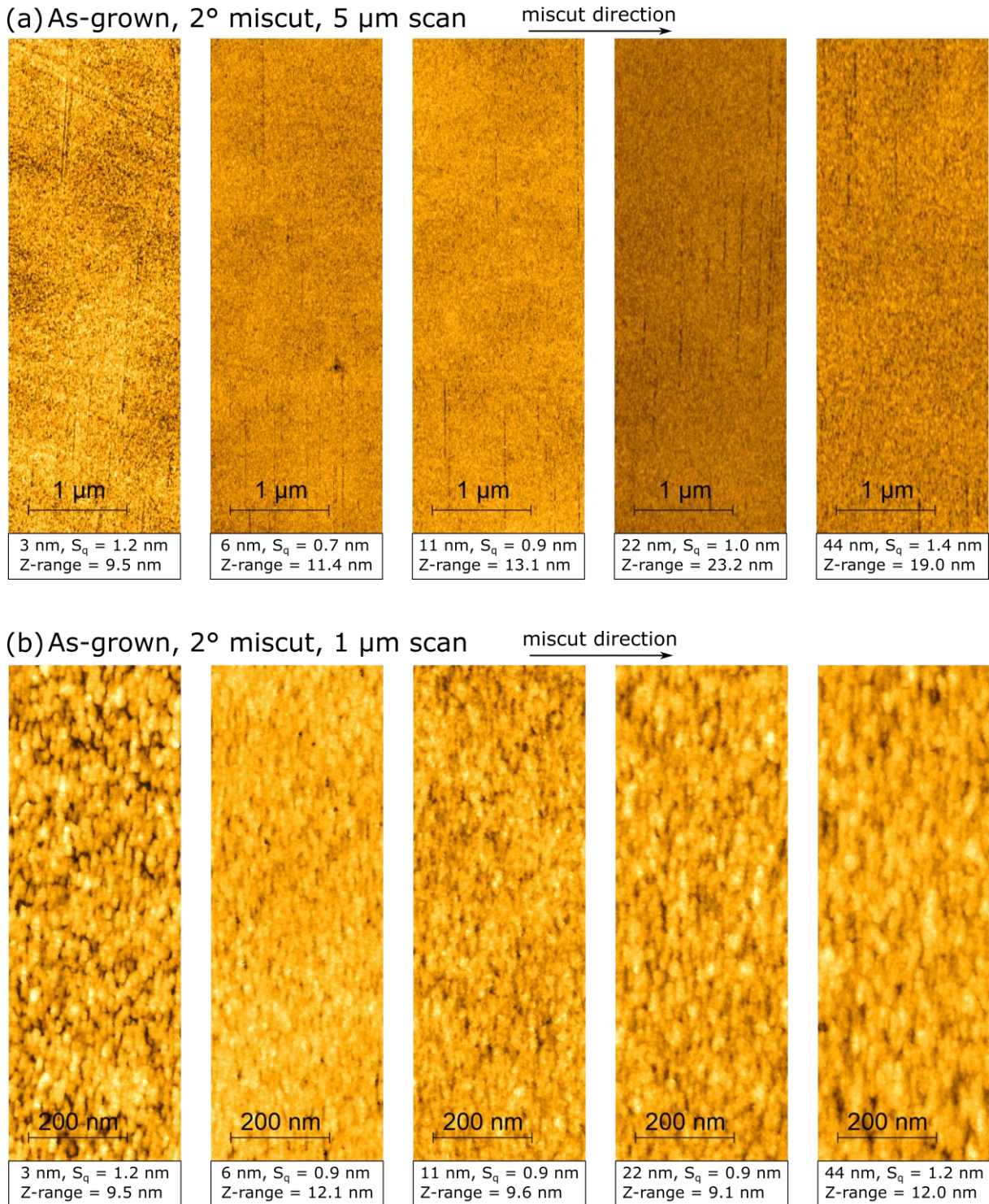


Figure 5.20: The AFM topography images of as-grown NLs with the same miscut direction in all images. The thicknesses of NLs, roughness (root-mean-square surface roughness S_q) and the z-range are indicated in the legend at the bottom of each image. The images in (a) are larger area scans with the vertical range of 5 μm, whereas those in (b) are higher resolution images with the vertical range of 1 μm.

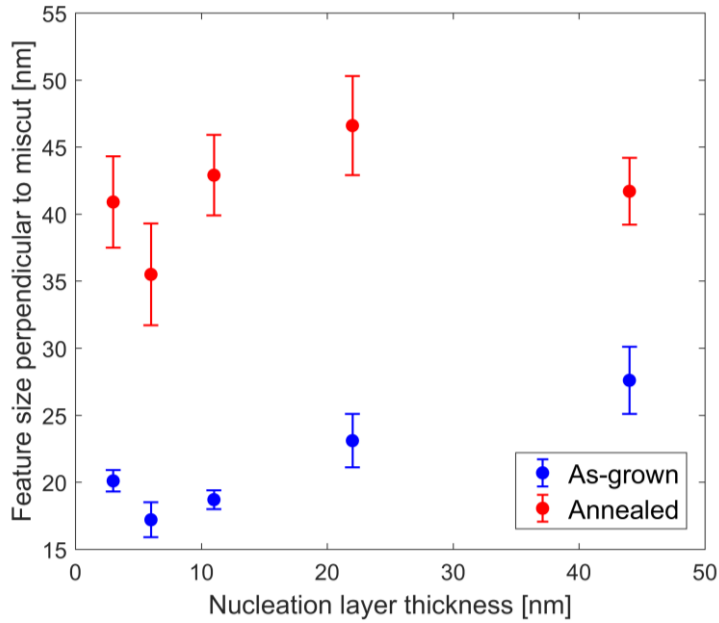


Figure 5.21: Characterizations of the feature sizes on the surfaces of as-grown and annealed samples with the NLs grown on 2° miscut 3C-SiC template.

The AFM topography images of annealed NLs are shown in Figure 5.22. They display elongated “island-like” features seen previously in Figure 5.20 for as-grown NLs. However, the islands of as-grown NLs have ripened during annealing, as demonstrated by the increase of the feature size in Figure 5.21. The origin of this effect can be enhanced diffusion of the material that allows rearrangement of the material, reduction of surface energy and, consequently, Ostwald ripening of individual GaN islands. At higher temperatures, the diffusion takes place at higher rates and the system is able to get to a state with lower energy more readily.

The above-mentioned process of island ripening results in an outdiffusion of the material from other parts of the surface, which exposes the substrate underneath. The surface coverage of annealed NLs was analyzed, and the results are summarized in Figure 5.23. The thicker NLs (11, 22, 44 nm) exhibit almost complete coverage, but this significantly drops for NLs with thicknesses of 3 nm and 6 nm. There may be several possible reasons for this phenomenon. Firstly, higher diffusion rate leads to faster rearrangement of the material on the surface. This correlates well with the observed increase of the feature size after annealing in Figure 5.21. Secondly, the material may be etched away by the reactor atmosphere or desorbed from the surface. We have employed XRD to decide which of these two mechanisms is responsible for the reduced surface coverage, or if it is a combination of both.

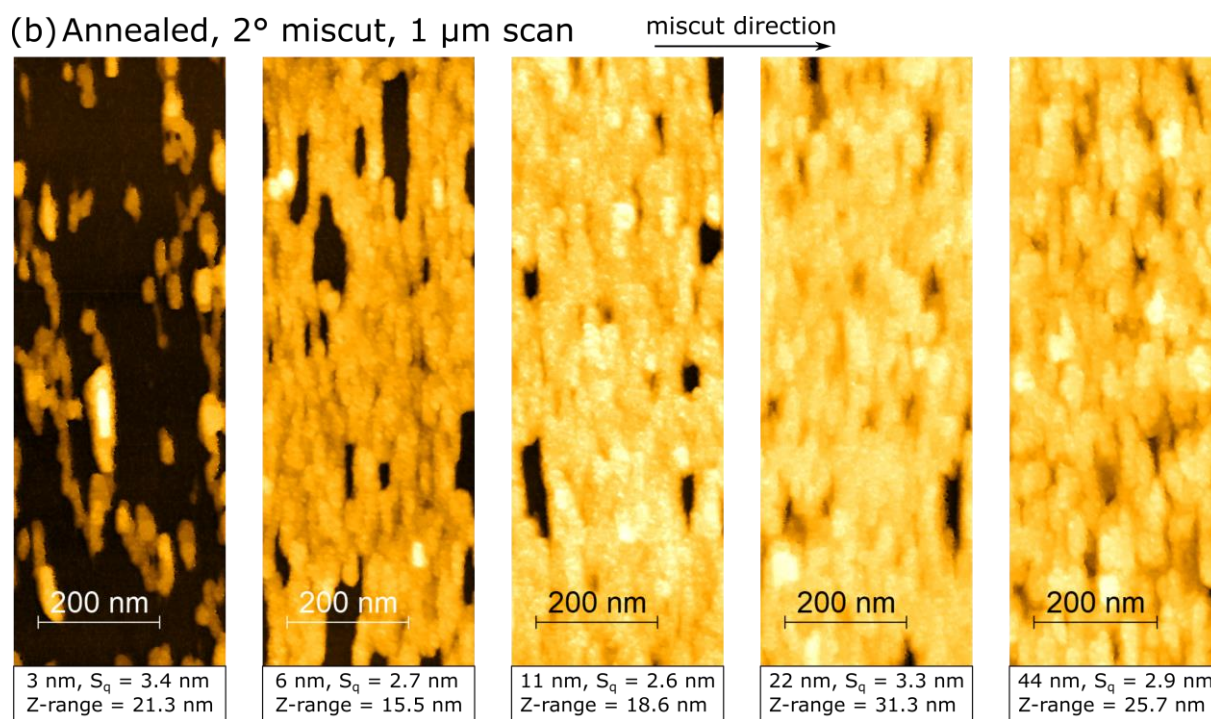
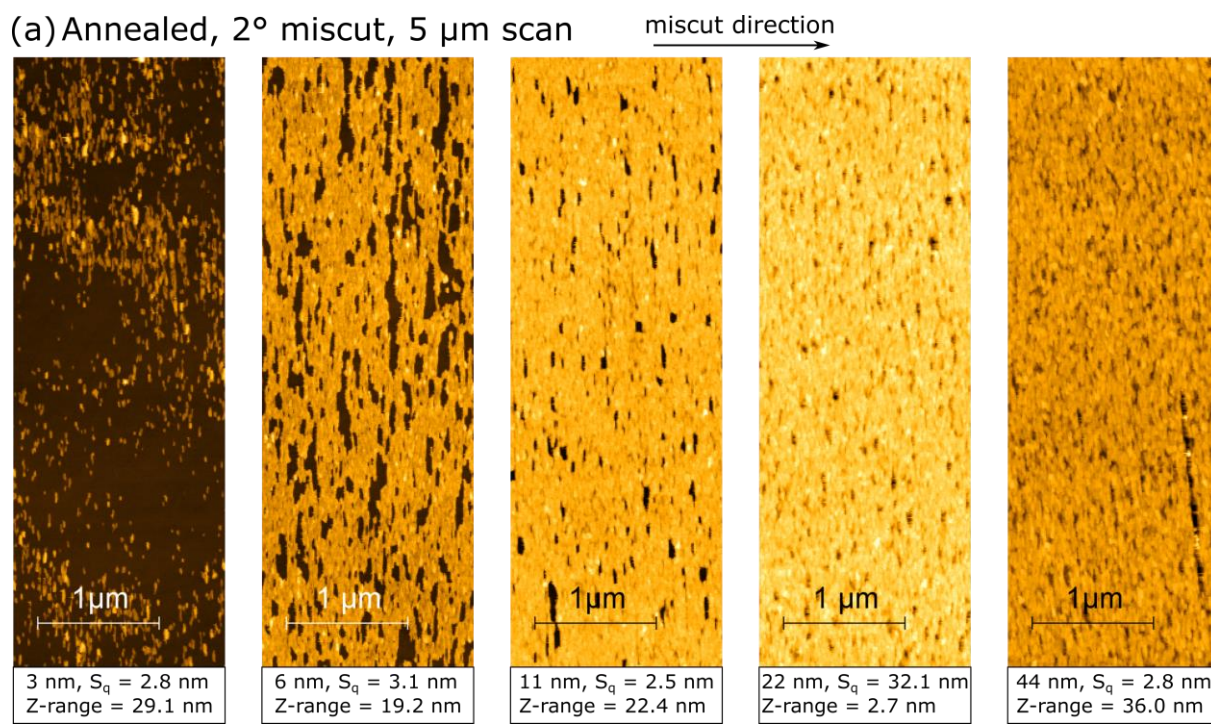


Figure 5.22: The AFM topography images of annealed NLs with the same miscut direction in all images. The images in (a) are large-area scans with vertical range of $5\ \mu\text{m}$, whereas those in (b) are high-resolution images with the vertical range of $1\ \mu\text{m}$. The meaning of the symbols in the legend at the bottom of each panel is the same as written in the caption of Figure 5.20.

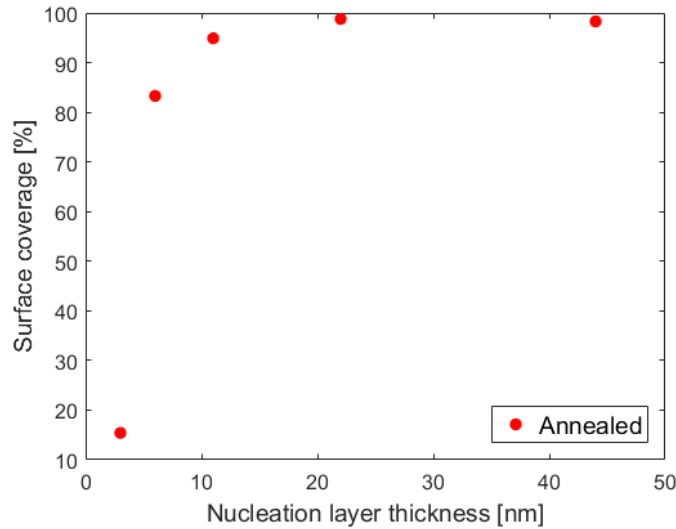


Figure 5.23: The surface coverage of samples with annealed NLs grown on 3C-SiC template with 2° miscut.

The ω - 2θ scan of the sample with 6 nm thick NL is shown in Figure 5.24(a). The intensity ratio of the GaN/SiC 002 peak from the ω - 2θ scans, see Figure 5.24(b), was calculated to account for the absolute intensity variance across samples and correlates with the amount of the material present in the sample. For most of the NL thicknesses, this ratio, obtained from the annealed samples, is lower than the ratio obtained from the as-grown samples, which can be attributed to the loss of material by etching or desorption taking place after annealing. For most of the samples this difference is small. However, for the thinnest NLs (3 nm, 6 nm) the relative difference between as-grown and annealed samples is significant, especially for the 3 nm sample. We assume that the larger separation and surface area of the islands in the thinnest NLs makes them inherently susceptible to etching by the reactor atmosphere or to desorption.

To conclude, there are both mechanisms present. The morphologies of GaN islands are modified due to diffusion, which leads to an increase of the feature size. At the same time, some material is desorbed or etched away, as proven by XRD in Figure 5.24.

XRD analysis also revealed the strain relaxation in thicker NLs. The relaxed zb-GaN has a lattice constant of 0.4506 nm which corresponds to the 2θ angle of 39.9845° [85,87]. In all NLs, a compressive in-plane strain and tensile strain in the growth direction is present. The thinnest NL has the highest strain, and the strain is decreasing with increasing NL thickness until it reaches almost fully relaxed state for the 44 nm thick NL which is illustrated by positions of the 002 zb-GaN peaks in Figure 5.25(a). The trend is the same for the as-grown and annealed samples as is visible in Figure 5.25(b). Additionally, annealing also causes strain relaxation. Higher temperature during annealing increases the defect mobility and enables the material to plastically relax elastic strain induced during the growth. Lower strain in the thicker NLs could be explained by the nucleation of defects as it becomes energetically beneficial to form a defect rather than maintain the elastic energy in the layer. Strain can be also reduced by the three-dimensional growth where the island can elastically expand into its surrounding space.

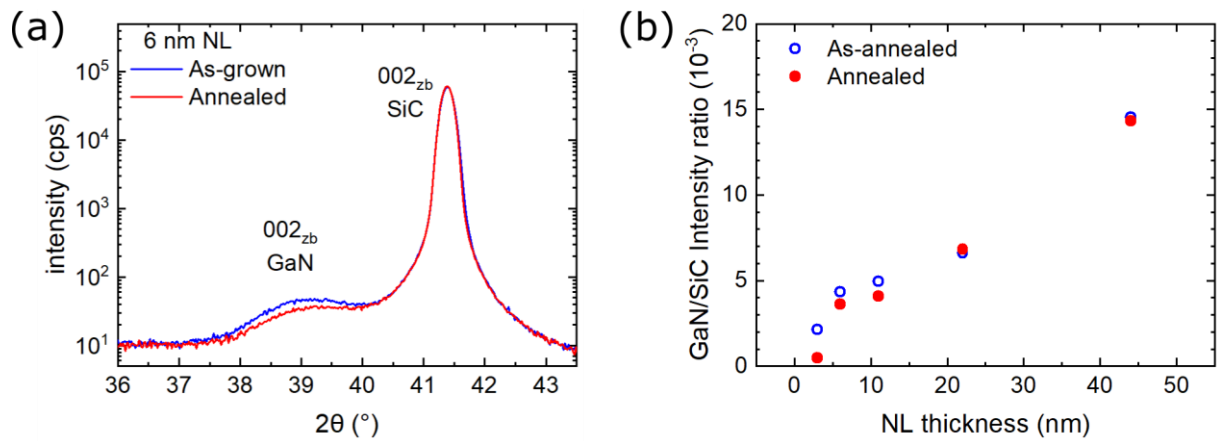


Figure 5.24: The ω - 2θ scan of the sample with 6 nm thick NL (a) and the intensity ratios of GaN/SiC 002 peaks of as-grown and annealed samples (b).

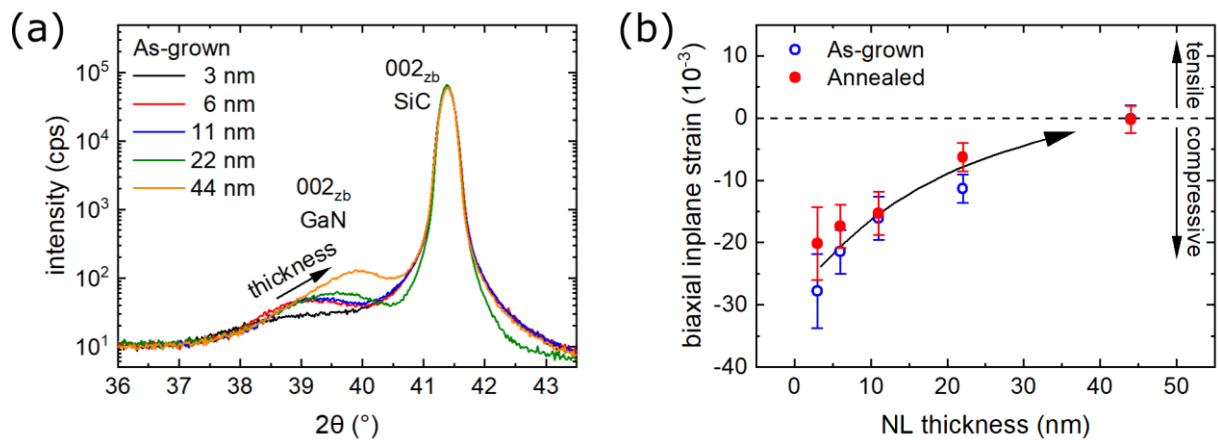


Figure 5.25: The ω - 2θ scan showing the 3C-SiC and zb-GaN 002 peaks of all as-grown 2° miscut samples indicating the shift of the zb-GaN 002 peak, the dashed line indicates position of the fully relaxed zb-GaN 002 peak (a); calculated in-plane biaxial strain of all as-grown 2° miscut samples.

Antiphase domains are present in some of the samples with 2° miscut. The islands in the antiphase domain region are elongated in the direction perpendicular to the surrounding islands as shown in Figure 5.26(a) and (b). Some of these islands do not have direct connections to the normally aligned islands. Therefore, the observed misalignment must be caused by the presence of an antiphase domain in the substrate and not by nucleation of the antiphase domain boundary and further growth of the island in the perpendicular direction. Furthermore, the perpendicular alignment of the islands begins in the nucleation stage. The elongation probably comes from

the potential valleys along the $\langle 110 \rangle$ directions present on GaN (001) surface [86]. These potential valleys are oriented perpendicularly in the antiphase domains, which causes a different orientation of the islands inside the antiphase domain region.

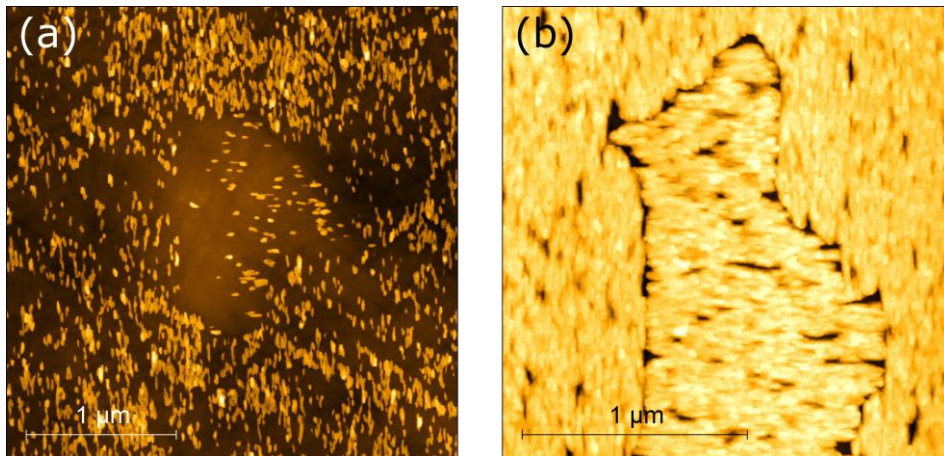


Figure 5.26: AFM topography of the annealed 2° miscut NL samples with the antiphase domains visible, the layer thickness is 3 nm (a) and 22 nm (b) and Z-range is 19.9 nm and 32 nm, respectively.

Facets in nucleation layers

In order to further characterize the morphology of the NLs, we have employed TEM and AFM to investigate the structures of facets of well-separated islands in the annealed sample with 3 nm NL. When measuring the angle between the plane of the substrate and the plane of the GaN island facet, it is important to take into account the miscut of the substrate. For non-zero miscut, one expects one steeper and one shallower facet, as illustrated in Figure 5.27. In particular, for a 2° miscut, the angle of the shallower facet would be 2° smaller, whereas the angle of the steeper facet will be 2° larger than the facet angle on the substrate without miscut.

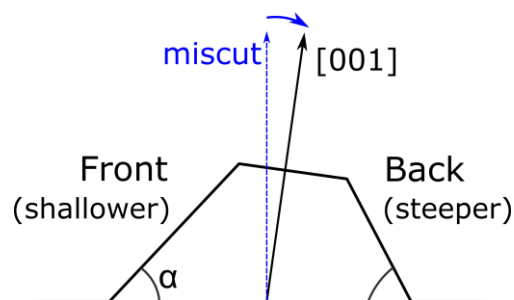


Figure 5.27: Illustration of the effect of miscut on the angles of the front and back facets, where the image plane is $(1\bar{1}0)$.

The facet angles were measured from the AFM line scan profiles and from cross-sectional TEM images. They are represented by the histograms shown in Figure 5.28(a) and (b) for the front and back facets, respectively. From both histograms and from the mean value of the facet angles shown in Table 2, one can see that the mean surface angles for the front and back facets are different. This is due to the effect of miscut as discussed earlier.

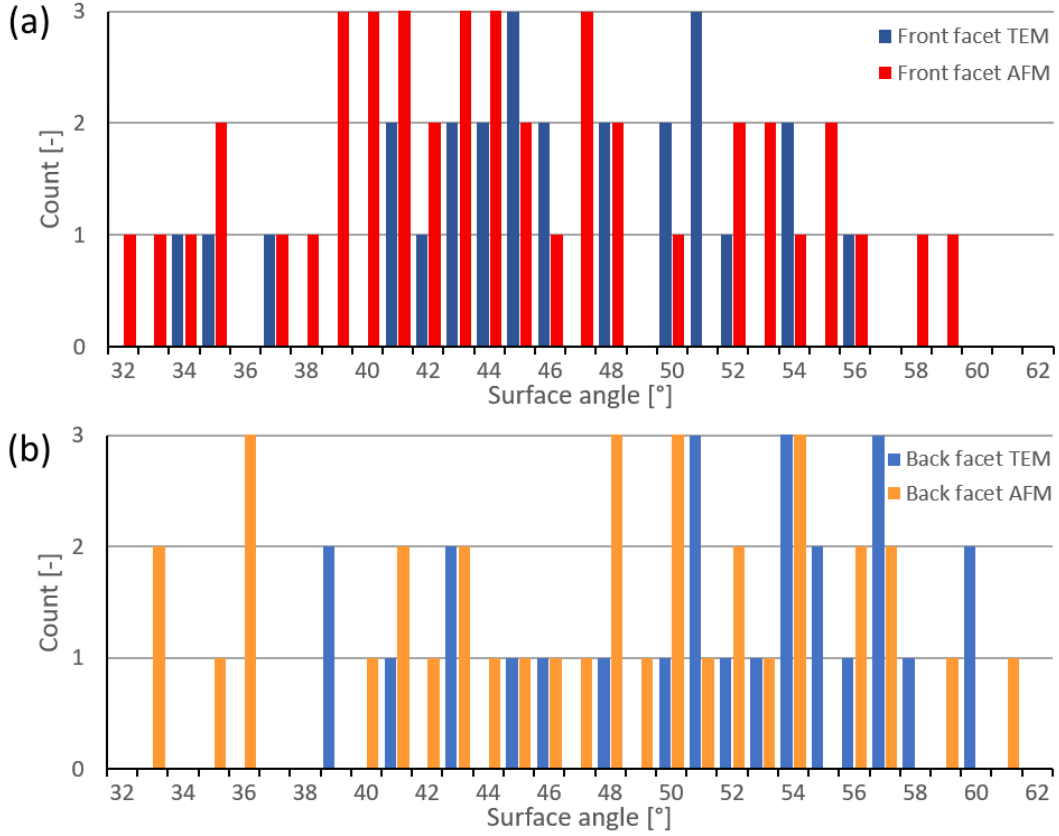


Figure 5.28: Histograms of the facet angles obtained from AFM and TEM for: (a) the front facet, and (b) the back facet.

Table 2: Mean values of the angles of facets measured to the surface of the substrate, with the error bars indicated.

	TEM	AFM
Front facet	$43.9^\circ \pm 1.6^\circ$	$44.5^\circ \pm 1.0^\circ$
Back facet	$50.2^\circ \pm 1.6^\circ$	$47.8^\circ \pm 1.2^\circ$

The observed facets are further summarized in Table 3, where they are characterized by their angles (defined in Figure 5.27) and the closest low-index plane. We have verified that annealed samples with 3 nm thick NLs contain $\{111\}$ facets, in agreement with Table 3. It is

currently not known whether these $\{111\}$ facets are present also in coalesced samples. If so, it is important to understand how they influence further growth and the formation of defects.

Table 3: Possible facet angles to the $[001]$ direction (see Figure 5.27) in the angular range investigated.

Possible facets	$\{111\}$	$\{335\}$	$\{112\}$
Facet angle to $\{001\}$	54.7°	40.3°	35.3°

The presence of $\{111\}$ facets may induce nucleation of SFs or inclusions with the wurtzite structure, as was previously discussed in the literature [88,89]. The zincblende and wurtzite structures differ in the stacking sequence of close-packed planes ($\{111\}$ for zincblende and $\{0001\}$ for wurtzite): zincblende has ABCABC stacking and wurtzite ABAB stacking of double layers. Therefore, if there are $\{111\}$ facets present in the zb-GaN layers, it may induce the formation of wurtzite inclusions and SFs, by locally altering the stacking sequence of the material. There are other possible mechanisms for SF formation, which will be discussed in the next section.

5.2.2 Stacking faults and dislocations in zincblende GaN

The presence of crystallographic defects in the GaN NL samples was investigated by TEM. The samples for TEM imaging were prepared using two techniques: (i) manual grinding and polishing, followed by argon-ion final polishing, and (ii) focused ion beam milling. All samples were prepared as cross-sections perpendicular to the growth direction. They were further oriented in the $\langle 110 \rangle$ direction.

Stacking faults (SFs) are the most common extended defects present in the zb-GaN layers. They occur in very high densities and may negatively impact the optical properties of the material as was suggested by photoluminescence studies of Church et al. [90] and cathodoluminescence studies by Kemper et al. [91]. Therefore, further study of SFs and associated partial dislocations is necessary to understand role of these defects and, consequently, to find ways to reduce their densities.

Figure 5.29 shows an overview STEM image of as-grown 22 nm thick NL sample with 4° miscut substrate. It consists of three layers: Si (001) substrate, approx. 3 μm thick 3C-SiC template, and zb-GaN NL. The bright lines in SiC represent SFs, one of which is highlighted in red. They are present in the entire layer with higher density at the Si/SiC interface. The objective in the following is to characterize the SFs and dislocations in the zb-GaN layers and discuss their possible nucleation mechanisms and their impact on the strain relief.

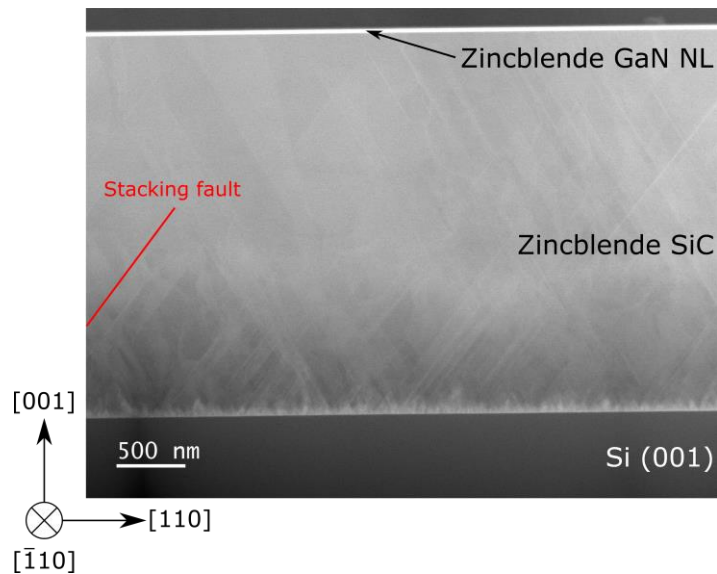


Figure 5.29: High-angle annular dark field (HAADF) STEM image of as-grown 22 nm thick sample with 4° miscut NL taken on $[\bar{1}10]$ zone axis. SFs in SiC are visible as bright lines (one of them is highlighted in red).

Since the GaN NLs are only 3-44 nm thick, high-resolution TEM was employed to investigate the crystallographic defects present. The spacing of defects in SiC near the SiC/GaN interface is very large and there are very few defects visible in SiC in the high-resolution STEM images (no defects are present in SiC in Figure 5.30). However, there is a large number of defects generated in GaN NLs near the interface with SiC. The impact of defects penetrating from SiC into GaN is negligible compared to the number of defects nucleated at the SiC/GaN interface. Also, there is no amorphous layer at the interface, which confirms good epitaxy of the GaN film on SiC. The N and C atoms, in GaN and SiC respectively, are not visible in the HAADF STEM images. The intensity of Z-contrast images in HAADF is governed by the square of the atomic number of the element present in the sample. The intensity ratio of Ga to N is 19.6 and thus Ga atoms will be 19.6 times brighter than N atoms, which explains the difficulty of imaging N atoms in GaN.

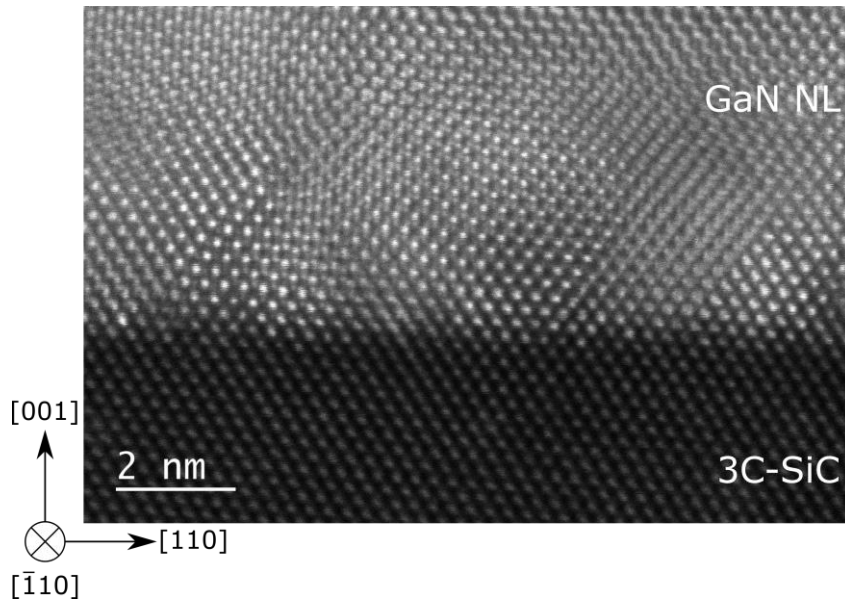


Figure 5.30: HAADF high-resolution STEM image of SiC/GaN interface of as-grown 22 nm thick sample with 4° miscut NL. The GaN NL contains a large density of defects, whose presence is manifested by smearing the contrast arising from individual atoms. No defects are present in the SiC layer.

Stacking faults in the zb-GaN viewed in the $\langle 110 \rangle$ direction can appear as a discontinuity of the stacking sequence or as a “hexagonal pattern”. The discontinuity of the stacking sequence (Figure 5.31(a)) is visible for the SF on the planes belonging to the zone whose zone axis is identical to the viewing direction. In the zb-GaN STEM images, $[\bar{1}10]$ viewing direction was used, so the discontinuity of the stacking sequence was observed for the SF on (111) and $(11\bar{1})$ planes. The hexagonal pattern is caused by the SFs in the zone whose zone axis is perpendicular to the viewing direction, e.g. $(\bar{1}11)$ and $(1\bar{1}1)$ for the $[\bar{1}10]$ viewing direction. The difference between the discontinuity of stacking sequence and the hexagonal pattern can be illustrated by viewing a block of atoms containing the intrinsic SF from two perpendicular $\langle 110 \rangle$ directions. The FCC lattice was used for simplicity and because only the Ga atoms are visible in STEM images. This makes the observed zincblende structure to look like FCC. The illustration of an intrinsic SF on the (111) plane in the $[\bar{1}10]$ projection of the FCC lattice is shown in Figure 5.32(a). The SF is clearly visible as an error in the regular stacking sequence of (111) planes. The projection in Figure 5.32(b) is obtained by rotating the structure from Figure 5.32(a) by 90° around the [001] axis, which results in the same hexagonal pattern shown in the STEM image in Figure 5.31(b). This confirms that the observed hexagonal pattern is the result of a SF in the zone whose zone axis is perpendicular to the viewing direction.

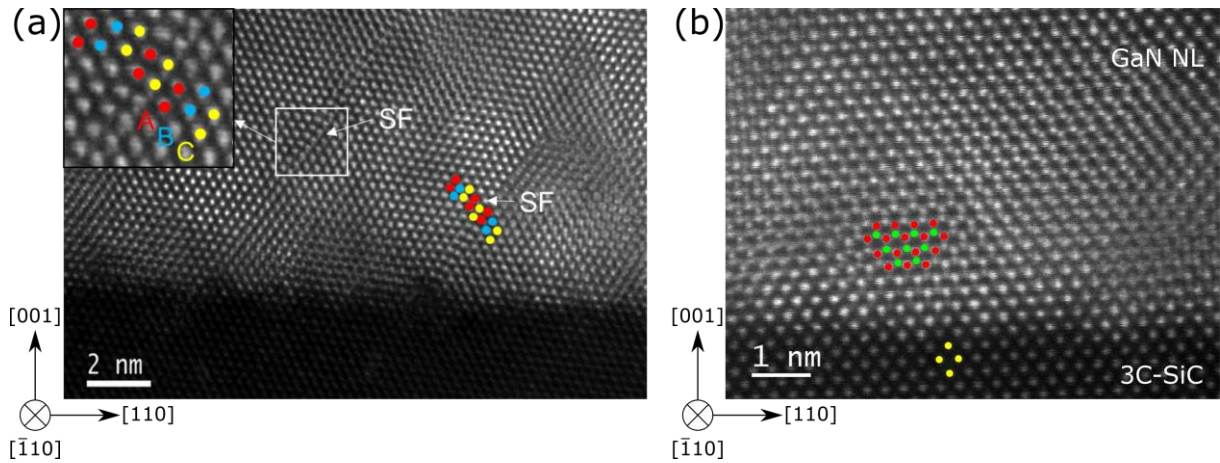


Figure 5.31: STEM image of the GaN NL with a highlighted SF visible as the discontinuity of the stacking (a) and hexagonal pattern (b).

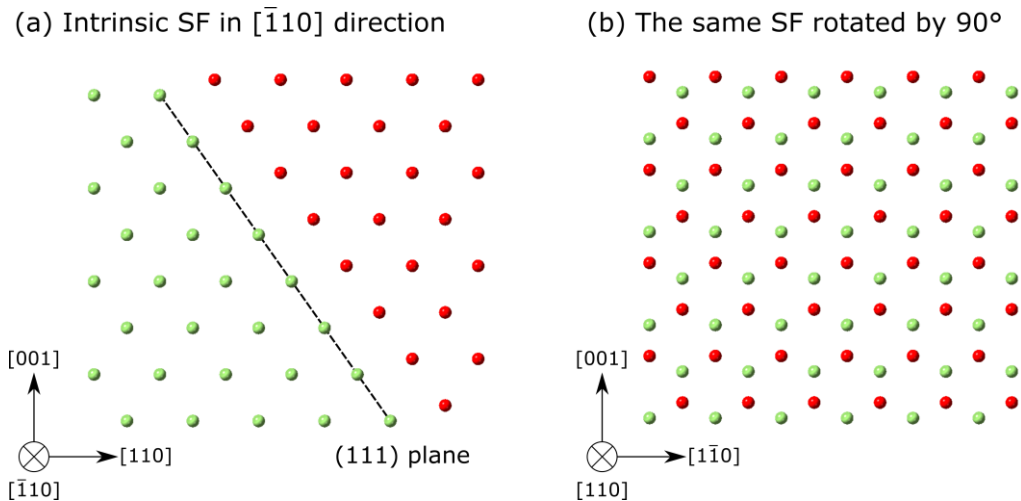


Figure 5.32: Two basic representations of intrinsic SFs in high-resolution TEM images: (a) fault in the FCC lattice in the projection perpendicular to the $[\bar{1}10]$ axis (the unshifted atoms are green, those shifted by the presence of the SF are red), (b) the same SF but viewed in the projection perpendicular to the $[110]$ direction rotated by 90° around the $[001]$ axis from (a).

Stacking faults, perfect and partial dislocations were the most prevalent extended defects observed in the zb-GaN NL layers. Perfect dislocations were identified as 60° mixed with $1/2\langle 110 \rangle$ Burgers vectors and were located at the GaN/SiC interface. Partial dislocations located at the interface were identified as 30° Shockley partials with $1/6\langle 112 \rangle$ Burgers vector. Some of the 30° Shockley partials were also found at some distance away from the interface. SFs mostly extended from the interface to the surface. In the cases when the SF did not reach the surface and was terminated inside the layer, it was bounded at one end by 90° Shockley partial dislocation. This arrangement corresponds to the extended 60° perfect dislocation and it is the

evidence of the dissociation of 60° perfect dislocations into 30° and 90° Shockley partials in zb-GaN NLs. Figure 5.33 shows all the options for the Shockley partials mentioned above. In some cases, the SF was bounded by the Lomer-Cottrell stair rod partial dislocation with $1/6\langle 110 \rangle$ Burgers vector. The Lomer-Cottrell dislocations were always located exactly at the GaN/SiC interface, as shown in Figure 5.34(a). The stair rod dislocations were a minority compared to the other types of dislocations present in zb-GaN. Even though, a majority of the SFs were of intrinsic type, some extrinsic SFs were observed as well. An extrinsic SF in zb-GaN was observed only when an extrinsic SF from SiC penetrated into the GaN layer, as shown in Figure 5.34(b).

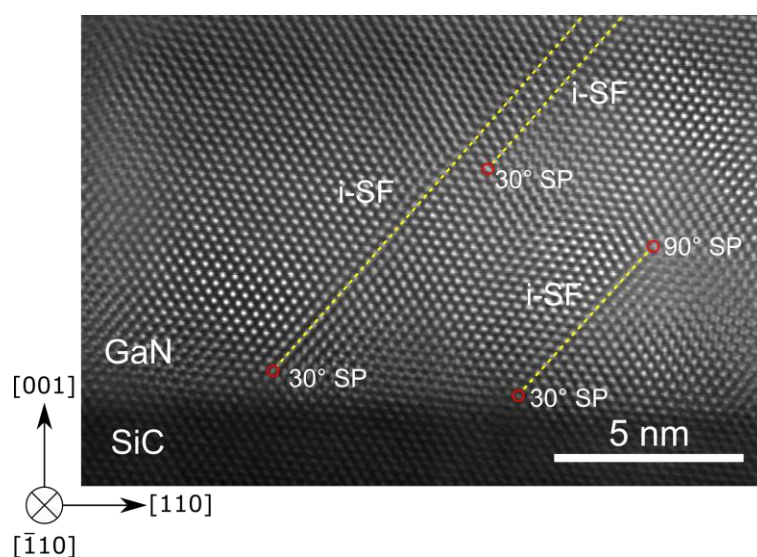


Figure 5.33: STEM image of GaN layer with intrinsic SF (denoted as i-SF in the figure) highlighted by yellow dashed line and partial dislocations highlighted by the red circle. 30° Shockley partials are located at the surface or at some distance away from it. The 60° extended perfect dislocation consisting of 30° and 90° Shockley partials and intrinsic SF is present.

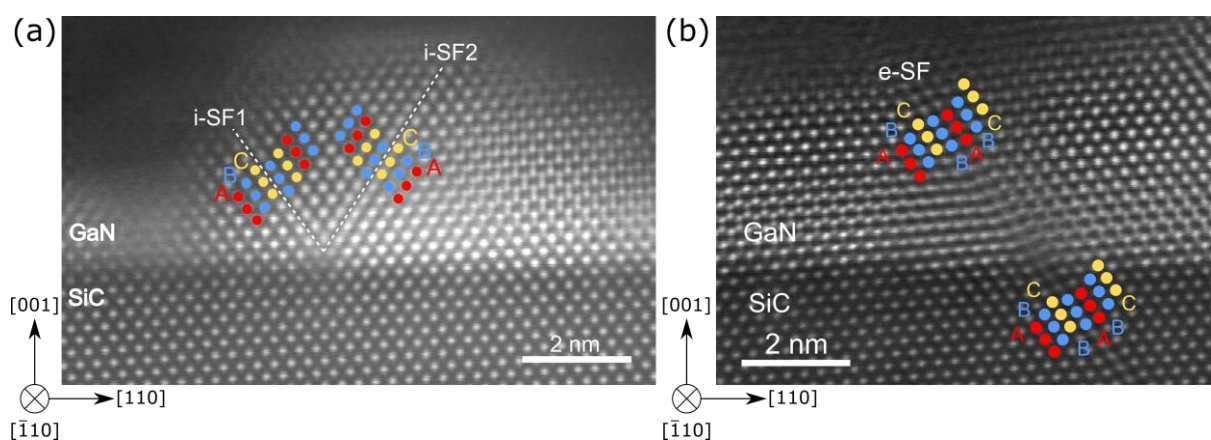


Figure 5.34: High-resolution images of zb-GaN NLs with a Lomer-Cottrell partial dislocation and associated intrinsic SFs (noted as i-SF in the figure) (a) and extrinsic SF (noted as e-SF in the figure) penetrating from SiC to GaN (b).

There are several possible mechanisms, how to nucleate a SF. Firstly, the presence of {111} facets may induce a SF and wurtzite formation as was discussed in the previous section. Secondly, SFs could be generated by agglomerations of vacancies. Vacancies are expected to be present in zb-GaN layers, because of the relatively low deposition temperature (approx. 600 °C), and consequently low diffusivity of atoms on the surface. The atoms are then unable to reach all lattice positions, which results in the formation of vacancies in the film. Vacancies could then diffuse and agglomerate on some close-packed plane and form a SF bounded at one end by the $1/3\langle 111 \rangle$ Frank partial dislocation [30]. Basal plane SFs bounded by the Frank partials were observed in the low temperature wurtzite GaN layers [71] and, therefore, could be also present in zb-GaN NLs. The analysis of the zb-GaN NLs did not prove the presence of any Frank partial dislocations. It is therefore not probable, that agglomeration of vacancies is the prevalent mechanism of SF formations in zb-GaN.

Another possible mechanism of the SF formation is the dissociation of perfect dislocations already present in the layer. Both undissociated 60° perfect dislocations and even the 60° perfect dislocation dissociated into the 90° and 30° Shockley partial dislocations bounding the SF were observed. Dissociation of the perfect dislocation in FCC, cubic diamond, and zincblende structures could be described by the dislocation reaction: $1/2\langle 110 \rangle \rightarrow 1/6\langle 211 \rangle + 1/6\langle 12\bar{1} \rangle$. According to the Frank's rule [27,30], this reaction is energetically favorable, because it leads to the reduction of energy. This mechanism could explain why the density of perfect dislocations is lower compared to the density of partial dislocations. However, high density of perfect dislocations had to be present initially to explain high density of SF observed in the zb-GaN NLs. We thus expect that also other mechanisms are operative during the growth of zb-GaN layers.

One of these possible mechanisms is the nucleation of Shockley partial dislocation half-loops on the surface. These could then glide on the {111} planes from the surface to the interface while dragging the SF in between. The arrangement where the SF extends from the surface to the interface and is terminated there by the Shockley partial dislocation is common in zb-GaN layers. Additionally, partial dislocations have smaller Burgers vectors than perfect dislocations and thus they require less energy to nucleate. This might make their nucleation close to the surface preferable over the nucleation of perfect dislocations. It is common that the SFs are extended from the interface to the surface, even for layers several hundred nm thick. Therefore, the thing to consider is the impact of the SF energy. In a majority of materials, the SF energy is positive which sets bounds on the SF area. However, in the case of SF in zb-GaN the SF energy might be negative because its stacking sequence (e.g. ABCABABC for the intrinsic SF) locally resembles the stacking sequence of a more stable wurtzite structure (ABAB). A few-layer SF may thus give rise to a negative SF energy in zb-GaN. This assertion is supported by the calculations of Wright [92] and Glas [93], who estimated the SF energy to be negative in all III-nitrides with the zincblende structure. Therefore, introducing a SF into zb-GaN layers might actually reduce the overall energy of the system.

We conclude that the most probable mechanisms for nucleation of SFs are dissociation of perfect dislocations and nucleation of partial dislocation half-loops on the surface. Perfect dislocations were present in very low numbers and dissociated 60° perfect dislocations were

observed. Also, SFs extending from the surface to the interface were often observed and the 30° Shockley partials were able to relieve the misfit strain as shown later in the text.

The origin of the Lomer-Cottrell partial dislocations should also be considered. They were always located exactly at the GaN/SiC interface and thus it is highly unlikely that they are formed by dislocation reaction between two Shockley partial dislocations that glide through the layer and meet exactly at the interface. We propose an alternative mechanism. If a SF is already formed and one of its Shockley partials is located at the interface, then another Shockley partial and a Lomer-Cottrell partial dislocation can nucleate from it according to the reaction: $1/6[\bar{2}11] \rightarrow 1/6[\bar{1}\bar{1}0] + 1/6[\bar{1}21]$. This reaction is not energetically favorable according to the Frank's rule, but it is beneficial considering the strain relief. The Lomer-Cottrell partial dislocation accommodates twice as much strain as 30° Shockley partial. The amount of strain relief associated with the Lomer-Cottrell partial dislocation and two 30° Shockley partials is essentially equivalent. If we compare the total energy of dislocations involved in the Lomer-Cottrell lock (Lomer-Cottrell partial dislocation and two Shockley partials) and two SFs nucleated separately (four Shockley partials), then the total energy of the Lomer-Cottrell lock is lower than the two SFs bounded by the Shockley partials. In some cases, it might be beneficial to nucleate a Lomer-Cottrell lock from the existing Shockley partial instead of the nucleation of a separate SF. Similar mechanism was proposed by Kozak et al. [94] for the nucleation of the Hirth lock.

Strain relief

The epitaxy of zb-GaN on 3C-SiC results in compressive in-plane strain that originates from lattice mismatch between both structures [87]. The associated strain energy can be relieved by the nucleation of defects during the growth of the NL. As was discussed in the previous section, the compressive in-plane strain is reduced with increasing thickness, which suggests that defects are formed throughout the growth of the NLs.

Dislocations are able to relieve the lattice mismatch strain and were observed in NL samples. Both perfect and partial dislocations contribute to the strain relief by the edge component of their Burgers vector located in the plane parallel to the interface. To evaluate the contribution of each dislocation type on the strain relief, one needs to determine the projection of their edge component onto the interface between the film and the substrate. In the following, the $[\bar{1}10]$ dislocation line vector was considered, because all TEM images were taken using this viewing direction and all identified dislocations had $\langle 110 \rangle$ dislocation line vector. The projections were calculated into $[110]$ and $[\bar{1}\bar{1}0]$ directions. The projected length of dislocations in zb-GaN is $a/2\sqrt{2} \approx 0.159$ nm for 60° perfect dislocations, $a/6\sqrt{2} \approx 0.053$ nm for 30° Shockley partial dislocations, $a/3\sqrt{2} \approx 0.106$ nm for 90° Shockley partial dislocations, and $a/3\sqrt{2} \approx 0.106$ nm for Lomer-Cottrell partial dislocations, with a being the lattice constant of zb-GaN [94]. The 60° perfect dislocation relieves the largest amount of strain, but strain relief by partial dislocations should not be neglected. Compared to the 60° perfect dislocation, 30° Shockley partial relieves 1/3 of the strain, and both 90° Shockley partial and Lomer-Cottrell partial dislocations relieve 2/3 of the strain. The abundance of partial dislocations together with significant amount of strain relieved by them, leads to the conclusion that a majority of the

strain in the zb-GaN layers is relieved by the partial dislocations instead of the perfect dislocations.

Depending on the position of the “half-plane”, the 60° perfect dislocations are able to relieve compressive and tensile strains in the layer. The Lomer-Cottrell partial dislocation is also able to relieve compressive and tensile strains. The 30° Shockley partial dislocation located at the interface relieves only the compressive strain in the layer and the 90° Shockley partial located at the interface relieves only tensile strain [95,96]. One should bear in mind that, this is only true for the Shockley partial located at the interface. The second partial located in the layer, which belongs to the same extended 60° perfect dislocation, relieves the same type of strain as the partial located in the interface. The dislocations observed in the zb-GaN layers (60° perfect, 30° Shockley partials, and Lomer-Cottrell dislocation) are able to relieve compressive in-plane strain present in the layers, which is in agreement with theoretical predictions. This also explains why no 90° Shockley partial located in the interface was observed, since they can only relieve tensile strain.

5.2.3 Interaction of stacking faults in zincblende GaN

The SF density in the zb-GaN is very high, and thus many interactions between SFs have to occur. This makes zb-GaN grown on 3C-SiC an ideal material to study how the SFs interact and the mechanisms that govern their behavior. Transmission electron microscopy and computer simulations were employed to study these phenomena.

For this study, a 500 nm thick zb-GaN epilayer was grown on 22 nm thick NL analyzed in the previous chapter. These layers were grown on 3C-SiC (001) templates with 2° miscut towards the [110] direction by MOCVD. Approx. 600°C was used for the NL growth and 885 °C for the epilayer growth.

Transmission electron microscopy

TEM was used due to its ability to resolve individual crystallographic defects in the zb-GaN layers. Diffraction contrast was used to determine the structure of SFs in the layer. Figure 5.35 shows a bright field STEM image of zb-GaN grown on 3C-SiC. The SFs are represented as dark straight lines and are present throughout the entire layer. It is also evident that the density of SFs is higher at the interface with SiC than near the surface. SFs often intersect each other, but sometimes they are stopped by another fault formed on an intersecting plane. In some cases, one SF stops propagating while the other continues to extend to the surface. Other times both SFs are terminated. A high-resolution STEM was employed, in order to investigate the intersections of these SFs in more detail.

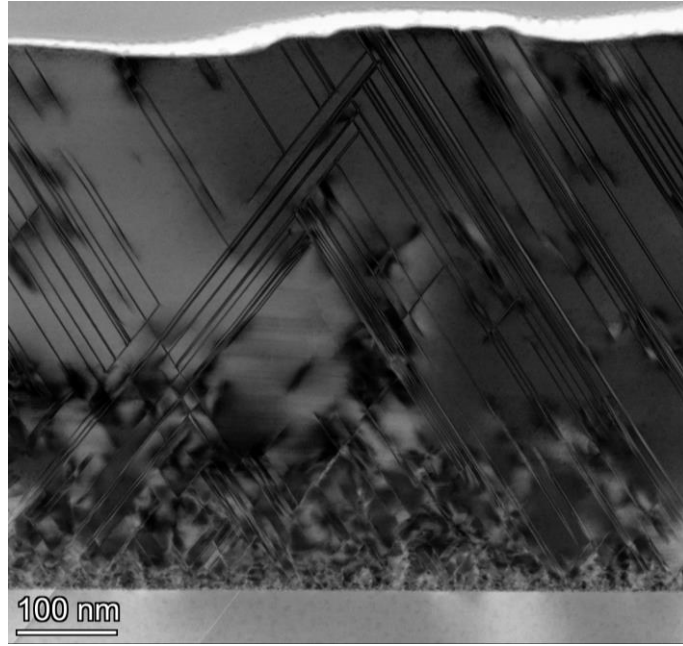


Figure 5.35: Bright field STEM image of zb-GaN layer taken using $g = 110$ near $[\bar{1}10]$ zone axis. SFs are represented as dark straight lines.

The high-resolution STEM images are shown in Figure 5.36. Four possibilities for the interactions of SFs were observed. The most frequent was intersection of the two SFs where both of them continue extending further into a layer. More on the structure of the intersection of SFs could be found in the theoretical work of Antoš et al. [38]. Another possibility is the annihilation of both SFs. In this case, when the two SFs meet, they stop propagating further, thus reducing the SF density. However, this is the least frequent scenario observed. We have also observed that one SF stopped propagating while the other continued further. The halted SF can be positioned either above or under the second SF, as shown in Figure 5.36 (c) and (d), respectively. One possible explanation of this behavior is that one SF is already present in the layer and the other extends from the surface or from the interface, as was suggested in Chapter 5.2.2. The gliding SF meets the one already present, which stops its propagation.

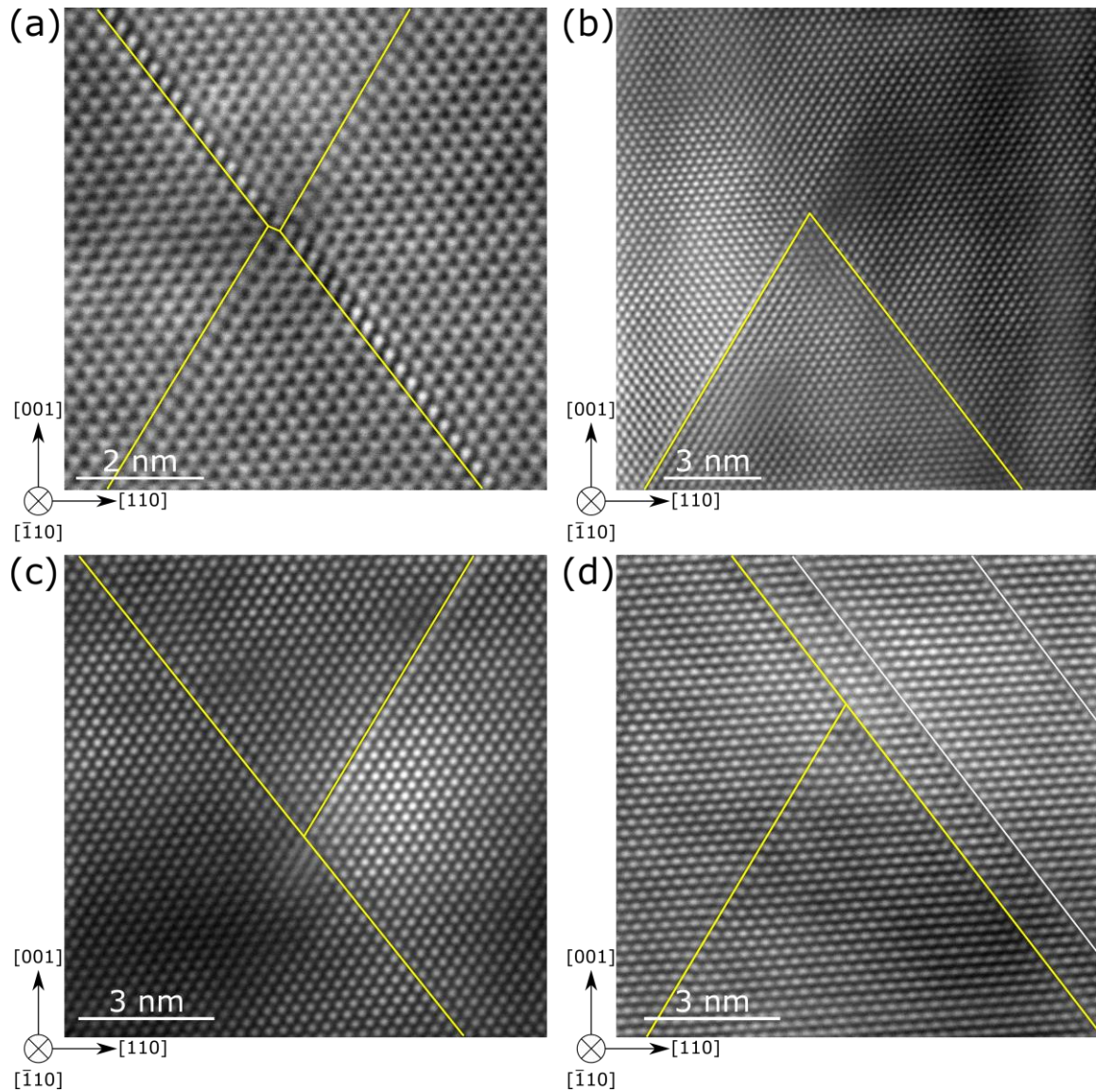


Figure 5.36: High-resolution STEM images of zb-GaN layers showing the possibilities for the SF interaction: intersection (a), annihilation (b), one SF is terminated (c) and (d), interacting SFs are highlighted by yellow lines and other SFs by white lines.

When the SFs intersect, they may also annihilate. This case might be reconciled by considering an interaction of partial dislocations bounding the SFs. There are 6 possible $1/6\langle 112 \rangle$ Burgers vectors of Shockley partial dislocations in each $\{111\}$ plane of the zincblende structure. Partial dislocations bounding the SFs on different $\{111\}$ planes can react with each other. If the dislocation reaction is energetically favorable, the SFs might annihilate. If it is not favorable, they might intersect. With 6 possible partial dislocations in each $\{111\}$ plane, there are 36 possible reactions between dislocations in two different $\{111\}$ planes. All possible reactions of partial dislocations in the (111) and $(\bar{1}\bar{1}\bar{1})$ planes are shown in Table 4. Out of the 36 possible reactions, 18 are energetically unfavorable. Out of the remaining 18 energetically favorable reactions, 10 have energies of the resulting dislocations that are very close to the

energy of dislocations coming to the reaction, and thus there might not be sufficient driving force for this dislocation reaction. Only 8 out of 36 reactions offer significant energy savings. The resulting dislocations are called the Lomer-Cottrell partial dislocation and the Hirth partial dislocation with the $1/6\langle 110 \rangle$ and $1/3\langle 100 \rangle$ Burgers vectors, respectively. These dislocations are common in materials with the FCC, diamond cubic and zinblende structures [27,30]. These dislocation reactions could govern whether the two interacting SFs will intersect or annihilate. The fact that only a minority of observed SFs annihilated can follow from the observation that only 8 out of the 36 possible dislocation reactions resulted in the formation of Lomer-Cottrell or Hirth locks.

Table 4: All possible reactions of partial dislocations in the (111) and (1 $\bar{1}$ 1) planes. The possible Burgers vectors are highlighted in grey, energetically favorable outcomes of the reactions in green, and the Lomer-Cottrell and Hirth locks in darker green.

$\begin{matrix} (111) \\ (1\bar{1}1) \end{matrix}$	$\frac{1}{6}[11\bar{2}]$	$\frac{1}{6}[1\bar{2}1]$	$\frac{1}{6}[\bar{2}11]$	$\frac{1}{6}[\bar{1}\bar{1}2]$	$\frac{1}{6}[\bar{1}2\bar{1}]$	$\frac{1}{6}[2\bar{1}\bar{1}]$
$\frac{1}{6}[21\bar{1}]$	$\frac{1}{6}[32\bar{3}]$	$\frac{1}{6}[3\bar{1}0]$	$\frac{1}{3}[010]$	$\frac{1}{6}[101]$	$\frac{1}{6}[13\bar{2}]$	$\frac{1}{3}[20\bar{1}]$
$\frac{1}{6}[\bar{1}2\bar{1}]$	$\frac{1}{6}[0\bar{1}\bar{3}]$	$\frac{2}{3}[0\bar{1}0]$	$\frac{1}{6}[\bar{3}\bar{1}0]$	$\frac{1}{6}[\bar{2}\bar{3}1]$	$\frac{1}{3}[\bar{1}0\bar{1}]$	$\frac{1}{6}[1\bar{3}\bar{2}]$
$\frac{1}{6}[\bar{1}\bar{1}2]$	$\frac{1}{3}[010]$	$\frac{1}{6}[0\bar{1}\bar{3}]$	$\frac{1}{6}[\bar{3}\bar{2}3]$	$\frac{1}{3}[\bar{1}02]$	$\frac{1}{6}[\bar{2}31]$	$\frac{1}{6}[101]$
$\frac{1}{6}[\bar{2}\bar{1}1]$	$\frac{1}{6}[\bar{1}0\bar{1}]$	$\frac{1}{6}[\bar{1}\bar{3}2]$	$\frac{1}{3}[\bar{2}01]$	$\frac{1}{6}[\bar{3}\bar{2}3]$	$\frac{1}{6}[\bar{3}10]$	$\frac{1}{3}[0\bar{1}0]$
$\frac{1}{6}[121]$	$\frac{1}{6}[23\bar{1}]$	$\frac{1}{3}[101]$	$\frac{1}{6}[\bar{1}\bar{3}2]$	$\frac{1}{6}[013]$	$\frac{2}{3}[010]$	$\frac{1}{6}[310]$
$\frac{1}{6}[1\bar{1}\bar{2}]$	$\frac{1}{3}[10\bar{2}]$	$\frac{1}{6}[2\bar{3}\bar{1}]$	$\frac{1}{6}[\bar{1}0\bar{1}]$	$\frac{1}{3}[0\bar{1}0]$	$\frac{1}{6}[01\bar{3}]$	$\frac{1}{6}[3\bar{2}\bar{3}]$

Modelling of stacking fault annihilation

We have developed a simple theoretical model of SF annihilation to compare experimental results with theoretical predictions. Our approach was to create two-dimensional model to capture annihilation of SFs by using reactions of their bounding partial dislocations. FCC structure oriented in $\langle 110 \rangle$ direction was used, because of its simplicity and close resemblance to the zinblende structure. The SF starts in the first layer, which represents the interface in the real material, and then extends through the layer until it reaches the end of the layer or annihilates with another SF. The model is therefore able to simulate both the structure of SFs as well as the dependence of their density on the thickness of the film and the initial density of SFs.

The initial conditions represent the number of SFs, types of $\{111\}$ planes on which where they can propagate, the bounding partial dislocations and the distribution of SFs across the film. Every SF is at a certain distance from previous SF while distances between SFs are drawn from the normal distribution with defined mean and standard deviation. Every SF is then randomly assigned (111) or $(11\bar{1})$ plane and a random Shockley partial dislocation from this plane. When the starting conditions are set up, SFs iteratively propagate one monolayer towards the surface, while being constrained to their assigned plane. As the SFs propagate, two SFs can meet at the same lattice position. When this happens, two options are possible. If the reaction of their partial dislocations leads to lowering of the energy, both SFs are terminated and do not extend into the next monolayer. Even though the reaction resulting in creation of $1/6\langle 310 \rangle$ is energetically favorable, it was not included in the reactions causing annihilation, because it saves very little energy and might not be possible due to the kinetics of the reaction. If the reaction of partial dislocations is not energetically favorable, the SFs penetrate through each other and continue extending into further monolayers. This process is illustrated in Figure 5.37. The option when one SF annihilates and the other continues propagating is not considered, because it could not be simply explained by reactions of partial dislocations. Also, this approach does not distinguish whether the SFs have originated from the surface of the film.

The boundary conditions are defined as follows. If the SF would move out of the simulated area, it will appear in the next monolayer on the other side of the simulated area and continue to propagate further. This process is repeated until the SFs reach the end of the layer.

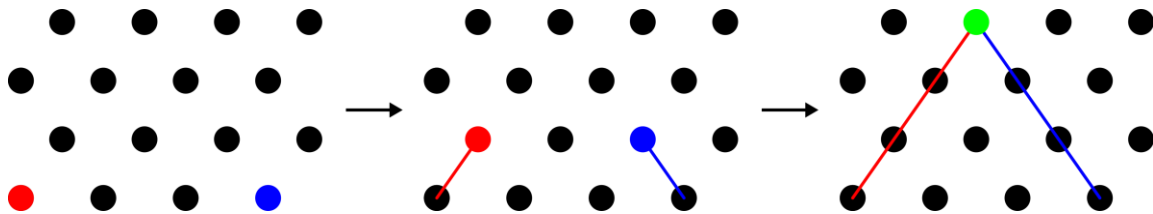


Figure 5.37: Illustration of the propagation of two non-coplanar SFs through the film in $[110]$ projection of FCC lattice. SFs are highlighted by red and blue lines and positions of their bounding partials are illustrated by red and blue dots. The termination of SFs is highlighted by green dot.

The simulated structure of SFs is shown in Figure 5.38(a). The initial SF density of approx. $2.2 \times 10^6 \text{ cm}^{-1}$ was used for all simulations, which is a rough estimate obtained from high-resolution STEM images. A few important observations could be made from the simulation. Majority of SFs are annihilated within the first 100 nm of the layer and only some SFs were able to reach the end of the layer. Both bundles of SFs as well as unfaulted areas, where there are no SFs, are present. We compared the simulation results with the experimental data on zb-GaN epilayers obtained by STEM. The bright field STEM image of a similar area as in the simulations is shown in Figure 5.38(b). This image exhibits similar features as the simulation, including the bundles of SFs, areas free of SFs, and SFs penetrating through the entire layer. Near the SiC/GaN interface, there was very high density of SFs and the diffraction

contrast in STEM did not have sufficient resolution to distinguish between them. However, in the first 50 nm the SF density decreased to the level, where they became recognizable. These experimental observations are in qualitative agreement with the simulated case, where a high number of SFs was present at the beginning and they quickly annihilated with increasing film thickness. The patterns formed by SFs are more complex in the real zb-GaN layer than in the simulated image. There are cases where one SF is annihilated and the other continues to propagate. This cannot be explained by the model and might be caused by the SF nucleating at the surface or interface, which then extends and meet with another SF already present in the layer. The propagation of a new SF could then be stopped by the second SF and create the characteristic arrangement observed in the zb-GaN layers. SFs could also be nucleated during the layer growth besides those that are formed at the beginning as in our model. SFs can also nucleate at the surface, which is another factor to consider while evaluating the results from the model. Overall, the model is able to simulate the structure of SFs present in the zb-GaN layers and exhibits similar features as the zb-GaN layers.

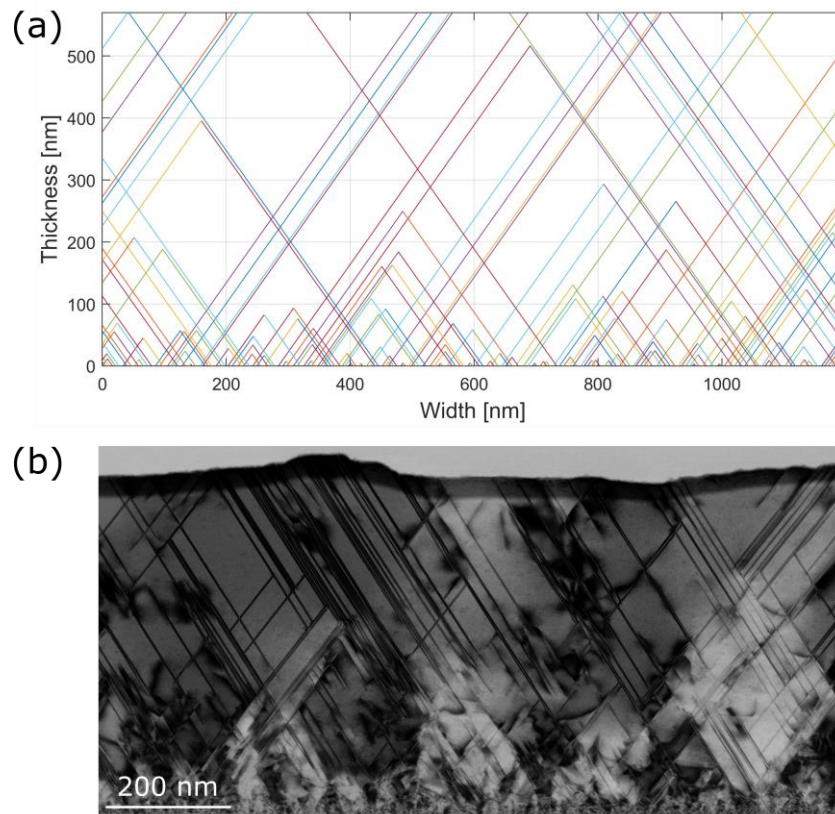


Figure 5.38: Simulated structure of SFs in the 570 nm thick layer, where lines of various colors represent the SFs (a), bright field STEM image of zb-GaN epilayer taken near $[\bar{1}10]$ zone axis using $g = 110$ with SFs visible as straight dark lines (b), both images have similar size.

In order to analyze whether the model is able to predict the decrease of SF density with increasing thickness observed in the zb-GaN layers, the density of SFs was analyzed for various distances from the interface. This density was calculated by counting the number of SFs crossing a line drawn parallel to the interface along the entire length of the FIB lamella. The SF

density was measured at 100, 200, 300, 400, and 500 nm away from the interface and the results are indicated by the red stars in Figure 5.39. The simulation that allows this comparison used much larger area to include interactions between more SFs and to suppress the randomness of the SF generation process. The result of this simulation is indicated by the blue line in Figure 5.39. It is interesting to note that, despite the simplicity of our SF interaction model, it is able to reasonably reproduce the experimental dependence of the SF density on thickness. The model unravels two stages of SF reduction. In the stage I, the SFs annihilate rapidly due to their close proximity. In the stage II, the SFs are further apart, and their interaction is not as frequent. This causes a decrease of the annihilation rate and, consequently, flattening of the SF density curve. Additionally, the first phase of the rapid annihilation of SFs is impossible to study using diffraction contrast TEM due to its insufficient resolution. However, high-resolution TEM can be potentially used to study this state of growth, but the limited field of view demands statistical averaging of the observations from several spots. Overall, the proposed model of SF annihilations is useful in the study of the structure of SFs in zb-GaN layers.

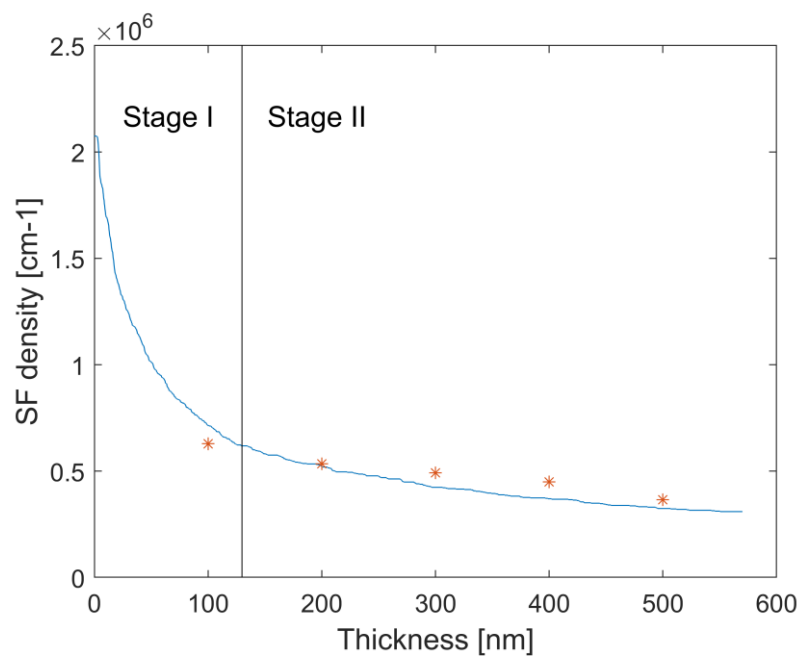


Figure 5.39: Comparison of the SF density obtained by the theoretical model (blue line) and from the experimental data (red stars).

6 Conclusions

We have investigated the structural and physical properties of extended defects in III-nitride materials grown on hexagonal and cubic structures. The wurtzite AlN/Si (111) interface was found to contain an amorphous layer composed of SiN_x and AlN. This layer has its origin either from the reaction of nitrogen precursor with Si substrate at the beginning of layer deposition, by diffusion of N into the substrate or by the combination of both. This interfacial layer could play a major role in the relief of epitaxial strain, because the AlN layer is not directly attached to the substrate. This finding suggests that the theoretical models aiming to explain the origin of threading dislocations in these materials should account for the presence of this amorphous layer.

The defects in wurtzite III-nitrides were found to be mainly threading dislocations that are present in both AlN/Si (111) and GaN/AlN/Si (111). Prismatic stacking faults were also found in thinner AlN nucleation layers, but they vanished in thicker layers. Most threading dislocations were of the *a*-type, followed by *a+c*-type dislocations, whereas the *c*-type dislocations were rare. Possible origin of these threading dislocations was investigated using TEM and correlated with the literature. We conclude that the most probable mechanism of their formation is bending of misfit dislocations with *a*-type Burgers vectors towards side facets of growing islands. During the island coalescence, these misfit dislocations react to form threading dislocations with line direction close to $\langle 0001 \rangle$ and the *a*-type Burgers vector. This explains why most threading dislocations are of the edge type. The second probable mechanism is the reaction of partial dislocations bounding a stacking fault, which may give rise to any of the three types of threading dislocations. To be specific, two Shockley partial dislocations with $1/3\langle 10\bar{1}0 \rangle$ Burgers vectors can react and create a perfect *a*-type threading dislocation. Two simple Frank partial dislocations with $1/2\langle 0001 \rangle$ Burgers vectors can combine to produce a perfect *c*-type threading dislocation. Similarly, two complex Frank partials with $1/6\langle 2\bar{2}03 \rangle$ Burgers vectors can react and create a perfect *a+c*-type threading dislocation. Taking into account the experimental evidence and predictions of atomistic simulations, we conclude that the two most probable mechanisms that give rise to threading dislocations in these materials are: (i) bending of misfit dislocations toward the surface of growing islands and their interactions during the island coalescence, and (ii) reactions of partial dislocations bounding the stacking faults.

The EBIC measurements of AlN/Si (111) layers revealed large variations of induced current across the AlN surface. Threading dislocations exhibited only weak drops of induced current. The V-defects acted as strong recombination sites, and this recombination efficiency was further enhanced for the clusters of V-defects. However, V-defects had low density and only local impact on the electrical properties. We assumed that individual threading dislocations had the most significant impact on the properties of the AlN layer due to their much higher density and uniform distribution. We have combined surface topography obtained from AFM with the EBIC signal measured in SEM to link the changes in surface morphology with the reduced electrical activity of the surface of GaN using CPEM. These results show that most threading dislocations in wurtzite GaN and AlN are terminated by surface depressions and lead to carrier losses.

The major types of extended defects in the metastable zincblende structure of III-nitrides were found to be stacking faults. The GaN nucleation layers consist of island-like features elongated in the direction perpendicular to the miscut. For as-grown samples, the surface feature sizes were shown to increase with the thickness of the nucleation layers and also get enhanced by annealing, which is accompanied by the reduction of the surface coverage. Both effects are caused by a concurrent diffusion and desorption (or etching) of the material by the reactor atmosphere. Some fraction of GaN diffuses toward larger islands and causes them to ripen, whereas the remaining material is desorbed or etched away. We have also employed TEM and AFM to characterize the angles of a wide range of well-separated facets. Some of these were attributed to several low-index planes including $\{111\}$, which are expected to play a role in the nucleation of stacking faults and the formation of the wurtzite phase. The angles between the facets and the surface of the SiC substrate were found to be modified by the substrate miscut. In particular, the front facet is consistently shallower and the back facet steeper than facets expected on SiC without miscut.

The spacing of stacking faults in 3C-SiC near the GaN interface is very large and thus they do not significantly influence the defect density in GaN. However, we have shown that these stacking faults readily penetrate into the GaN layer and probably propagate further toward the surface of the GaN film. Unlike in SiC, a large density of stacking faults was found in GaN, which are mostly of the intrinsic type. Stacking faults are mostly bounded by Shockley partial dislocations with $1/6\langle 112 \rangle$ Burgers vectors and, occasionally, by Lomer-Cottrell partial dislocations with $1/6\langle 110 \rangle$ Burgers vectors. 30° Shockley partial dislocations were located at the GaN/SiC interface, where they were able to relieve misfit strain. Out of the possible mechanisms for stacking fault formation we concluded that the most probable mechanism is the dissociation of perfect 60° dislocations and nucleation of partial dislocation half-loops from the surface, which then glide toward the GaN/SiC interface to relieve the misfit strain.

Due to the high dislocation density, interactions of stacking faults were very frequent. Several possibilities of stacking fault interactions were found and were attributed to different outcomes of partial dislocation reactions bounding the stacking fault. We have developed a theoretical model of stacking fault annihilation, which is based on elemental reactions between partial dislocations. The predictions of this model are shown to agree reasonably well with the experimental data.

7 References

- [1] M. Fox, *Optical properties of solids*, 2nd ed., Oxford University Press, Oxford, 2010.
- [2] H. Morkoç, *General Properties of Nitrides*, in: *Handbook of Nitride Semiconductors and Devices*, Wiley-VCH, Chichester, 2009.
- [3] P.B. Hirsch, *Dislocations in semiconductors*, *Mater Sci Tech-Lond.* 1 (1985) 666–677. doi:10.1179/mst.1985.1.9.666.
- [4] G. Naresh-Kumar, J. Bruckbauer, P.R. Edwards, S. Krausel, B. Hourahine, R.W. Martin, M.J. Kappers, M.A. Moram, S. Lovelock, R.A. Oliver, C.J. Humphreys, C. Trager-Cowan, *Coincident Electron Channeling and Cathodoluminescence Studies of Threading Dislocations in GaN*, *Microsc Microanal.* 20 (2014) 55–60. doi:10.1017/S1431927613013755.
- [5] R.A. Oliver, M.J. Kappers, C. McAleese, R. Datta, J. Sumner, C.J. Humphreys, *The origin and reduction of dislocations in Gallium Nitride*, *J Mater Sci-Mater El.* 19 (2008) 208–214. doi:10.1007/s10854-008-9648-7.
- [6] T. Hino, S. Tomiya, T. Miyajima, K. Yanashima, S. Hashimoto, M. Ikeda, *Characterization of threading dislocations in GaN epitaxial layers*, *Appl Phys Lett.* 76 (2000) 3421–3423. doi:10.1063/1.126666.
- [7] N. Yamamoto, H. Itoh, V. Grillo, S.F. Chichibu, S. Keller, J.S. Speck, S.P. DenBaars, U.K. Mishra, S. Nakamura, G. Salviati, *Cathodoluminescence characterization of dislocations in gallium nitride using a transmission electron microscope*, *J Appl Phys.* 94 (2003) 4315–4319. doi:10.1063/1.1598632.
- [8] M. Albrecht, J.L. Weyher, B. Lucznik, I. Grzegory, S. Porowski, *Nonradiative recombination at threading dislocations in n-type GaN: Studied by cathodoluminescence and defect selective etching*, *Appl Phys Lett.* 92 (2008) 231909. doi:10.1063/1.2928226.
- [9] D. Cherns, M.E. Hawkrige, *The structure and properties of dislocations in GaN*, *J Mater Sci.* 41 (2006) 2685–2690. doi:10.1007/s10853-006-7871-2.
- [10] I. Arslan, A. Bleloch, E.A. Stach, N.D. Browning, *Atomic and Electronic Structure of Mixed and Partial Dislocations in GaN*, *Phys Rev Lett.* 94 (2005) 25504. doi:10.1103/PhysRevLett.94.025504.
- [11] Y. Xin, E.M. James, I. Arslan, S. Sivananthan, N.D. Browning, S.J. Pennycook, F. Omnès, B. Beaumont, J.P. Faurie, P. Gibart, *Direct experimental observation of the local electronic structure at threading dislocations in metalorganic vapor phase epitaxy grown wurtzite GaN thin films*, *Appl Phys Lett.* 76 (2000) 466–468. doi:10.1063/1.125789.
- [12] W. Qian, G.S. Rohrer, M. Skowronski, K. Doverspike, L.B. Rowland, D.K. Gaskill, *Open-core screw dislocations in GaN epilayers observed by scanning force microscopy and high-resolution transmission electron microscopy*, *Appl Phys Lett.* 67 (1995) 2284–2286. doi:10.1063/1.115127.
- [13] A. Béré, A. Serra, *Atomic structure of dislocation cores in GaN*, *Phys Rev B.* 65 (2002) 205323. doi:10.1103/PhysRevB.65.205323.

- [14] R. Gröger, L. Leconte, A. Ostapovets, Structure and stability of threading edge and screw dislocations in bulk GaN, *Comput Mater Sci.* 99 (2015) 195–202. doi:10.1016/j.commatsci.2014.12.013.
- [15] I. Belabbas, M.A. Belkhir, Y.H. Lee, J. Chen, A. Béré, P. Ruterana, G. Nouet, Local electronic structure of threading screw dislocation in wurtzite GaN, *Comput Mater Sci.* 37 (2006) 410–416. doi:10.1016/j.commatsci.2005.11.002.
- [16] J. Elsner, R. Jones, P.K. Sitch, V.D. Porezag, M. Elstner, T. Frauenheim, M.I. Heggie, S. Öberg, P.R. Briddon, Theory of Threading Edge and Screw Dislocations in GaN, *Phys Rev Lett.* 79 (1997) 3672–3675.
- [17] M. Matsubara, J. Godet, L. Pizzagalli, E. Bellotti, Properties of threading screw dislocation core in wurtzite GaN studied by Heyd-Scuseria-Ernzerhof hybrid functional, *Appl Phys Lett.* 103 (2013) 262107. doi:10.1063/1.4858618.
- [18] M. Auf der Maur, A. Pecchia, G. Penazzi, W. Rodrigues, A. Di Carlo, Efficiency Drop in Green InGaN / GaN Light Emitting Diodes, *Phys Rev Lett.* 116 (2016) 27401. doi:10.1103/PhysRevLett.116.027401.
- [19] S.P. Denbaars, Gallium-nitride-based materials for blue to ultraviolet optoelectronics devices, *Proc IEEE.* 85 (1997) 1740–1749. doi:10.1109/5.649651.
- [20] D. Zhu, D.J. Wallis, C.J. Humphreys, Prospects of III-nitride optoelectronics grown on Si, *Rep Prog Phys.* 76 (2013) 106501. doi:10.1088/0034-4885/76/10/106501.
- [21] D. Holec, Multi-scale modelling of III-nitrides: from dislocations to the electronic structure, University of Cambridge, 2008.
- [22] L. Pauling, *General chemistry*, Dover Publications, New York, 1988.
- [23] C.-Y. Yeh, Z.W. Lu, S. Froyen, A. Zunger, Zinc-blende-wurtzite polytypism in semiconductors, *Phys Rev B.* 46 (1992) 10086–10097. doi:10.1103/PhysRevB.46.10086.
- [24] M.J. Paisley, Z. Sitar, J.B. Posthill, R.F. Davis, Growth of cubic phase gallium nitride by modified molecular-beam epitaxy, *J Vac Sci Technol A.* 7 (1989) 701–705. doi:10.1116/1.575869.
- [25] O. Brandt, H. Yang, A. Trampert, K. H. Ploog, Growth of Cubic GaN on (001) GaAs, *MRS Proc.* 395 (1995) 27–38. doi:10.1557/PROC-395-27.
- [26] C. Bayram, J.A. Ott, K.-T. Shiu, C.-W. Cheng, Y. Zhu, J. Kim, M. Razeghi, D.K. Sadana, Cubic Phase GaN on Nano-grooved Si (100) via Maskless Selective Area Epitaxy, *Adv Funct Mater.* 24 (2014) 4492–4496. doi:10.1002/adfm.201304062.
- [27] P.M. Anderson, J.P. Hirth, J. Lothe, *Theory of dislocations*, 3rd ed., Cambridge University Press, Cambridge, 2017.
- [28] J.W. Christian, S. Mahajan, Deformation twinning, *Prog Mater Sci.* 39 (1995) 1–157. doi:10.1016/0079-6425(94)00007-7.

- [29] B.K. Meyer, D.M. Hofmann, H. Alves, Defects and defect identification in group III-nitrides, *Mater Sci Eng B*. 71 (2000) 69–76. doi:10.1016/S0921-5107(99)00351-7.
- [30] D. Hull, D.J. Bacon, *Introduction to Dislocations*, 5th ed., Butterworth-Heinemann, Oxford, 2011. doi:10.1016/C2009-0-64358-0.
- [31] R. Hull, J.C. Bean, Misfit dislocations in lattice-mismatched epitaxial films, *Crit Rev Solid State*. 17 (1992) 507–546. doi:10.1080/10408439208244585.
- [32] J. Nord, K. Albe, P. Erhart, K. Nordlund, Modelling of compound semiconductors: analytical bond-order potential for gallium, nitrogen and gallium nitride, *J Phys Condens Matter*. 15 (2003) 5649–5662. doi:10.1088/0953-8984/15/32/324.
- [33] Y. Xin, S.J. Pennycook, N.D. Browning, P.D. Nellist, S. Sivananthan, F. Omnès, B. Beaumont, J.P. Faurie, P. Gibart, Direct observation of the core structures of threading dislocations in GaN, *Appl Phys Lett*. 72 (1998) 2680–2682. doi:10.1063/1.121097.
- [34] J.G. Lozano, H. Yang, M.P. Guerrero-Lebrero, A.J. D’Alfonso, A. Yasuhara, E. Okunishi, S. Zhang, C.J. Humphreys, L.J. Allen, P.L. Galindo, P.B. Hirsch, P.D. Nellist, Direct Observation of Depth-Dependent Atomic Displacements Associated with Dislocations in Gallium Nitride, *Phys Rev Lett*. 113 (2014) 135503. doi:10.1103/PhysRevLett.113.135503.
- [35] H. Yang, J.G. Lozano, T.J. Pennycook, L. Jones, P.B. Hirsch, P.D. Nellist, Imaging screw dislocations at atomic resolution by aberration-corrected electron optical sectioning, *Nat Commun*. 6 (2015) 7266. doi:10.1038/ncomms8266.
- [36] N. Mante, S. Rennesson, E. Frayssinet, L. Largeau, F. Semond, J.L. Rouvière, G. Feuillet, P. Vennéguès, Proposition of a model elucidating the AlN-on-Si (111) microstructure, *J Appl Phys*. 123 (2018) 214502. doi:10.1063/1.5017550.
- [37] A.E. Chernyakov, M.M. Sobolev, V.V. Ratnikov, N.M. Shmidt, E.B. Yakimov, Nonradiative recombination dynamics in InGaN/GaN LED defect system, *Superlattices Microstruct*. 45 (2009) 301–307. doi:10.1016/j.spmi.2008.10.045.
- [38] Z. Antoš, P. Vacek, R. Gröger, Intersections of two stacking faults in zincblende GaN, *Comput Mater Sci*. 180 (2020) 109620. doi:10.1016/j.commatsci.2020.109620.
- [39] P. Ruterana, A. Béré, G. Nouet, Formation and Stability of the Prismatic Stacking Fault in Wurtzite (Al,Ga,In) Nitrides, *MRS Proc*. 595 (1999) F99W3.55. doi:10.1557/PROC-595-F99W3.55.
- [40] A. Teke, H. Morkoç, Group III Nitrides, in: S. Kasap, P. Capper (Eds.), *Springer Handbook of Electronic and Photonic Materials*, Springer US, Boston, MA, 2007: pp. 753–804. doi:10.1007/978-0-387-29185-7_32.
- [41] B. Gil, *Group III nitride semiconductor compounds: physics and applications*, Oxford University Press, Oxford, 1998.
- [42] L. Liu, J.H. Edgar, Substrates for gallium nitride epitaxy, *Mater Sci Eng R*. 37 (2002) 61–127. doi:10.1016/S0927-796X(02)00008-6.

- [43] D.B. Holt, B.G. Yacobi, *Extended defects in semiconductors electronic properties, device effects and structures*, Cambridge University Press, New York, 2007.
- [44] H.J. Leamy, Charge collection scanning electron microscopy, *J Appl Phys.* 53 (1982) R51–R80. doi:10.1063/1.331667.
- [45] H. Brune, Growth Modes, in: K.H.J. Buschow, R.W. Cahn, M.C. Flemings, B. Ilschner, E.J. Kramer, S. Mahajan, P. Veysière (Eds.), *Encyclopedia of Materials: Science and Technology*, Elsevier, Oxford, 2001: pp. 3683–3692. doi:10.1016/B0-08-043152-6/00657-4.
- [46] S. Strite, H. Morkoç, GaN, AlN, and InN: A review, *J Vac Sci Technol B.* 10 (1992) 1237–1266. doi:10.1116/1.585897.
- [47] F.C. Frank, Capillary equilibria of dislocated crystals, *Acta Crystallogr.* 4 (1951) 497–501. doi:10.1107/S0365110X51001690.
- [48] B. Heying, E.J. Tarsa, C.R. Elsass, P. Fini, S.P. DenBaars, J.S. Speck, Dislocation mediated surface morphology of GaN, *J Appl Phys.* 85 (1999) 6470–6476. doi:10.1063/1.370150.
- [49] Z. Chen, L.W. Su, J.Y. Shi, X.L. Wang, C.L. Tang, P. Gao, AFM Application in III-Nitride Materials and Devices, in: V. Bellitto (Ed.), *Atomic Force Microscopy - Imaging, Measuring and Manipulating Surfaces at the Atomic Scale*, InTech, Rijeka, 2012.
- [50] G. Radtke, M. Couillard, G.A. Botton, D. Zhu, C.J. Humphreys, Scanning transmission electron microscopy investigation of the Si(111)/AlN interface grown by metalorganic vapor phase epitaxy, *Appl Phys Lett.* 97 (2010) 251901. doi:10.1063/1.3527928.
- [51] P. Chen, R. Zhang, Z.M. Zhao, D.J. Xi, B. Shen, Z.Z. Chen, Y.G. Zhou, S.Y. Xie, W.F. Lu, Y.D. Zheng, Growth of high quality GaN layers with AlN buffer on Si(1 1 1) substrates, *J Cryst Growth.* 225 (2001) 150–154. doi:10.1016/S0022-0248(01)00842-9.
- [52] A.P. Lange, X.L. Tan, C.S. Fadley, S. Mahajan, Structure and chemistry of aluminum predeposition layers in AlN epitaxy on (111) silicon, *Acta Mater.* 115 (2016) 94–103. doi:10.1016/j.actamat.2016.05.036.
- [53] T. Novák, P. Kostelník, M. Konečný, J. Čechal, M. Kolíbal, T. Šikola, Temperature effect on Al predeposition and AlN nucleation affecting the buffer layer performance for the GaN-on-Si based high-voltage devices, *Jpn J Appl Phys.* 58 (2019) SC1018. doi:10.7567/1347-4065/ab0d00.
- [54] M.-H. Kim, Y.-C. Bang, N.-M. Park, C.-J. Choi, T.-Y. Seong, S.-J. Park, Growth of high-quality GaN on Si(111) substrate by ultrahigh vacuum chemical vapor deposition, *Appl Phys Lett.* 78 (2001) 2858. doi:10.1063/1.1371539.
- [55] S.-J. Lee, S.-H. Jang, S.-S. Lee, C.-R. Lee, Growth and characterization of In_{0.28}Ga_{0.72}N/GaN multiple-quantum wells on Si(111), *J Cryst Growth.* 249 (2003) 65–71. doi:10.1016/S0022-0248(02)02100-0.

- [56] S. Tanaka, Y. Kawaguchi, N. Sawaki, M. Hibino, K. Hiramatsu, Defect structure in selective area growth GaN pyramid on (111)Si substrate, *Appl Phys Lett.* 76 (2000) 2701. doi:10.1063/1.126448.
- [57] G.Q. Hu, X. Kong, L. Wan, Y.Q. Wang, X.F. Duan, Y. Lu, X.L. Liu, Microstructure of GaN films grown on Si(111) substrates by metalorganic chemical vapor deposition, *J Cryst Growth.* 256 (2003) 416–423. doi:10.1016/S0022-0248(03)01368-X.
- [58] R. People, J.C. Bean, Calculation of critical layer thickness versus lattice mismatch for $\text{Ge}_x\text{Si}_{1-x}/\text{Si}$ strained-layer heterostructures, *Appl Phys Lett.* 47 (1985) 322–324. doi:10.1063/1.96206.
- [59] A. Fischer, H. Kühne, H. Richter, New Approach in Equilibrium Theory for Strained Layer Relaxation, *Phys Rev Lett.* 73 (1994) 2712–2715. doi:10.1103/PhysRevLett.73.2712.
- [60] D. Holec, P.M.F.J. Costa, M.J. Kappers, C.J. Humphreys, Critical thickness calculations for InGaN/GaN, *J Cryst Growth.* 303 (2007) 314–317. doi:10.1016/j.jcrysgro.2006.12.054.
- [61] W.D. Nix, B.M. Clemens, Crystallite coalescence: A mechanism for intrinsic tensile stresses in thin films, *J Mater Res.* 14 (1999) 3467–3473. doi:10.1557/JMR.1999.0468.
- [62] B.W. Sheldon, K.H.A. Lau, A. Rajamani, Intrinsic stress, island coalescence, and surface roughness during the growth of polycrystalline film, *J Appl Phys.* 90 (2001) 5097. doi:10.1063/1.1412577.
- [63] D.B. Williams, C.B. Carter, *Transmission electron microscopy: a textbook for materials science*, 2nd ed, Springer, New York, 2008.
- [64] R. Datta, M.J. Kappers, J.S. Barnard, C.J. Humphreys, Revealing all types of threading dislocations in GaN with improved contrast in a single plan view image, *Appl Phys Lett.* 85 (2004) 3411–3413. doi:10.1063/1.1807962.
- [65] P.B. Hirsch, J.G. Lozano, S. Rhode, M.K. Horton, M.A. Moram, S. Zhang, M.J. Kappers, C.J. Humphreys, A. Yasuhara, E. Okunishi, P.D. Nellist, The dissociation of the [a + c] dislocation in GaN, *Philos Mag.* 93 (2013) 3925–3938. doi:10.1080/14786435.2013.797617.
- [66] C.M. Drum, Intersecting faults on basal and prismatic planes in aluminium nitride, *Philos Mag.* 11 (1965) 313–334. doi:10.1080/14786436508221859.
- [67] X.J. Ning, F.R. Chien, P. Pirouz, J.W. Yang, M.A. Khan, Growth defects in GaN films on sapphire: The probable origin of threading dislocations, *J Mater Res.* 11 (1996) 580–592. doi:10.1557/JMR.1996.0071.
- [68] W. Qian, M. Skowronski, M. De Graef, K. Doverspike, L.B. Rowland, D.K. Gaskill, Microstructural characterization of α -GaN films grown on sapphire by organometallic vapor phase epitaxy, *Appl Phys Lett.* 66 (1995) 1252–1254. doi:10.1063/1.113253.

- [69] X.H. Wu, P. Fini, E.J. Tarsa, B. Heying, S. Keller, U.K. Mishra, S.P. DenBaars, J.S. Speck, Dislocation generation in GaN heteroepitaxy, *J Cryst Growth*. 189–190 (1998) 231–243. doi:10.1016/S0022-0248(98)00240-1.
- [70] R.A. Oliver, M.J. Kappers, C.J. Humphreys, Insights into the origin of threading dislocations in GaN/Al₂O₃ from atomic force microscopy, *Appl Phys Lett*. 89 (2006) 011914. doi:10.1063/1.2219747.
- [71] V. Narayanan, K. Lorenz, W. Kim, S. Mahajan, Origins of threading dislocations in GaN epitaxial layers grown on sapphire by metalorganic chemical vapor deposition, *Appl Phys Lett*. 78 (2001) 1544–1546. doi:10.1063/1.1352699.
- [72] M.A. Moram, C.S. Ghedia, D.V.S. Rao, J.S. Barnard, Y. Zhang, M.J. Kappers, C.J. Humphreys, On the origin of threading dislocations in GaN films, *J Appl Phys*. 106 (2009) 073513. doi:10.1063/1.3225920.
- [73] N. Gmeinwieser, U.T. Schwarz, Pattern formation and directional and spatial ordering of edge dislocations in bulk GaN: Microphotoluminescence spectra and continuum elastic calculations, *Phys Rev B*. 75 (2007) 245213. doi:10.1103/PhysRevB.75.245213.
- [74] Y.B. Kwon, J.H. Je, P. Ruterana, G. Nouet, On the origin of a-type threading dislocations in GaN layers, *J Vac Sci Technol A*. 23 (2005) 1588–1591. doi:10.1116/1.2049301.
- [75] V. Narayanan, K. Lorenz, W. Kim, S. Mahajan, Gallium nitride epitaxy on (0001) sapphire, *Philos Mag A*. 82 (2002) 885–912. doi:10.1080/01418610208240008.
- [76] F.Y. Meng, I. Han, H. McFelea, E. Lindow, R. Bertram, C. Werkhoven, C. Arena, S. Mahajan, Direct observation of formation of threading dislocations from stacking faults in GaN layer grown on (0001) sapphire, *Scr Mater*. 64 (2011) 93–96. doi:10.1016/j.scriptamat.2010.09.012.
- [77] A. Stukowski, Visualization and analysis of atomistic simulation data with OVITO—the Open Visualization Tool, *Model Simul Mat Sci Eng*. 18 (2010) 015012. doi:10.1088/0965-0393/18/1/015012.
- [78] P. Vacek, P. Kostelník, R. Gröger, Correlation of Structure and EBIC Contrast from Threading Dislocations in AlN/Si Films, *Phys. Status Solidi B*. 256 (2019) 1900279. doi:10.1002/pssb.201900279.
- [79] X.A. Cao, J.A. Teetsov, F. Shahedipour-Sandvik, S.D. Arthur, Microstructural origin of leakage current in GaN/InGaN light-emitting diodes, *J Cryst Growth*. 264 (2004) 172–177. doi:10.1016/j.jcrysgro.2004.01.031.
- [80] Z. Liliental-Weber, Y. Chen, S. Ruvimov, J. Washburn, Formation mechanism of nanotubes in GaN, *Phys Rev Lett*. 79 (1997) 2835–2838. doi:10.1103/PhysRevLett.79.2835.
- [81] H.K. Cho, J.Y. Lee, G.M. Yang, C.S. Kim, Formation mechanism of V defects in the InGaN/GaN multiple quantum wells grown on GaN layers with low threading dislocation density, *Appl Phys Lett*. 79 (2001) 215–217. doi:10.1063/1.1384906.

- [82] H. Liang, Y. Saripalli, P.K. Kandaswamy, E.P. Carlson, P. Favia, O. Richard, H. Bender, M. Zhao, S.B. Thapa, E. Vancoille, Growth techniques to reduce V-defect density in GaN and AlGaIn layers grown on 200 mm Si (111) substrate, *Phys Status Solidi C*. 11 (2014) 533–536. doi:10.1002/pssc.201300555.
- [83] D. Cherns, S.J. Henley, F.A. Ponce, Edge and screw dislocations as nonradiative centers in InGaIn/GaN quantum well luminescence, *Appl Phys Lett*. 78 (2001) 2691–2693. doi:10.1063/1.1369610.
- [84] X.H. Wu, C.R. Elsass, A. Abare, M. MacK, S. Keller, P.M. Petroff, S.P. Denbaars, J.S. Speck, S.J. Rosner, Structural origin of V-defects and correlation with localized excitonic centers in InGaIn/GaN multiple quantum wells, *Appl Phys Lett*. 72 (1998) 692–694. doi:10.1063/1.120844.
- [85] L.Y. Lee, M. Frentrup, P. Vacek, F.C. Massabuau, M.J. Kappers, D.J. Wallis, R.A. Oliver, Investigation of MOVPE-grown zincblende GaN nucleation layers on 3C- SiC / Si substrates, *J Cryst Growth*. 524 (2019) 125167. doi:10.1016/j.jcrysgr.2019.125167.
- [86] L.Y. Lee, M. Frentrup, M.J. Kappers, R.A. Oliver, C.J. Humphreys, D.J. Wallis, Effect of growth temperature and V/III-ratio on the surface morphology of MOVPE-grown cubic zincblende GaN, *J Appl Phys*. 124 (2018) 105302. doi:10.1063/1.5046801.
- [87] M. Frentrup, L.Y. Lee, S.-L. Sahonta, M.J. Kappers, F. Massabuau, P. Gupta, R.A. Oliver, C.J. Humphreys, D.J. Wallis, X-ray diffraction analysis of cubic zincblende III-nitrides, *J Phys D*. 50 (2017) 433002. doi:10.1088/1361-6463/aa865e.
- [88] K. Lorenz, M. Gonsalves, W. Kim, V. Narayanan, S. Mahajan, Comparative study of GaN and AlN nucleation layers and their role in growth of GaN on sapphire by metalorganic chemical vapor deposition, *Appl Phys Lett*. 77 (2000) 3391–3393. doi:10.1063/1.1328091.
- [89] C.H. Wei, Z.Y. Xie, L.Y. Li, Q.M. Yu, J.H. Edgar, MOCVD Growth of Cubic GaN on 3C-SiC Deposited on Si (100) Substrates, *J Electron Mater*. 29 (2000) 317–321. doi:10.1007/s11664-000-0070-z.
- [90] S.A. Church, S. Hammersley, P.W. Mitchell, M.J. Kappers, S.L. Sahonta, M. Frentrup, D. Nilsson, P.J. Ward, L.J. Shaw, D.J. Wallis, C.J. Humphreys, R.A. Oliver, D.J. Binks, P. Dawson, Photoluminescence studies of cubic GaN epilayers, *Phys Status Solidi B*. 254 (2017) 1600733. doi:10.1002/pssb.201600733.
- [91] R.M. Kemper, P. Veit, C. Mietze, A. Dempewolf, T. Wecker, F. Bertram, J. Christen, J.K.N. Lindner, D.J. As, STEM-CL investigations on the influence of stacking faults on the optical emission of cubic GaN epilayers and cubic GaN/AlN multi-quantum wells, *Phys Status Solidi C*. 12 (2015) 469–472. doi:10.1002/pssc.201400154.
- [92] A.F. Wright, Basal-plane stacking faults and polymorphism in AlN, GaN, and InN, *J Appl Phys*. 82 (1997) 5259–5261. doi:10.1063/1.366393.
- [93] F. Glas, A simple calculation of energy changes upon stacking fault formation or local crystalline phase transition in semiconductors, *J Appl Phys*. 104 (2008) 093520. doi:10.1063/1.3009338.

- [94] R. Kozak, I. Prieto, Y.A.R. Dasilva, R. Erni, O. Skibitzki, G. Capellini, T. Schroeder, H.V. Känel, M.D. Rossell, Strain relaxation in epitaxial GaAs / Si (0 0 1) nanostructures, *Philos Mag.* 97 (2017) 2845–2857. doi:10.1080/14786435.2017.1355117.
- [95] B.C.D. Cooman, C.B. Carter, The accommodation of misfit at {100} heterojunctions in III–V compound semiconductors by gliding dissociated dislocations, *Acta Metall.* 37 (1989) 2765–2777. doi:10.1016/0001-6160(89)90311-8.
- [96] P.M.J. Marée, J.C. Barbour, J.F. Van der Veen, K.L. Kavanagh, C.W.T. Bulle-Lieuwma, M.P.A. Vieggers, Generation of misfit dislocations in semiconductors, *J Appl Phys.* 62 (1987) 4413–4420. doi:10.1063/1.339078.

Author publications and other outputs

Publications in impacted journals

(1) L.Y. Lee, M. Frentrup, P. Vacek, M.J. Kappers, D.J. Wallis, R.A. Oliver: Investigation of stacking faults in MOVPE-grown zincblende GaN by XRD and TEM. *J Appl Phys.* 125 (2019) 105303.

My contribution: Construction of theoretical model for stacking fault annihilation

(2) P. Vacek, P. Kostelník, R. Gröger: Correlation of Structure and EBIC Contrast from Threading Dislocations in AlN/Si Films. *Phys Status Solidi B.* 256 (2019) 1900279.

(3) L.Y. Lee, M. Frentrup, P. Vacek, F.C.-P. Massabuau, M.J. Kappers, D.J. Wallis, R.A. Oliver: Investigation of MOVPE-grown zincblende GaN nucleation layers on 3CSiC/ Si substrates. *J Cryst Growth.* 524 (2019) 125167.

My contribution: AFM measurement and analysis of 2° miscut sample series and antiphase domains

(4) Z. Antoš, P. Vacek, R. Gröger: Intersections of two stacking faults in zincblende GaN. *Comp Mater Sci.* 180 (2020) 109620.

My contribution: TEM measurement and analysis

(5) P. Šťastný, P. Vacek, M. Trunec: Characterization of microstructure and phase distribution of sintered multiphasic calcium phosphate bioceramics. *Ceram Int.* 46 (2020) 5500-5504.

My contribution: TEM measurement and analysis

(6) P. Vacek, M. Frentrup, L.Y. Lee, F.C.-P. Massabuau, M.J. Kappers, D.J. Wallis, R. Gröger, R.A. Oliver: Defect structures in (001) zincblende GaN/3C-SiC nucleation layers. *J Appl Phys.* *In press* (2021).

Presentations at international conferences

P. Vacek, L.Y. Lee, M. Frentrup, M.J. Kappers, R.A. Oliver, D.J. Wallis: Investigation of zinc blende GaN nucleation layers deposited on 3C-SiC / Si templates. *UK Semiconductors*, (2018) Sheffield, United Kingdom.

Posters at international conferences

(1) P. Vacek, J. Dluhoš, M. Rudolf, R. Gröger: Correlative probe and electron microscopy of threading dislocations in III-nitrides. *CEITEC PhD Retreat* (2017) Telč, Czech Republic.

(2) P. Vacek, Z. Nováček, J. Dluhoš, R. Gröger: Correlative probe and electron microscopy of GaN and AlN films on Si (111) substrate. *International Congress: Engineering of Advanced Materials* (2017) Erlangen, Germany.

(3) P. Vacek, P. Kostelník, R. Gröger: Correlation of Structure and EBIC Contrast from Threading Dislocations in AlN/Si Films. *CEITEC PhD Retreat* (2019) Kouty, Czech Republic.

(4) P. Vacek, P. Kostelník, R. Gröger: Correlation of Structure and EBIC Contrast from Threading Dislocations in AlN/Si Films. *International Conference on Defects in Semiconductors* (2019) Seattle, WA, USA.

Projects

BUT Junior internal research project 2017 “Correlative probe and electron microscopy imaging of threading dislocations in III-nitrides”, No. STI-J-17-4388 (principal investigator).

Internships

Doctoral internship (February-July 2017): Department of Materials Science and Metallurgy, University of Cambridge, UK.

Supervisor: Prof. Rachel Oliver

Topic: Studies of nucleation layers for the growth of cubic zincblende GaN on 3C-SiC/Si {001} substrates.

List of symbols and abbreviations

AFM	Atomic force microscopy
CPEM	Correlative probe and electron microscopy
DFT	Density functional theory
EBAC	Electron beam absorbed current
EBIC	Electron beam induced current
EDX	Energy-dispersive X-ray spectroscopy
FCC	Face-centered cubic
FIB	Focused ion beam
HAADF	High-angle annular dark field
HCP	Hexagonal close-packed
LED	Light-emitting diode
MOCVD	Metal-organic chemical vapor deposition
NL	Nucleation layer
SEM	Scanning electron microscopy
SF	Stacking fault
SPM	Scanning probe microscopy
STEM	Scanning transmission electron microscopy
TD	Threading dislocation
TEM	Transmission electron microscopy
XRD	X-ray diffraction
zb-GaN	Zincblende GaN